学位論文

Abundance Determinations of Classical Cepheids in the Galactic Center with Near-infrared High-resolution Spectroscopy

(近赤外線高分散分光による銀河系中心セファイドの金属量決定)

平成27年 11月 博士(理学)申請

東京大学大学院理学系研究科

天文学専攻

福江 慧

Abstract

The metallicity gradient of the Galactic disk provides important information on the chemical evolution of the disk. Previous studies show that the iron abundances of stars increase on average towards the inner part of the Galactic disk. The iron abundances in the Galactic Center region provide critical information to interpret the metallicity gradient. Cepheid variable stars are one of the best tracers of the metallicity distribution. However, only a few Cepheids in the inner Galaxy ($R_{\rm GC}$, Galactocentric distance, less than 5 kpc) have been identified and used for tracing the metallicity gradient. Matsunaga et al. (2011, 2015) recently discovered four Classical Cepheids in the Galactic Center region ($R_{\rm GC} < 200$ pc). The severe foreground reddening, requires observations in the infrared rather than in the optical, but almost no one has done high-resolution spectroscopy of Cepheids in the infrared. Therefore the goals of this thesis are twofold: (1) to establish the method of abundance analysis using near-infrared high-resolution spectra and (2) to measure the iron abundances of the Cepheids newly found in the Galactic Center. For these purposes, we obtained H-band spectra of the new Cepheids using *Subaru*/IRCS (R=20,000, λ = 14600–17900 Å). We also observed calibration stars, including G- and K-type giants/supergiants and standard Cepheids (δ Cep, X Cyg), whose iron abundances have been well determined.

Firstly, we developed and verified the method of abundance analysis by investigating H-band spectra of 10 G- and K-type standard stars. We used MPFIT (Takeda, 1995) based on ATLAS9 (Kurucz, 1993a) to calculate atmospheric models and to synthesize model spectra. We found that synthesized model spectra reasonably fit with observational data using the atomic linelist of Meléndez & Barbuy (1999). The iron abundances derived together with microturbulence ξ agree with those in the literature.

Secondly, we constructed the method of determining effective temperature using line-depth ratios (LDRs). This method has been used for optical spectra, but we found relations useful for H-band spectra for the first time. The ratios of absorption lines with different excitation potentials can be used as temperature scales. The most important advantage of the LDR method is their robustness against interstellar reddening and extinction. Furthermore, the scales are constructed and calibrated empirically by observables. We found nine pairs of absorption lines whose LDRs allow us to determine the temperatures of G- and K-type giants/supergiants to an accuracy of $\sim$40 K. Checking the dependency of our scales on stellar parameters, we found that the temperature scales we developed may slightly bias the estimates for stars with significantly different iron abundances, i.e. [Fe/H]< -0.3 dex or [Fe/H]$> +0.3$ dex. Additionally examined is a method of using LDRs for simultaneously deriving all the major atmospheric parameters ($T_{\rm eff}$, $\log g$, [Fe/H], ξ, [X/Fe]). Our experiment demonstrated that it can work well for model spectra without errors, although it turned out to be severely affected

by observational errors of the spectra.

Thirdly, we applied MPFIT and the LDR method to two calibration Cepheids, δ Cep and X Cyg. Derived effective temperatures and iron abundances are found to be consistent with previous estimates obtained by other groups using optical spectra.

Finally, the same methods were applied to the target Cepheids in the Galactic Center. Although their spectra have significantly lower S/N, 30–70, than those for calibration stars, we obtained the temperatures, microturbulence, and iron abundances with the following accuracies: $\Delta T_{\rm eff}$ =120–300 K, $\Delta\xi$ =0.5–1.0 km/s, and Δ[Fe/H] $\sim$ 0.06 dex (statistical) or 0.1–0.3 dex (with various uncertainties included). Their iron abundances are found to be slightly higher than solar, [Fe/H]=0.1–0.2 dex, except one object with +0.5 dex (for which the S/N of the spectrum is lowest, though). Because of the metallicity dependence of the LDR temperature scales, we developed an iterative method to estimate the temperature and iron abundance and applied it to this metal-rich object. This iterative analysis leads to a slightly higher iron abundance, +0.6 dex, with a higher temperature, 4940 K, than original estimate by 160 K. As the results, we derived iron abundances to be +0.1–0.2 dex for three Cepheids and +0.6 dex for the last. The statistical and systematic errors are 0.06 dex and 0.1–0.2 dex, respectively.

Previous observations report that other types of stars around the Galactic Center have iron abundances similar to the solar or slightly higher, 0.0–0.2 dex. Some of the objects are considered to be rather old, at least a few Gyr. We infer that the iron abundances of stars in this region, $R_{\rm GC} < 200$ pc, have remained more-or-less constant over a large fraction of the history of the Milky Way evolution. This iron abundance is close to the average of iron abundances of old evolved stars in the Galactic bulge ($R_{\rm GC} < 3$ kpc), which suggests that gas assembly made of mass-loss gas from the bulge stars was used for the star formation in the Center ($R_{\rm GC} < 200$ pc). On the other hand, Cepheids in the inner part of the disk ($3.5 < R_{\rm GC} < 5$ kpc) are known to have higher iron abundances, which are more similar to the highest iron abundance, +0.6 dex, among our targets. Such a high iron abundance in the Galactic Center may be explained by an inflow of metal-rich gas from the inner disk.

Contents

1 Introduction **7**

1.1 The metallicity gradient of the Galactic disk 7

1.2 Goals and structure of the thesis 10

2 Observations and Reductions **11**

2.1 Observation 11

2.1.1 Targets 11

2.1.2 Instruments 11

2.1.3 Observations with *Subaru*/IRCS 13

2.2 Data Reduction 13

2.2.1 Data Reduction using IRAF 13

2.2.2 Estimation of signal-to-noise ratio 19

3 Abundance analysis of Metal standard stars **21**

3.1 SPTOOL 21

3.2 Linelist in the infrared wavelength 23

3.3 The determination of microturbulence 28

3.4 Abundance analysis of metal standard stars 31

3.4.1 Iron abundance determination with H-band spectra 31

3.4.2 Comparison with the iron abundances in literature 31

3.5 Effects of the assumed solar abundance ratio 36

3.6 Summary 38

4 Line-depth ratios in H band to determine $T_{\rm eff}$ **39**

4.1 Introduction to the LDR method 39

4.2 Temperature scales in the H band 41

4.3 Discussion 50

4.3.1 Sensitivity to atmospheric parameters 50

4.3.2 Line blending 56

4.4 Summary 56

5 Determination of stellar parameters using LDR **61**

5.1 Method 61

5.2 Effects of observational errors 64

6 Abundance analysis of Standard Cepheids **67**
6.1 Atmospheric parameters 67
6.2 Abundance analysis of standard Cepheids 72

7 Abundance analysis of GC Cepheids **75**
7.1 The effects of low signal-to-noise ratios 75
7.2 Atmospheric parameters 79
7.3 Abundance analysis of the targets 79
7.4 Iteration to re-determine temperature and iron abundance considering the LDR dependency on metallicity 85

8 Discussion and Summary **87**
8.1 Discussion 87
8.2 Summary 92

A Solar abundance ratios **101**

B Histograms of [Fe/H] and literature values **105**

C Line depths and the ratios of all observed stars **121**

Chapter 1

Introduction

In this thesis we report measurement of iron abundance, [Fe/H], of Cepheids found in the Galactic Center to investigate the metallicity gradient of the Galactic disk, i.e. metallicity distribution as a function of Galactocentric distance ($R_{\rm GC}$). We introduce previous studies on the metallicity gradient and why Cepheids are important in section 1.1 and describe our scientific goals and the structure of the thesis in section 1.2.

Throughout this thesis, we use the notation $\log\epsilon(\mathrm{X})$ for the abundance of an element X, $\log\epsilon(\mathrm{X}) = \log \mathrm{N_X}/\log \mathrm{N_H} + 12$, where $\mathrm{N_X}$ indicates the number density of the element X. The abundance of hydrogen is taken as $\log\epsilon(\mathrm{H}) = 12$ as is conventionally done. We also use the notation [Fe/H] and [X/Fe] which are logarithmic abundances with respect to the solar values:

$$\begin{aligned}[\mathrm{Fe/H}] &= (\log\epsilon(\mathrm{Fe})/\log\epsilon(\mathrm{H})) - (\log\epsilon(\mathrm{Fe})/\log\epsilon(\mathrm{H}))_\odot \\ [\mathrm{X/Fe}] &= (\log\epsilon(\mathrm{X})/\log\epsilon(\mathrm{Fe})) - (\log\epsilon(\mathrm{X})/\log\epsilon(\mathrm{Fe}))_\odot.\end{aligned}$$

We adopt the solar iron abundance of $\log\epsilon(\mathrm{Fe}) = 7.50$ (see more details on the solar abundance in Section 3.5 and Appendix A).

1.1 The metallicity gradient of the Galactic disk

The Milky Way is important not only because it hosts our Solar system but also because we can investigate stellar populations and interstellar components in greater detail than any other galaxies. Recent large surveys for stellar populations in various regions of the Milky Way have been revolutionizing the study of its structure and evolution (e.g. Ivezić et al., 2012). In addition to many exciting results on the halo, large-scale (10^4 to 10^6 stars) spectroscopic surveys also make it possible to test chemo-dynamical models of the disk with various physical processes, such as radial migration (e.g., Schönrich & Binney, 2009; Haywood et al., 2013). A critical observable feature for investigating the large-scale disk structure is the metallicity gradient (Chiappini et al., 2001).

In order to study the metallicity gradient, we need tracers whose distances and locations can be accurately determined. For measuring distances of stars, trigonometric parallax is the most fundamental method. Hipparcos satellite made a giant step forward in the parallax measurements (Perryman et al., 1997), but its accuracy only allowed us to measure distances to stars within ∼100 pc. Gaia satellite was launched in 2013 for mapping stars in a very large extent of the Milky Way (Gilmore et

al., 2012). However, its optical observation is strongly affected by dust extinction along the Galactic plane (Reylé et al., 2008). JASMINE satellite being planned by National Astronomical Observatory of Japan is expected to make infrared parallax measurements of stars in obscured regions of the inner Milky Way in the future (Gouda & Working Group, 2010). At present, at least, it is necessary to use tracers whose distances can be measured with a method other than parallax.

Cepheid variable stars are, in fact, accurate distance indicators from period-luminosity relation (Sandage et al., 2006). They are young stars evolved from intermediate-mass stars (10–300 Myr, 4–11 $M_{\odot}$, Bono et al., 2005). They are concentrated to the disk, in particular to the thin disk (predominantly within 100 pc around the plane). With richness of absorption lines in their spectra, the chemical abundances can be accurately measured. In fact the abundance gradient traced by them is found to be the clearest and tightest in previous studies. In the innermost disk ($R_{\rm GC} \sim$ 3.5–5 kpc), the iron abundances are supersolar, [Fe/H] $\sim$ 0.4 dex. On the other hand, the iron abundances in the outer disk region ($R_{\rm GC} \sim 15$ kpc) are subsolar or more metal-poor, $-0.2 \sim -0.5$ (e.g., Andrievsky et al., 2004; Luck et al., 2006; Lemasle et al., 2008). Pedicelli et al. (2009) found gradient of -0.051 ± 0.004 dex/kpc using iron abundances of 265 Cepheids located at Galactocentric distances ranging from 5 to 17 kpc based either on high-resolution spectra or on photometric metallicity indices. Genovali et al. (2014) expanded samples toward outer region up to $R_{\rm GC} = 19$ kpc, and obtained the gradient of -0.060 ± 0.002 dex/kpc. These results show a good agreement with the current chemical evolution model (Minchev et al., 2013).

A drawback of using Cepheids to trace the metallicity gradient is incompleteness of the current samples in the Milky Way. Previous surveys of variable stars, mainly conducted in the optical wavelengths, are strongly limited by interstellar extinction. Within $R_{\rm GC} = 3$ kpc, there have been no Cepheids whose iron abundances were measured before (see, e.g., Figure 4 of Genovali et al., 2014). On the other hand, recent infrared observations are beginning to reveal Cepheids spread across a wide area of the Milky Way (Matsunaga et al., 2011; Feast et al., 2014; Matsunaga, 2014). The main targets in this thesis are four Cepheids recently discovered by Matsunaga et al. (2011, 2013, 2015). As reported by these authors, the distances and kinematics of these Cepheids suggest that they belong to Nuclear Stellar Disk (NSD), which is a disk-like system of stars within $\sim$ 200 pc around the Galactic Center (Launhardt et al., 2002). These objects are the first Cepheids in the very center of the Milky Way, thus providing a new insight into the metallicity gradient. However, foreground extinctions of these objects are around 2–3 mag in K which correspond to roughly 20–30 mag in V, and optical observations are therefore impossible. We use spectra in the H band (1.4–1.8 μm) which we obtained using *Subaru*/IRCS as we describe in Chapter 2.

Another group of useful tracers of the metallicity gradient is stellar clusters. Their distances and other parameters such as age and foreground extinction can be estimated based on, for example, isochrone fitting. Their metallicity distribution also indicates the radial gradient (Friel & Janes, 1993; Twarog et al., 1997). Unlike Cepheids, the ages of clusters range from a few Myr to almost the age of the Milky Way. This makes it possible to study time evolution of the metallicity gradient (e.g., Tsujimoto et al., 2010; Jacobson et al., 2011), though the accuracy of the cluster ages is not as good as that of Cepheids. Recent infrared surveys have revealed a rich group of massive stellar clusters where several red supergiants are associated (Davies et al., 2012, and references therein). They seem to be preferentially found around the near- and far-side ends of the Galactic bar although the global distribution of such massive clusters in the inner part of the Milky Way remains to be concluded with

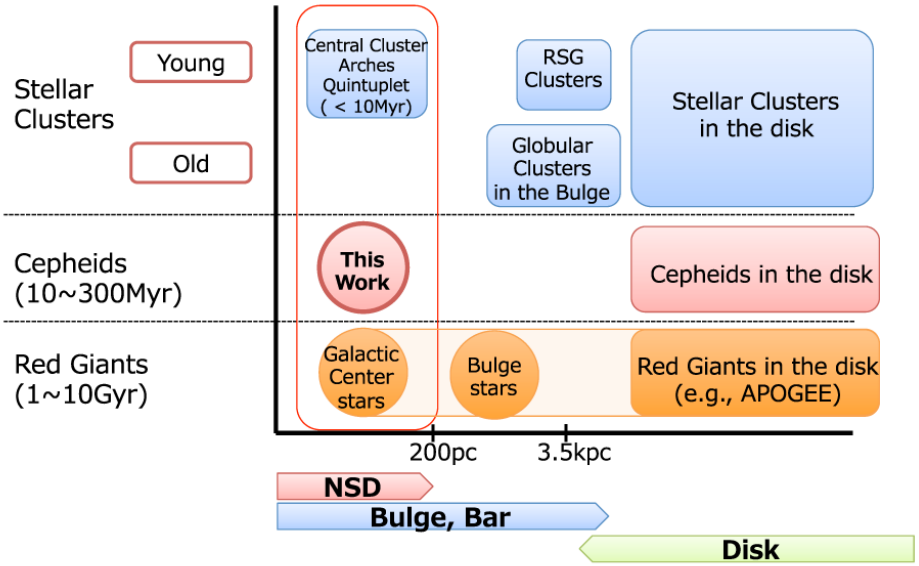

Figure 1.1 Schematic diagram of stellar populations useful for tracing metallicity distribution. The targets are widely distributed in the Galactic plane, from the Galactic Center, in particular the Nuclear Stellar Disk (NSD), to the outer disk.

more complete surveys and detailed studies. Surprisingly low iron abundances, [Fe/H]~ -0.25 dex, have been reported for some of these massive clusters (Davies et al., 2009b; Origlia et al., 2013, 2015), and no firm scenario to explain such low iron abundances has been proposed yet.

We here briefly summarize focus on various types of objects in the NSD to compare with our target Cepheids and to discuss the evolution of the NSD (Figure 1.1). In the NSD at $R_{\rm GC} < 60$ pc, three prominent clusters are known: the Central Cluster (a few pc around Sgr A*), the Arches and Quintuplet Clusters (24 and 30 pc, respectively, form Sgr A* in projected distance). These clusters are young (a few Myr) and their iron abundances are around solar (Cunha et al., 2007). In the same region, the iron abundances of several red giants (1–10 Gyr) are also found to be around solar (Ryde & Schultheis, 2015). These results make it possible to discuss time variation of iron abundance in the NSD by comparing metallicities of old and young stars.

1.2 Goals and structure of the thesis

The primary goal of this work is to measure the iron abundances, [Fe/H], of Cepheids found in the NSD. This will be the first of such measurements for Cepheids located within ∼3.5 kpc of the Galactic Center and provide important constraints on the Galactic chemical evolution. For this purpose, we have to develop the method of deriving the iron abundances with H-band spectra as follows:

- Abundance measurement of metallicity with Fe I lines in the H-band (Chapter 3)
  We examine the abundance analysis method using H-band spectra of metal standard stars. Important steps include selection of the list of atomic lines and determination of the microturbulence.

- Determination of temperature with the line-depth ratio (LDR) method (Chapter 4)
  We construct temperature indicators for the LDR method, for the first time, using H-band spectra of calibration stars. The most important advantage of this method is its robustness against interstellar reddening and extinction.

- Abundance analysis of Cepheids (Chapter 6 and 7)
  We apply the above procedures to spectra of Cepheids, first to those of standard Cepheids and then to those of the targets. In order to take into account the sensitivity of the LDRs to metallicity, we develop an iterative method to determine $T_{\rm eff}$ and [Fe/H] of objects outside the solar abundance regime.

In Chapter 5, in addition, we consider a different method of deriving stellar parameters including temperature and metallicity by using LDRs. This may be a simple and easy-to-use method, but the accuracy of the estimate is affected by observational errors more than the method we use in Chapter 6. Then, in Chapter 8, we compare the iron abundances of the target Cepheids with those of other relevant stars in the inner Galaxy and discuss the impact of our results on the chemical evolution of the Milky Way. And we also summarize the thesis and gives future prospects.

Through this thesis, we establish a method of deriving a iron abundance and other parameters with H-band high-resolution spectra and apply this to the Cepheids in an uncultivated region in terms of the metallicity gradient. Recent near-infrared surveys, such as VVV survey (e.g., Dékány et al., 2015), have been discovering obscured Cepheids in the inner part of the Milky Way. The analysis method developed here shall be useful for investigating such new Cepheids in the future.

Chapter 2

Observations and Reductions

In order to achieve the goals of this thesis, we observed the target Cepheids and calibration stars. In this Chapter, we describe the observations and data reduction to obtain spectra of the objects which are ready for the chemical abundance analysis. We followed standard process for analyzing echelle spectra. In addition, we estimated realistic signal-to-noise ratios using method described in Fukue et al. (2015).

2.1 Observation

2.1.1 Targets

Our targets are summarized in Table 2.1. The main targets of this work are Cepheids in the Nuclear Stellar Disk, while we also observed several calibrating stars, both Cepheids and static stars (i.e. stars without strong pulsation). The static calibrating stars are composed of 10 objects, K- and G-type giants and supergiants, whose parameters are relatively well known in optical. Table 2.1 lists the parameters, $T_{\rm eff}$, $\log g$ and [Fe/H], adopted from Prugniel et al. (2011, hereafter P11) and other basic information where available. P11 determined these parameters by least-squares fitting to synthesized spectra. The exceptions were Arcturus and HD 18391, for which P11 averaged the literature values without attempting error estimates. For these two stars, we adopted the typical error presented in their study. We also observed two Cepheids, δ Cep and X Cyg, whose parameters are well known.

2.1.2 Instruments

The infrared camera and spectrograph (IRCS) is attached to a Nasmyth focus of the *Subaru* 8.2 m telescope (Kobayashi et al., 2000). IRCS consists of two sections, a cross-dispersed echelle spectrograph that provides middle- to high-spectral resolutions ($\lambda/\Delta\lambda$ =5,000–20,000) and a near-infrared camera with two pixel-scale mode of 58 and 23 mas. The camera can be used as an infrared slit viewer for the echelle spectrograph. This slit viewer enables us to keep targets within the slit of the echelle spectrograph even if they are only visible in the infrared. Each section is equipped with a Raytheon 1024×1024 InSb IR array with an Aladdin multiplexer. IRCS is designed to be used efficiently with the *Subaru* Adaptive Optics (AO) system to achieve high angular resolution.

[1] These data are taken from IRCS web page, http://www.naoj.org/Observing/Instruments/IRCS/echelle/orders.html.

Table 2.1. List of the target Cepheids and calibrating stars and their parameters.

Object	Spectral Type	Right Ascension J2000.0	Declination J2000.0	$T_{\rm eff}$ (K)	$\log g$(cgs) (dex)	[Fe/H] (dex)	Period (days)
Target stars							
GCC-a	···	17 46 06.01	−28 46 55.1	···	···	···	23.528
GCC-b	···	17 45 32.27	−29 02 55.2	···	···	···	19.942
GCC-c	···	17 45 30.89	−29 03 10.5	···	···	···	22.755
GCC-d	···	17 44 56.90	−29 13 33.7	···	···	···	18.886
Calibration Cepheids							
δ Cep	F5Ib–G1Ib	22 29 10.27	+58 24 54.71	5625–6663	1.9–2.6	+0.04±0.05	5.366
X Cyg	F7Ib–G8Ib	20 43 24.19	+35 35 16.08	4851–6145	0.8–1.9	+0.10±0.03	16.386
Calibration stars							
HD 219978	K4.5Ib	23 19 23.77	+62 44 23.18	3951±55	0.57±0.18	+0.22±0.08	···
HD 137704	K4III	15 26 17.38	+34 20 09.58	4084±42	1.97±0.21	−0.32±0.08	···
Arcturus	K2III	14 15 39.67	+19 10 56.67	4280±60	1.70±0.13	−0.53±0.05	···
HD 12014	K0Ib	01 59 50.89	+59 09 38.99	4371±108	0.66±0.16	+0.04±0.10	···
HD 124186	K4III	14 11 15.12	+32 17 45.21	4419±59	2.66±0.17	+0.30±0.06	···
μ Leo	K2III	09 52 45.81	+26 00 25.03	4466±54	2.65±0.15	+0.31±0.06	···
HD 223047	G5Ib	23 46 02.04	+46 25 12.97	5002±50	1.26±0.09	+0.04±0.05	···
HD 196755	G5IV+	20 39 07.78	+10 05 10.33	5582±31	3.64±0.07	−0.02±0.03	···
HD 204155	G5	21 26 42.90	+05 26 29.90	5718±56	3.93±0.11	−0.69±0.06	···
HD 18391	G0Ia	02 59 48.72	+57 39 47.65	5750±60	1.20±0.17	−0.13±0.05	···

Note. The spectral types and atmospheric parameters of the two standard Cepheids are taken from Takeda et al. (2013) and Kovtyukh et al. (2005). The spectral types of other calibrating stars are taken from the SIMBAD database (operated at CDS, Strasbourg, France), and their parameters and errors are adopted from Prugniel et al. (2011).

Table 2.2. Wavelength coverages[1] of H-band orders of $Subaru$/IRCS.

Order	Wavelength (μm)	Dispersion (A/pixel)
32	1.7485–1.7910	0.416
33	1.6955–1.7368	0.404
34	1.6455–1.6858	0.394
35	1.5985–1.6377	0.384
36	1.5540–1.5923	0.374
37	1.5120–1.5493	0.365
38	1.4721–1.5086	0.357

2.1.3 Observations with $Subaru$/IRCS

In 2010 and 2012, we obtained H-band spectra of our targets using IRCS. We used the high-resolution mode with the narrowest slit (0.14 arcsec, $\lambda/\Delta\lambda = 20,000$), but the spectra still cover a wide range of λ (14600–17900 Å in the 38th to 32nd orders, Table 2.2). During the July 2012 run, we used the adaptive optics system AO188 with laser star guiding (Hayano et al., 2010). In June 2010 and May 2012, the AO-guided observations were interrupted by instrumental problems and poor seeing conditions. For the calibrating and target Cepheids, we only use the data in the 2012 July run in the following analysis. Each target was integrated at different positions along the long slit, positions A and B, in the order A-B-B-A. In contrast, Arcturus is very bright and illuminates almost the entire slit even at the shortest integration time (0.4 sec). Sky frames (S) with no objects in the slit were obtained after and before integrations at the object position (O) in the order O-S-S-O. For wavelength calibration and for removing the telluric absorption lines, we also observed telluric standard stars. The observational log including the list of telluric standards is given in Table 2.3.

2.2 Data Reduction

2.2.1 Data Reduction using IRAF

Basic data reduction of the spectra was performed using the Image Reduction and Analysis Facility (IRAF[2]). Bad pixels in each raw image were masked by data provided on the IRCS web page[3]. Background was removed from the object images by subtracting an image at a shifted position from the counterpart of the AB pair. The images were then flat fielded using normalized flat images from dome screen shots (20 with flat lamp illumination; 20 without illumination). Figures 2.1 and 2.2 show examples of the echellogram images for the dome flat and a target (μ Leo). We then extracted one-dimensional spectra in the 32nd to 38th orders from each image. Because the background level

[2]IRAF is distributed by the National Optical Astronomy Observatory, which is operated by the Association of Universities for Research in Astronomy (AURA) under cooperative agreement with the National Science Foundation.

[3]http://www.naoj.org/Observing/Instruments/IRCS/

Table 2.3. Observational log for our targets and calibration stars.

Object	H (mag)	IT (s)	NDR	Air-mass	S/N	Tell	Date	Phase ϕ
Target stars								
GCC-a	11.9	300×11	16	1.59-1.52	42	E	2012.07.26	0.22
GCC-b	11.9	300×11	16	1.55-1.74	55	E	2012.07.26	0.23
GCC-c	12.4	300×12	16	1.52-1.57	35	F	2012.07.27	0.69
GCC-d	12.1	300×8	16	1.83-2.13	36	G	2012.07.27	0.18
Calibration stars								
δ Cep	2.47	1.0×4	2	1.44	221	D1	2012.07.26	0.37
X Cyg	3.94	2.0×4	4	1.61	181	D1	2012.07.26	0.07
HD 219978	1.19	0.4×4	1	1.43	211	D1	2012.07.26	
HD 137704	2.43	0.5×4	1	1.27	164	C	2012.05.25	
Arcturus	–2.81	0.4×4	1	1.07	209	B	2010.06.20	
HD 12014	3.92	1.0×4	2	1.31	179	D2	2012.07.27	
HD 124186	3.66	1.0×4	2	1.10	151	C	2012.05.25	
μ Leo	1.33	2.0×4	4	1.77	273	A	2010.06.20	
HD 223047	2.70	0.5×4	1	1.11	173	D2	2012.07.27	
HD 196755	3.64	1.0×4	2	1.37	194	D1	2012.07.26	
HD 204155	7.03	50×4	16	1.34	164	D1	2012.07.26	
HD 18391	2.72	0.5×4	1	1.35	162	D1	2012.07.27	
Telluric standard stars								
HD 91130	5.55	120×4	16	1.68	393	A	2010.06.20	
HD 177756	3.64	10×4	12	1.13	310	B	2010.06.20	
HD 138341	5.87	15×4	16	1.10	229	C	2012.05.25	
HIP 100664	6.10	10×4	16	1.37	281	D1	2012.07.26	
···	···	15×4	16	1.33	224	D2	2012.07.27	
HD 163955	4.60	3.0×4	7	1.57	247	E	2012.07.26	
HD 175360	5.85	20×4	16	1.53	209	F	2012.07.27	
HIP 93526	5.32	8.0×4	16	1.79	237	G	2012.07.27	

Note. H-band magnitudes and phases at the epoch of the spectral observations are estimated for the target Cepheids based on the light curves of Matsunaga et al. (2015), while the magnitudes of the other object are taken from SIMBAD. For calculating the observed phases of two standard Cepheids, we adopted the epoch and period from Andrievsky et al. (2005) and Kovtyukh et al. (2005). IT and NDR indicate integration time and number of non-destructive readouts, respectively. See section 2.2.2 and Table 2.4 about signal-to-noise ratio, (S/N). Log for telluric standard stars is also given and the column "Tell" indicates which telluric standard was used for each object.

Table 2.4. Signal-to-noise ratios for individual orders and their averages.

Object	Tell	m=38	m=37	m=36	m=35	m=34	m=33	m=32	Average
GCC-a	1	15	29	34	48	51	53	41	43
	2	15	29	34	47	50	52	38	42
GCC-b	1	21	41	46	63	67	66	52	57
	2	21	40	45	62	64	63	47	55
GCC-c	1	4	22	27	40	45	47	37	36
	2	4	22	26	40	44	45	34	35
GCC-d	1	14	26	30	42	42	43	33	37
	2	13	25	30	42	42	43	31	36
δ Cep	1	228	384	342	435	416	354	191	360
	2	106	203	163	323	208	208	81	202
X cyg	1	119	209	160	401	193	224	73	218
	2	85	158	121	309	151	169	56	165
HD 219978	1	160	295	235	432	331	335	126	298
	2	96	186	146	322	195	204	73	191
HD 137704	1	140	235	201	272	228	240	108	219
	2	95	165	143	196	158	156	76	152
Arcturus	1	159	303	222	328	317	303	124	272
	2	112	224	164	271	197	188	60	193
HD 12014	1	155	305	276	381	264	267	133	275
	2	91	179	152	242	168	154	78	164
HD 124186	1	109	190	161	237	204	213	85	186
	2	83	147	126	182	150	148	67	139
μ Leo	1	194	360	319	390	423	471	209	360
	2	142	278	245	284	291	270	142	252
HD 223047	1	140	264	233	369	249	238	92	249
	2	87	169	143	239	164	147	67	158
HD 196755	1	118	266	184	407	239	247	79	243
	2	84	178	131	311	169	178	59	175
HD 204155	1	92	176	126	361	171	175	49	183
	2	73	142	104	289	140	145	43	149
HD 18391	1	137	258	222	256	248	212	108	222
	2	86	168	141	198	164	141	72	150

Note. Listed are the values for reduced spectra both before and after removing telluric lines (indicated by the column "Tell", 1 for before and 2 for after). See section 2.2.2 for more details.

Figure 2.1 An example of two-dimensional raw images of illuminated dome flat.

may slightly change during the relatively long integration times for the GC-Cepheids, some of the subtracted images show residual backgrounds which were removed when we extract one-dimensional spectra using the apall task in the IRAF. Wavelength was calibrated using telluric absorption lines in the spectra of telluric standard stars taken before or after the target spectra with the same instrumental settings. Next we traced the continuum levels of all spectra in the same process, removing the broad absorption lines of hydrogen in telluric stars. Spectra processed by these procedures were combined into a single spectrum for each target. The telluric absorption lines of the target were subtracted using a spectrum of the corresponding telluric standard (Table 2.1). Finally, radial velocities were estimated by comparing the observational and synthesized spectra. Figure 2.3 shows a section of the resultant spectra. Cooler stars clearly show more absorption lines.

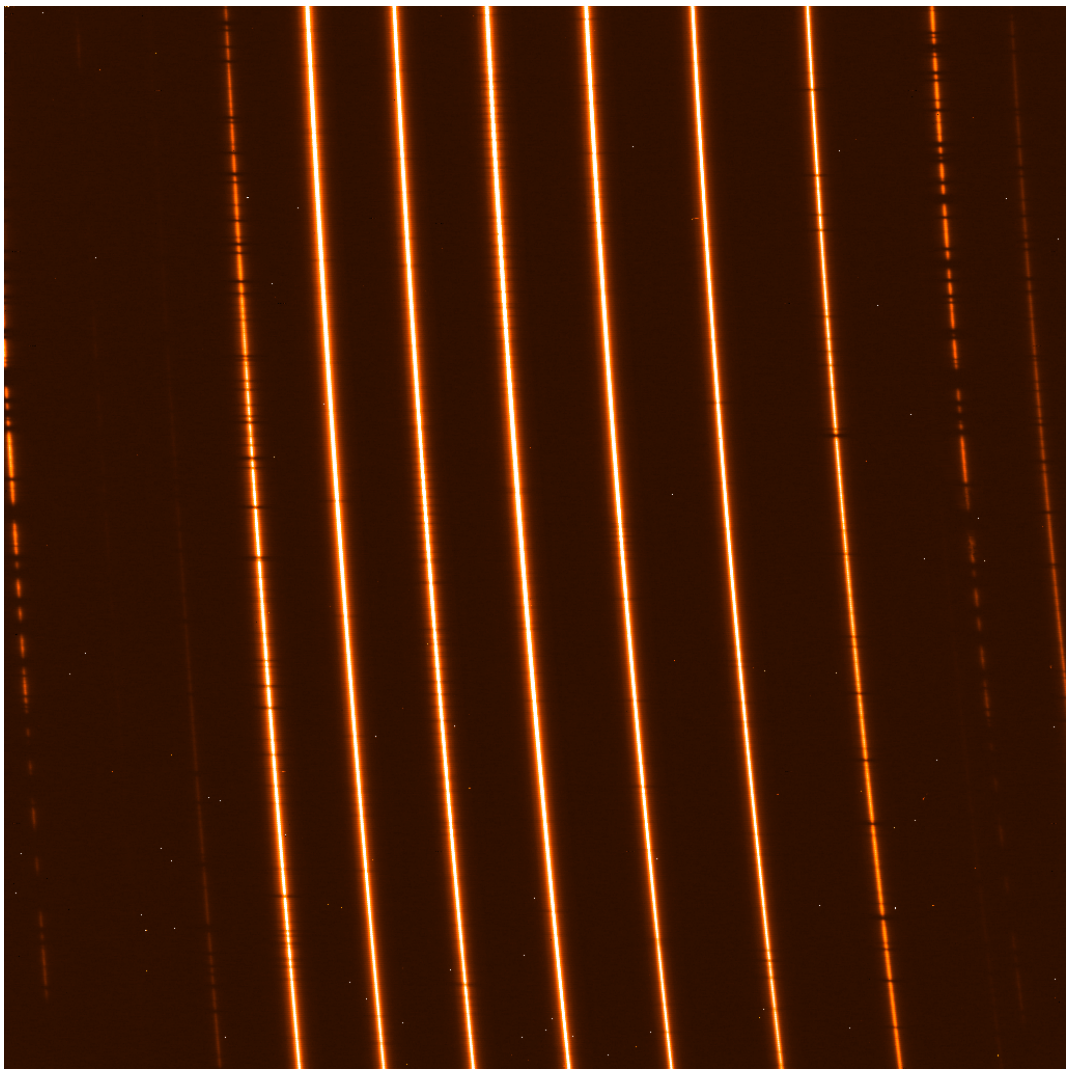

Figure 2.2 An example of two-dimensional raw images of stars; 1 sec integration of δ Cep.

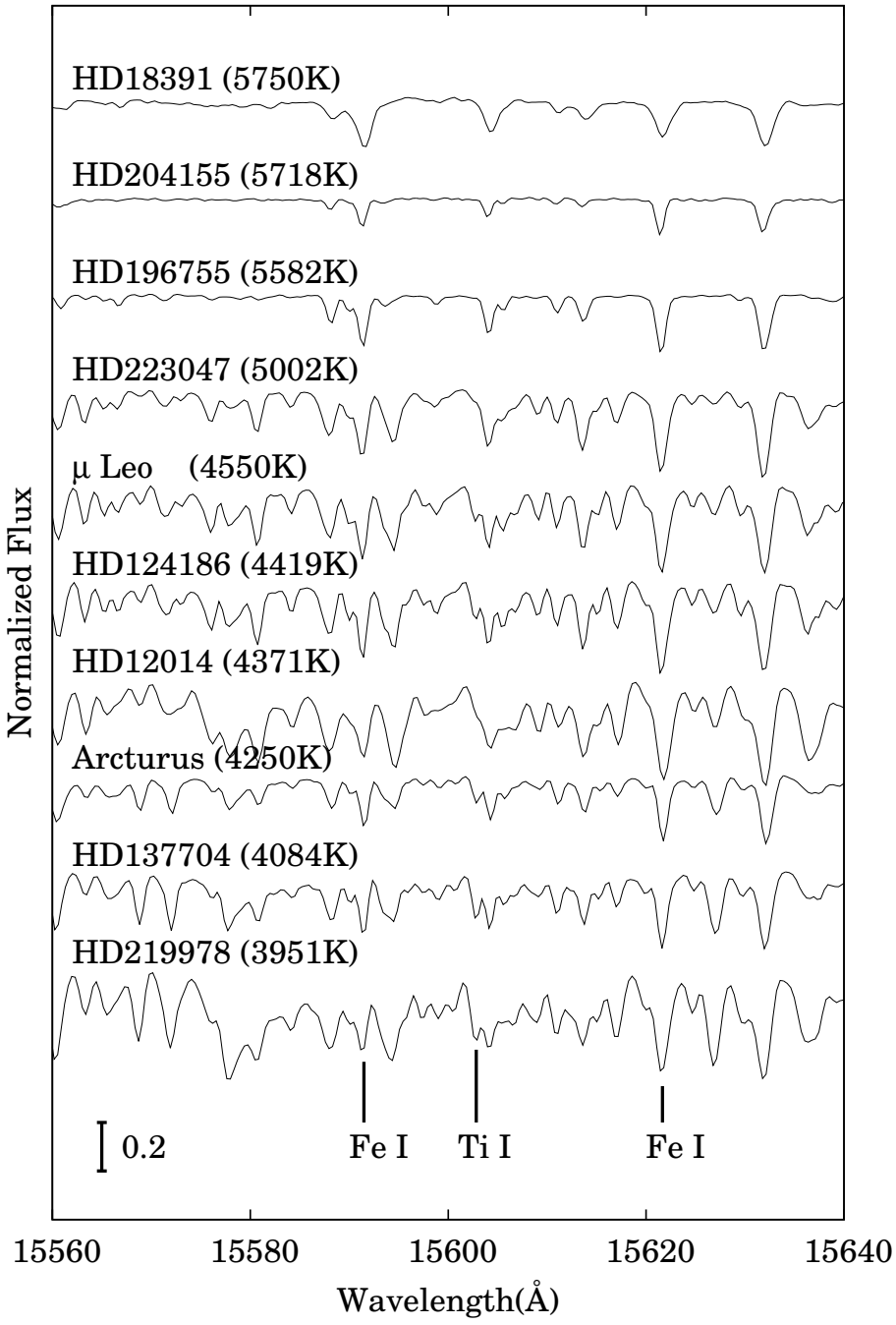

Figure 2.3 A part of the reduced spectra after the continuum normalization and the removal of telluric absorption lines. The spectra of the 10 static calibrating stars are shown in order of the effective temperature as indicated in the panel. Three lines selected for the LDR indicators (Chapter 4) are indicated in the bottom.

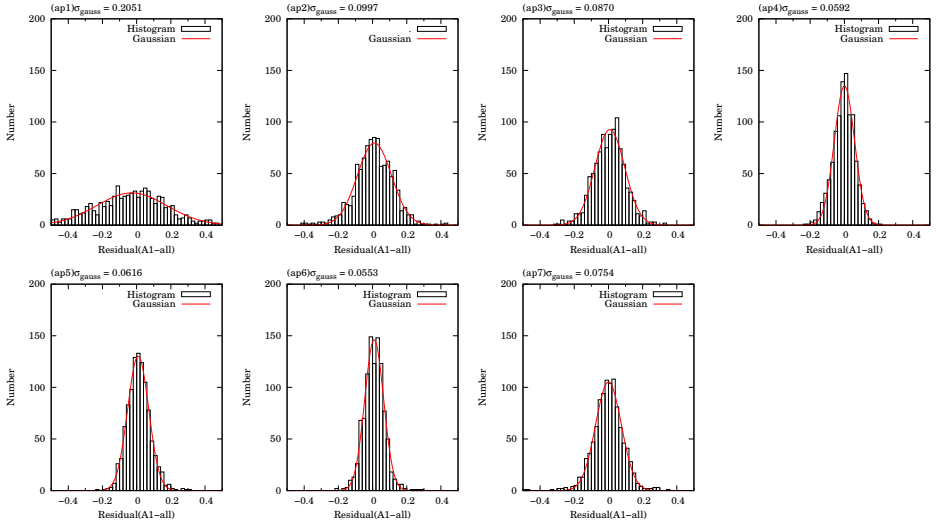

Figure 2.4 Histograms of pixel-to-pixel differences between a single normalized spectrum and the final spectrum. Each panel shows a histogram for each echelle order (ap1 = 38th order to ap7 = 32nd order). This example is for the case of GCC-a; the S/N of each integration is relatively low, ∼40.

2.2.2 Estimation of signal-to-noise ratio

Since the normalized spectra of telluric standard stars have broad flat regions without prominent metal lines, we can estimate their signal-to-noise ratios (S/N = $1/\sigma$, where σ is the noise at the continuum level of the normalized spectrum) in the flat parts. However, the noise levels of late-type stars are difficult to estimate in this way because the spectra contain many absorption lines and few flat regions. Thus we estimated a realistic S/N by the following method. First, we took differences between two paired spectra of the AB sequences. For example, comparing the i-th normalized spectrum $\mathrm{A}_i(\lambda)$ of position A and the corresponding spectrum $\mathrm{B}_i(\lambda)$ of position B, the combined noise from both spectra remains in the difference $\mathrm{A}_i(\lambda)-\mathrm{B}_i(\lambda)$. As illustrated in Figure 2.4, such a difference is well represented by a Gaussian noise function which gives an empirical estimate of the noise. Combining the scatters in these differences, σ_i (i = 1 to N_{pair}), we estimated the noise level in the final normalized spectrum as $\sigma = \sqrt{\Sigma\sigma_i^2}/2N_{\mathrm{pair}}$. For each calibrating object, for example, we have two pairs of the AB sequence, giving four integrations in total (i.e., N_{pair} = 2). The noise in the telluric standard was obtained in the same way and combined with that for the corresponding targets. Table 2.3 lists the S/N with and without the noise from the telluric standards taken into account for each order of the spectra. The 38 th order is dominated by strong telluric absorptions and the estimated S/N tends to be low. Also because we did not find useful lines in this order, we do not use this order in the following analysis. In case of GC Cepheids, a noise σ_N in an average of N frames, $\mathrm{M}(\lambda)$, is significantly smaller than those in individual frames $\mathrm{A}_i(\lambda)$. Thus, we consider the difference $\mathrm{A}_i(\lambda) - \mathrm{M}(\lambda)$ as σ_i. Then, we can derive the error in the combined spectra as $\sigma_N = \sqrt{\Sigma\sigma_i^2}/N$. We calculated the average S/N for each object combining those in the 33rd to 37th orders (Table 2.3).

Chapter 3

Abundance analysis of Metal standard stars

As we mentioned earlier in the Introduction, strong interstellar extinction for our Cepheids requires us to make observations in the infrared rather than in the optical (see also section 4.1). Whereas previous abundance measurements of Cepheids have been done by a few groups using optical spectra, the measurement method using infrared spectra has to be established including a calibration with metallic standard stars.

In this chapter we describe the method we developed for determining microturbulence and iron abundances through the analysis of only H-band spectra of the static calibrating stars. In this chapter, we fix effective temperature, surface gravity, and metallicity [M/H] as known values and estimate microturbulence and iron abundance [Fe/H]. The first two sections give basic setups of the method: the software we use, SPTOOL, for handling atmosphere models and synthetic spectra and for measuring iron abundances in section 3.1, and list of absorption lines in the H band in section 3.2. In section 3.3, we discuss how to determine the microturbulence. Finally, we present measurements of iron abundances of the 10 calibrating stars and compare the results with literature values in section 3.4.

3.1 SPTOOL

For many applications of interpreting spectra, it is necessary to make use of atmospheric models which describe the structures of stellar atmosphere in terms of temperature, density, and so on. The atmospheric parameters necessary for constructing a stellar atmospheric model include $T_{\rm eff}$ (effective temperature), $\log g$ (logarithmic surface gravity), ξ (microturbulence), and [M/H] (metallicity). We assume that the atmospheric structure is in local thermodynamic equilibrium (LTE), hydrostatic equilibrium, plane parallel and 1–D structures. ATLAS code was developed by R. Kurucz in the 1970s based on these assumptions and one of the current versions, ATLAS9, is still commonly used for the abundance analysis. Kurucz also provides extensive database of atomic and molecular lines. Other widely-used atmospheric models include MARCS (Gustafsson et al., 1975) and PHOENIX (Hauschildt et al., 1997). ATLAS and other models provide grids of atmospheric models with wide ranges of atmospheric parameters, and it is possible to interpolate these models for creating one with a given

parameter set. In this thesis, we make use of ATLAS9 atmosphere models.

For calculating model atmospheres and synthesizing spectra we make use of SPTOOL[1] which has been developed by Y. Takeda. This tool has been used for chemical abundance analysis by many investigators (e.g. Takeda, 1995; Takeda et al., 2013; Notsu et al., 2013). SPTOOL utilizes the program routines of ATLAS9 package by Kurucz. Table A.1 shows the solar abundance ratio assumed in this thesis together with those in some references. SPTOOL implements an interactive task called SPSHOW which synthesizes and draws a spectrum for a given parameter set including a microturbulence ξ (km/s), a macroturbulent velocity ζ (km/s), chemical compositions and a wavelength resolution.

The iron abundance determinations are carried out using MPFIT, a tool to search for the best synthetic spectrum, also developed by Y. Takeda. MPFIT also works within the framework of SPTOOL and searches the best match between the theoretical and observational spectra, by iteratively varying the abundance, the broadening parameter and the radial-velocity shift for a relatively narrow range of spectrum. We used a width of 3 Å for each MPFIT run in the following analysis. It computes synthetic spectra, with a given atmosphere model, a microturbulence, and iteratively varying abundances of target elements. Synthesized spectra are convolved with an assumed broadening function including the instrumental profile. MPFIT searches for an optimal solution which gives the smallest residual between the logarithmic quantities of model fluxes $\eta_i(T, \log g, [\mathrm{M/H}], \xi, \zeta)$ and observed fluxes y_i,

$$\sigma^2 = \sum_{i=1}^{N} (y_i - \eta_i - C)^2 / N, \tag{3.1}$$

where N is the number of pixels used in the comparison and C is a constant offset reflecting the difference of units between model and observed fluxes (Takeda, 1995). The estimate includes an iteration process, 10 times, of varying the iron abundance, broadening macroturbulent velocity together with instrumental profile. The atmosphere model and the microturbulence are fixed during the iteration.

The solar abundances used in SPTOOL is adopted from Anders & Grevesse (1989) except the iron abundance which is assumed to be $\log \epsilon(\mathrm{Fe}) = 7.50$. These abundances are different from the recent results (Asplund et al., 2009), and we discuss this effect in section 3.5.

[1] http://optik2.mtk.nao.ac.jp/~takeda/sptool/

Table 3.1. List of major catalogs which include absorption lines in the near infrared.

Catalog	Reference
Robert Kurucz Database	http://kurucz.harvard.edu/
NIST Atomic Spectra Database	http://www.nist.gov/pml/data/asd.cfm
Vienna Atomic Line Database (VALD)	http://vald.astro.univie.ac.at/~vald/php/vald.php
R09	Ryde et al.(2009)
M99	Meléndez & Barbuy(1999)

3.2 Linelist in the infrared wavelength

Calculating synthetic spectra requires a list of absorption lines, which typically includes wavelengths, excitation energies of lower state of the transition, line-strengths, and more. Line strengths are represented by $\log gf$ which combines oscillator strength, f, and statistical weights of the upper level of the transition, g. Table 3.1 summarizes previous catalogs with absorption lines in the infrared. Some of these adopted the values based on theoretical calculation. Meléndez & Barbuy (1999, hereafter M99) calibrated $\log gf$ values of lines at 14900–18000 Å based on the solar spectrum ($\lambda/\Delta\lambda = 300,000$; Wallace et al., 1996), while Ryde et al. (2009, R09) calibrated those of relatively strong Fe lines at 15326–15705 Å based on the spectrum of Arcturus, a prototype K-type giant. We decided to use the linelist of M99 as we discuss below. Late-type stars also show many molecular lines, progressively stronger toward lower temperatures. The main molecules making absorptions in H band are OH, CN and CO (Coelho et al., 2005). We adopted a linelist of these molecules compiled by Kurucz Database[2]. Figure 3.1 illustrates absorption lines of Fe, CN, CO and OH, separately, by synthesizing absorption spectra with individual species only.

We compared spectra synthesized by using two linelists, M99 with VALD[3]. Both of these lists cover the entire range of H band. 800 and 5553 Fe I lines between 14600 and 17900 Å are listed in M99 and VALD, respectively. VALD has a larger number of lines because they include theoretically calculated lines. In contrast, M99 listed lines that were clearly recognized in the high-resolution spectrum of the Sun. We examined the excitation potential (EP) and $\log gf$ values in the two lists for each of the lines listed in M99 (Figure 3.2). The excitation potentials in the two are almost identical. Most of Fe I lines present in H band have relatively high excitation potentials (EP $= 5 \sim 7$ eV). In contrast, the comparison the $\log gf$ values shows a scatter; the $\log gf$ in M99 tend to be larger than those in VALD. The difference in oscillator strengths directly affects predicted model spectra and inferred metallicities. For example, Figure 3.3 compares observed high-resolution Arcturus spectrum ($\lambda/\Delta\lambda = 100,000$; Hinkle et al., 1995) and model spectra synthesized by using the two linelists. We adopted atmospheric parameters and chemical composition of Arcturus from Smith et al. (2013). This figure indicates that, at least with the adopted parameters, the list of M99 reproduces the observed spectra better than VALD.

We then investigated the effects of the linelist on $\log \epsilon$(Fe) values from individual absorption lines.

[2]http://kurucz.harvard.edu/linelists/linesmol/

[3]We used VALD2 database. The most recent version of VALD is available at http://vald.astro.uu.se.

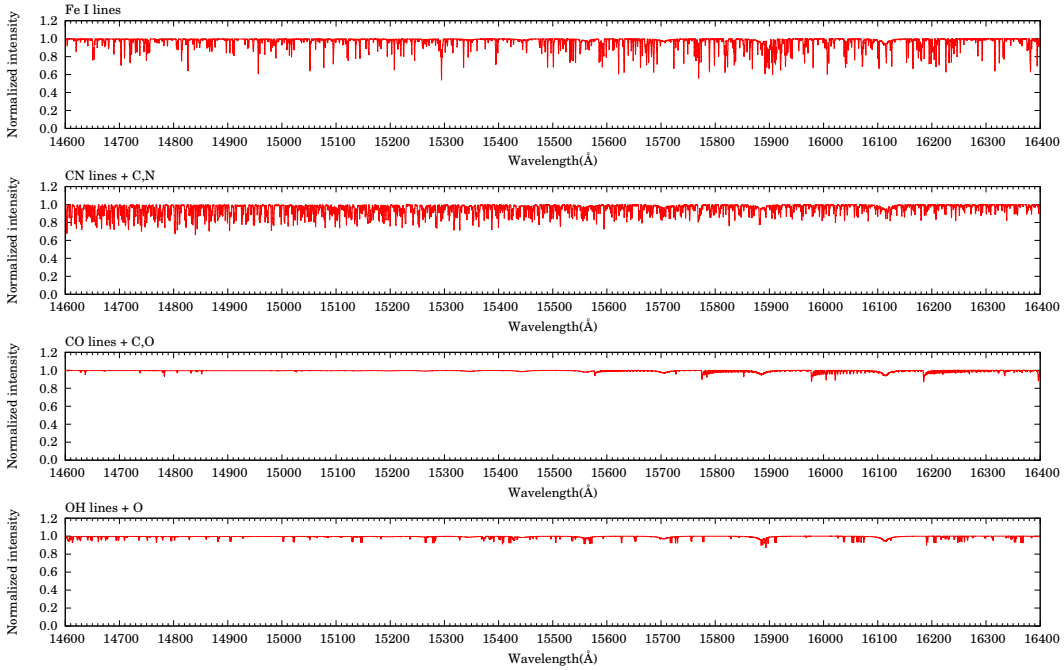

Figure 3.1 Fe I lines and molecular bands (CO, CN, OH) in H band are illustrated using synthetic spectra with only individual elements included. Fe lines are taken from M99, while molecular line data are adopted from Kurucz Database.

Statistical errors in $\log gf$ would lead to a large line-by-line dispersion among the resultant $\log \epsilon$(Fe) values. Here we selected 20 unblended lines found in our spectrum of μ Leo to measure $\log \epsilon$(Fe) with the two calibrations. Considering that the microturbulence affecting the measurements is not necessarily same in the optical and in the infrared spectra, we considered five different ξ between 1.0 and 2.5 km/s. With $\xi = 1.8$ km/s (the value found in Smith et al., 2013), the abundances of μ Leo were estimated to be 7.66 dex with the VALD calibration and 7.79 dex with that of M99. The standard deviations were $\pm$0.32 and $\pm$0.23 dex respectively. The M99 calibration gives a smaller scatter than the VALD. There is a $\sim 1\sigma$ difference between the metallicity scales defined by the two line lists. This conclusion does not depend on the ξ. In this study, we adopt the $\log gf$ values calibrated by M99. We discuss the metallicity scale in comparison with previous measurements in section 3.4.

We examined the spectra of μ Leo in order to identify absorption lines which can be used for the iron abundance measurement in our analysis. We selected 95 Fe I lines (Table 3.2) based on the following criteria: (1) the line is as unblended as possible, and (2) there are no telluric lines severely affecting the stellar absorption line.

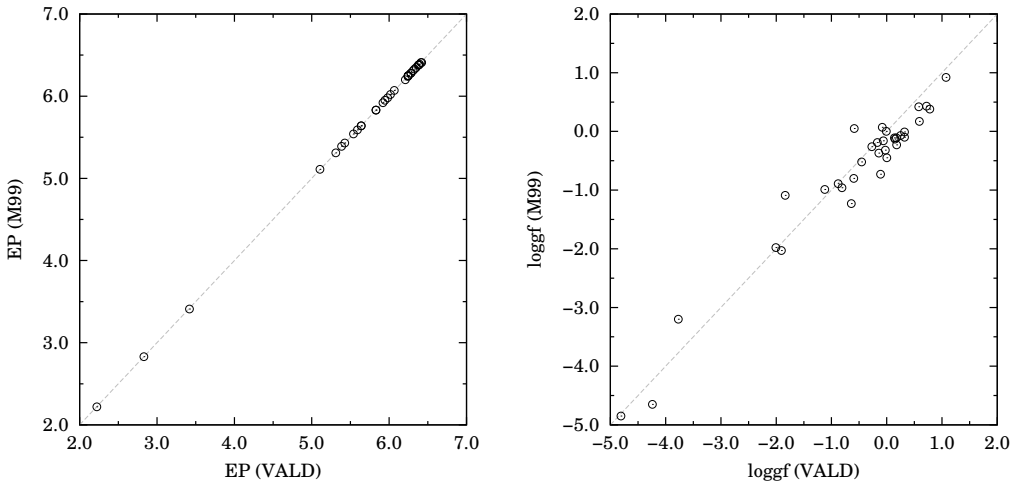

Figure 3.2 Comparison of $\log gf$ and excitation potential (EP) for common lines in the two linelists, VALD and Meléndez & Barbuy (1999).

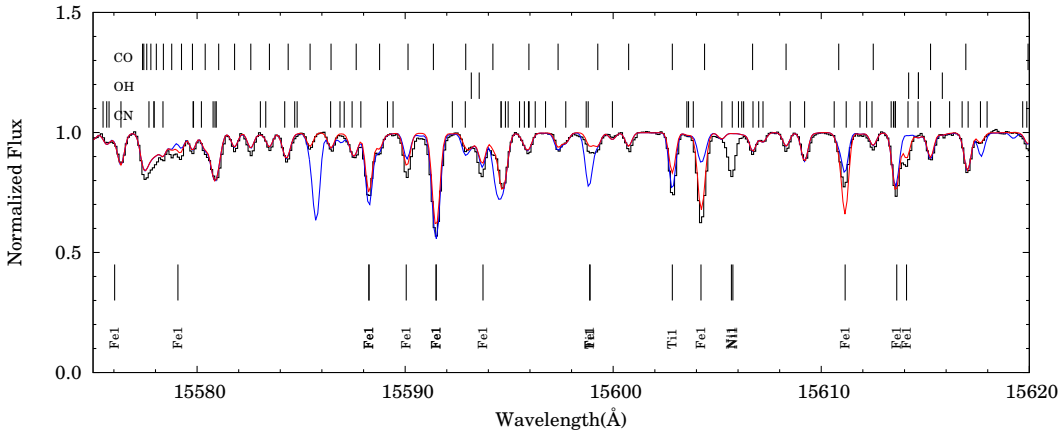

Figure 3.3 An observed spectrum of Arcturus ($\lambda/\Delta\lambda = 100,000$; Hinkle et al., 1995) indicated by black curve is compared with synthetic spectra with VALD (blue) or M99 (red) used.

Table 3.2. Selected Fe I lines used for measuring $\log \epsilon$(Fe).

ID	λ (Å)	EP (eV)	$\log gf$	s/w	ID	λ (Å)	EP (eV)	$\log gf$	s/w
H1	15112.33	6.26	−1.01		H35	16178.02	6.38	−0.52	w
H2	15194.50	2.22	−4.85		H36	16182.20	6.32	−0.90	
H3	15207.54	5.39	−0.10	s	H37	16195.08	6.39	0.12	
H4	15219.62	5.59	−0.25	s	H38	16198.51	5.41	−0.60	
H5	15294.56	5.31	0.43	s	H39	16204.27	6.32	0.06	
H6	15301.56	5.92	−0.84		H40	16207.77	6.32	0.36	
H7	15524.30	5.79	−1.51		H41	16213.56	6.28	0.04	w
H8	15534.26	5.64	−0.47		H42	16225.64	6.38	−0.03	
H9	15542.09	5.64	−0.70	w	H43	16231.67	6.38	0.42	
H10	15560.78	6.35	−0.55		H44	16235.98	5.92	−0.45	
H11	15566.72	6.35	−0.50		H45	16246.47	6.28	−0.27	w
H12	15571.74	6.32	−0.90		H46	16252.57	6.32	−0.50	
H13	15604.22	6.24	0.28		H47	16284.79	6.40	0.07	w
H14	15621.65	5.54	0.17	s	H48	16292.85	5.92	−0.62	
H15	15631.95	5.35	−0.15	s	H49	16316.35	6.28	0.92	s
H16	15645.01	6.31	−0.54		H50	16324.46	5.39	−0.66	
H17	15648.52	5.43	−0.80		H51	16331.53	5.98	−0.61	
H18	15652.87	6.25	−0.19		H52	16440.42	6.29	−0.36	
H19	15662.01	5.83	0.00		H53	16444.84	5.83	0.21	
H20	15677.02	6.25	−0.73		H54	16466.94	6.39	0.00	
H21	15686.44	6.25	0.02		H55	16486.69	5.83	0.38	s
H22	15853.31	5.96	−0.80		H56	16492.10	6.61	−0.59	
H23	15863.74	6.26	−0.04		H57	16494.45	6.39	−0.53	
H24	15868.52	5.59	−0.26	s	H58	16517.25	6.29	0.37	
H25	15878.45	5.62	−0.61		H59	16519.43	6.39	−0.40	
H26	15892.41	6.31	0.08		H60	16522.10	6.29	−0.19	
H27	15895.23	6.26	0.20		H61	16524.49	6.34	0.47	
H28	15898.02	6.31	0.00	w	H62	16541.43	5.95	−0.58	
H29	15904.35	6.36	0.25		H63	16552.02	6.41	−0.01	
H30	15906.04	5.62	−0.34		H64	16586.06	5.62	−1.53	w
H31	15971.25	6.41	−0.41		H65	16645.88	5.96	−0.34	
H32	15980.73	6.26	0.60	s	H66	16648.24	6.55	−0.45	
H33	16153.25	5.35	−0.82	w	H67	16693.11	6.42	−0.41	w
H34	16165.05	6.32	0.73	s	H68	16739.30	6.38	−0.97	

(continues)

Table 3.2 (continued)

ID	λ (Å)	EP (eV)	$\log gf$	s/w	ID	λ (Å)	EP (eV)	$\log gf$	s/w
H69	16783.04	6.30	−0.94		H83	17469.92	6.41	−0.71	
H70	16792.25	6.35	−1.09		H84	17473.42	6.41	−1.05	
H71	16794.22	6.57	−0.43		H85	17478.03	6.64	0.11	
H72	16799.66	5.87	−0.74		H86	17516.09	6.64	−0.31	
H73	16822.70	5.11	−2.45		H87	17538.64	5.72	−1.22	
H74	17011.11	5.95	−0.24		H88	17554.15	6.45	−0.56	
H75	17027.62	6.62	−0.67		H89	17581.92	6.38	−0.55	
H76	17037.79	6.39	−0.42		H90	17683.92	6.34	0.00	
H77	17052.20	6.39	−0.60	w	H91	17706.67	5.97	−0.66	
H78	17067.67	6.37	−0.17		H92	17721.09	6.58	0.45	
H79	17161.12	6.02	−0.32	w	H93	17728.13	6.58	0.34	w
H80	17166.20	5.95	−0.79		H94	17747.35	5.92	−0.76	
H81	17302.33	6.07	−0.11	w	H95	17771.13	5.95	−0.07	
H82	17310.26	6.32	−0.90						

Note. The parameters, wavelength (λ), excitation potential (EP) and line strengths ($\log gf$), are adopted from M99. The lines with s (strong) and w (weak) flag in the "s/w" column or used for determining the microturbulence (see section 3.3 for details).

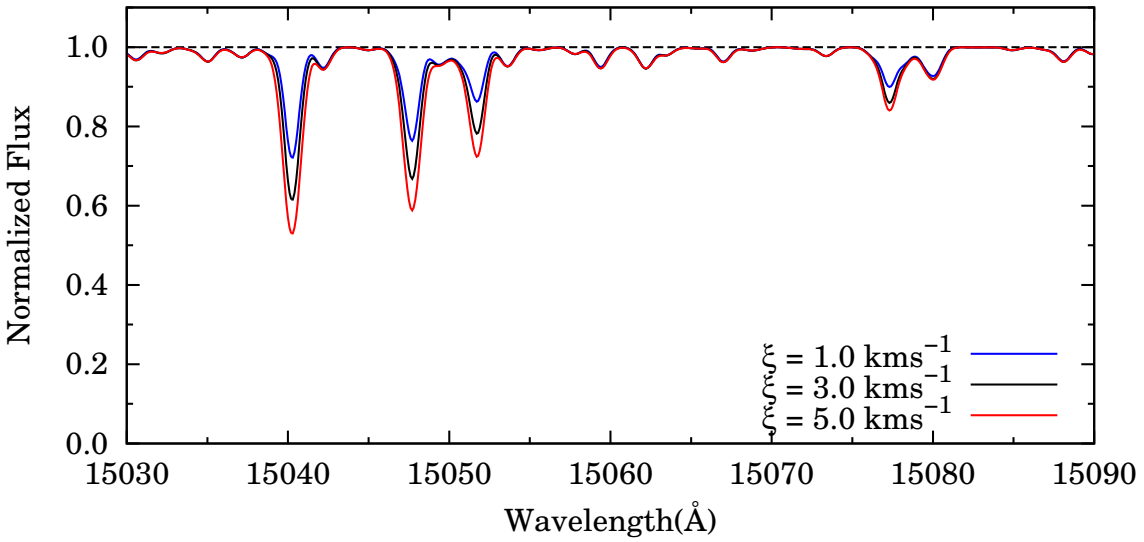

Figure 3.4 Variation of absorption line strength in synthetic spectra with increasing microturbulence (from ξ = 1.0, 3.0 and 5.0 km/s). The effect of microturbulence ξ is clearly seen for strong absorption lines while not evident for weak lines.

3.3 The determination of microturbulence

An important, though not well-understood, parameter which characterizes spectra is microturbulence. Observed absorption lines are broadened by two turbulent velocities, microturbulence and macroturbulent velocity, in addition to other factors including an instrumental line-spread function. The macroturbulent velocity is considered for turbulent-like (random) motions of atmosphere components larger than line forming region. It broadens the absorption line but does not give a significant effect on abundance analysis. The microturbulence ξ, on the other hand, is considered as motions of micro non-thermal components in the line-forming region. It not only broadens line profiles but may also increase equivalent widths (Mucciarelli, 2011). Because it is difficult to determine its effects in modeling atmospheres and spectral synthesis from physical principles, the microturbulence is treated as a free parameter. Determination of this parameter is a crucial part because it tends to give a significant effect on the measurement of abundances.

As an example, we plot synthetic spectra with different ξ (1.0, 3.0, 5.0 km/s) in Figure 3.4. This figure clearly indicates that strong lines are greatly affected by microturbulence but weak lines are not. An improperly large ξ would lead to underestimates of abundance in case of strong lines. The top panel of Figure 3.5, ξ–log ϵ(Fe) plot (log ϵ(Fe) = log N_{Fe}/ log N_H + 12), clearly illustrates such effects. We here assume that log ϵ(Fe) values measured by strong lines should agree with those measured by weak lines if the microturbulence together with other parameters like temperature and surface gravity are appropriate.

We search the ξ value of the cross-point between strong lines and weak lines as we describe below, while previous method based on the ξ–log ϵ(Fe) plot mainly considers the standard deviation of log ϵ(Fe) values from all lines measured (e.g., Saffe & Levato, 2004). As a guide of line strengths, we use X factor

adopted from Gratton et al. (2006),

$$X = \log gf - \mathrm{EP} \times \frac{5040}{0.86 \times T_{\mathrm{eff}}}, \tag{3.2}$$

where the coefficient 0.86 may be slightly different in different literature. We selected Fe lines with X> -6 (calculated with the solar temperature $T_{\mathrm{eff}} = 5777$ K) as strong lines, and those with X< -6 as weak lines. Among Fe I lines found in our spectra, we selected ten strong lines which show significantly large variations of $\log \epsilon$(Fe) as a function of ξ, and 13 relatively weak lines which show weak variations if any (Table 3.2).

Figure 3.5 illustrates our method of determining ξ. We derive the abundances of Fe I lines in the range of microturbulence from 1 to 7 km/s. The $\log \epsilon$(Fe) for each line is obtained by fitting synthetic spectra with the help of MPFIT as described in section 3.1. As the atmospheric parameters of the standard stars, we used reference values listed in Table 2.1. The top panel of Figure 3.5 shows variation of the abundances against the microturbulence. The variations for the strong and weak lines are indicated by black and gray curves, respectively, of which the former have larger slopes. Median variations are drawn for the two groups in the middle panel, while the bottom panel plots the difference of the two curves. The two curves in the middle panel meet at $\xi = 2.25$ km/s, giving the zero residual in the bottom. As the best estimate, we take the ξ value at which the residual curve diminishes, i.e. 2.25 km/s in this case and consider the range of ξ, where the residual is zero within the 1 σ as the error of the estimate. The typical error of ξ is 0.5 km/s. The results for other objects are presented in Appendix B (Figures B.1–B.9).

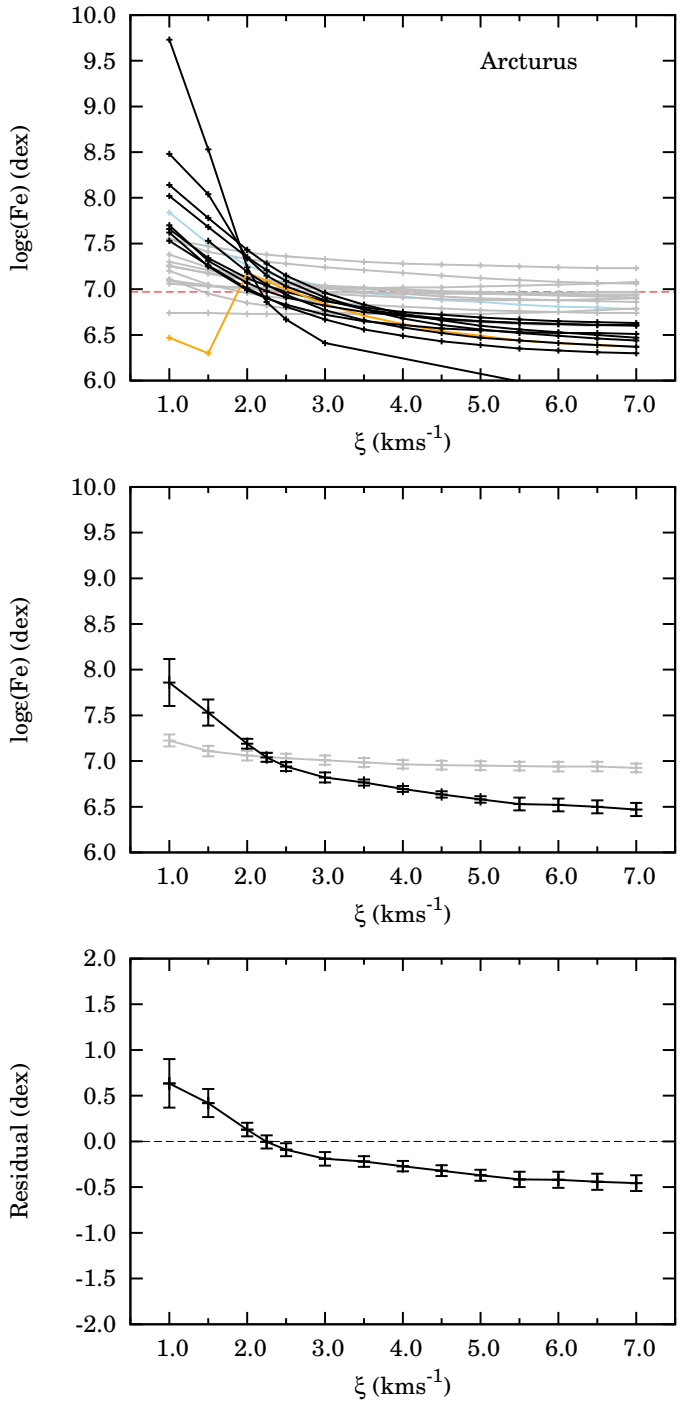

Figure 3.5 The ξ–$\log\epsilon$(Fe) plot for Fe I abundance of Arcturus. The top panel shows variation of abundances from individual lines. Black and gray curves indicate the variations obtained for strong and weak lines, respectively, but colored curves indicate rejected ones. Median curves for the two groups are drawn in the middle panel, and their difference in the bottom.

3.4 Abundance analysis of metal standard stars

3.4.1 Iron abundance determination with H-band spectra

With the microturbulence derived as in the previous section, we measure $\log \epsilon$(Fe) with a larger number of Fe I lines and take their mean for each object. Instead of simply taking the mean, we consider histograms of $\log \epsilon$(Fe) values from individual lines and fit Gaussian functions to determine the iron abundance as shown in Figure 3.6. The middle panel indicates our best estimate of $\log \epsilon$(Fe) for this example, 7.05 dex, or Arcturus. The standard error of this iron abundance is estimated to be 0.02 dex by dividing the σ value of the Gaussian by the square root of its area which corresponds to the number of lines involved. Table 3.3 provides our estimates of iron abundances and the errors for the 10 metal standard stars. Plots similar to Figure 3.6 are given in Appendix B for the all objects. A typical standard error in $\log \epsilon$(Fe) is 0.03 dex. This is regarded as a statistical error under a given set of the atmospheric parameters and other parameters.

We then consider an error of iron abundances caused by uncertainty in atmospheric parameters, i.e. microturbulence, effective temperature, and surface gravity. Constructing atmospheric models with varying the adopted parameters one-bye-one by an error size of each parameter, we repeated the iron abundance measurements to estimate the effect of varying the atmospheric parameters. For example, the top and bottom panels on the right side of Figure 3.6 show the estimates done with the microturbulences shifted by the error size, 0.25 km/s. As listed in Table 3.3, most of the errors taking individual atmospheric parameters into account are smaller than 0.1 dex. We consider these uncertainties as independent and derived a total error by $\sigma_{\rm all} = \sqrt{\sigma^2_{\Delta T} + \sigma^2_{\Delta G} + \sigma^2_{\Delta \xi}}$, which leads to the typical total uncertainty of 0.1 dex for the calibrating stars.

3.4.2 Comparison with the iron abundances in literature

Figure 3.7 shows a comparison between our iron abundance and those in Prugniel et al. (2011). Although there seems to be a systematic offset especially in the low-metal range, the abundances of three stars are consistent within 1 σ error and those of other three within 2 σ error. Figure 3.8 plots the results together with other previous estimates (see Appendix B Table B.1 for each value). There is a scatter of $\pm$0.1 dex or larger for each star. While our values are within the scatters, for Arcturus and μ Leo in particular, also seen is a small offset of ours being slightly high. As we mentioned earlier, the microturbulence has an important and direct effect on the iron abundance estimation. For Arcturus and μ Leo, unlike the others, we can find many papers reporting both ξ and $\log \epsilon$(Fe). Figure 3.9 plots the iron abundance estimates against the accompanying ξ in the literature. It is seen that the estimates of the microturbulence and iron abundance are anti-correlated.

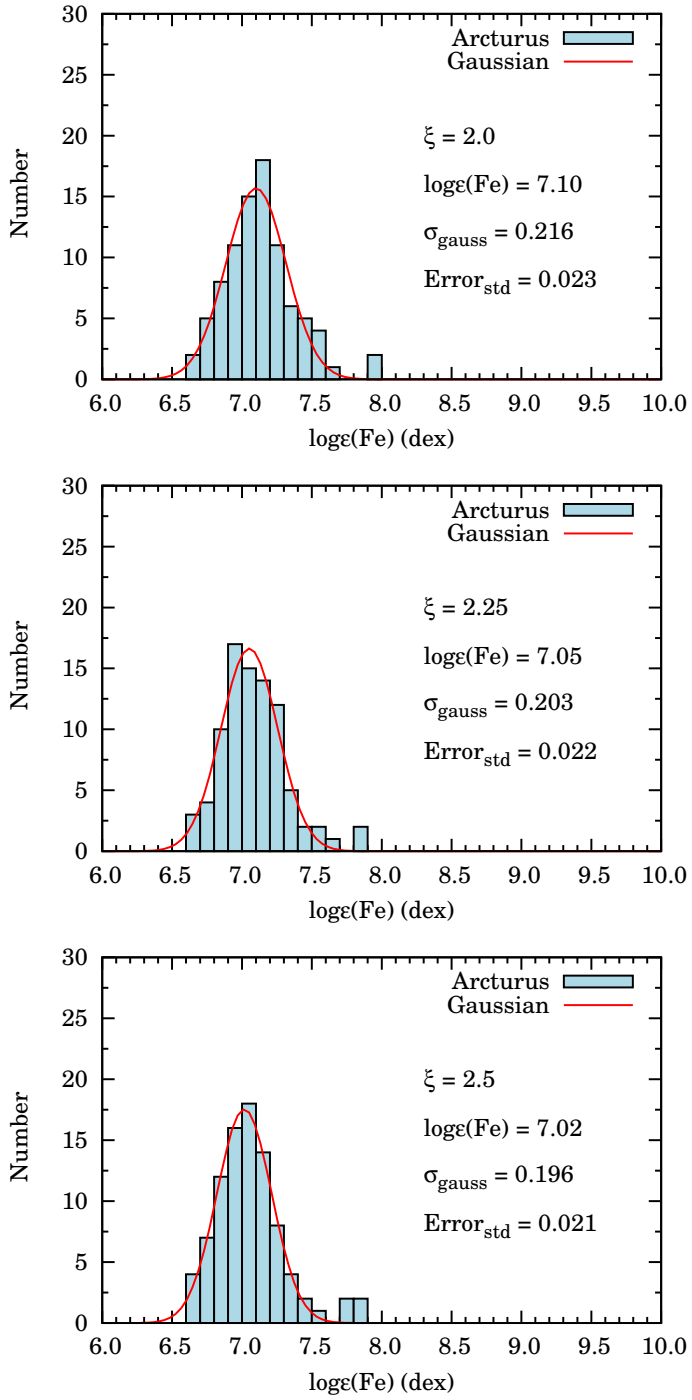

Figure 3.6 Histograms of $\log \epsilon(\mathrm{Fe})$ values from individual lines for Arcturus. Red curves indicate fitted Gaussian functions. Different ξ values are assumed in three panels, of which the middle indicates the result with our best estimate of ξ.

Table 3.3. List of our estimates of ξ and [Fe/H].

Object	$T_{\rm eff}$ (K)	$\log g$ (dex)	ξ (km/s)	[Fe/H] (dex)
HD 219978	3951±55	0.57±0.18	$3.50^{+0.50}_{-0.50}$	0.02±0.03
HD 137704	4084±42	1.97±0.21	$2.25^{+0.25}_{-0.25}$	−0.20±0.02
Arcturus	4280±60	1.70±0.13	$2.25^{+0.25}_{-0.25}$	−0.45±0.02
HD 12014	4371±108	0.66±0.16	$4.00^{+0.50}_{-0.50}$	−0.05±0.03
HD 124186	4419±59	2.66±0.17	$2.50^{+0.50}_{-0.50}$	0.32±0.03
μ Leo	4466±54	2.65±0.15	$2.50^{+0.50}_{-0.50}$	0.28±0.03
HD 223047	5002±50	1.26±0.09	$3.50^{+0.50}_{-0.50}$	0.23±0.02
HD 196755	5582±31	3.64±0.07	$2.50^{+0.50}_{-0.50}$	0.14±0.01
HD 204155	5718±56	3.93±0.11	$2.25^{+0.75}_{-0.25}$	−0.48±0.02
HD 18391	5750±60	1.20±0.13	$5.25^{+2.25}_{-1.75}$	0.04±0.04

Note. This is together with $T_{\rm eff}$ and $\log g$ from Prugniel et al. (2011). The errors of [Fe/H] are statistical ones from the Gaussian fits.

Table 3.4. Effects of changing atmospheric parameters on [Fe/H] (see text for details).

Object	$\sigma_{-\Delta T}$ (dex)	$\sigma_{+\Delta T}$ (dex)	$\sigma_{-\Delta G}$ (dex)	$\sigma_{+\Delta G}$ (dex)	$\sigma_{-\Delta \xi}$ (dex)	$\sigma_{+\Delta \xi}$ (dex)	σ_{all_-} (dex)	σ_{all_+} (dex)
HD 219978	0.01	0.00	0.01	−0.01	0.09	−0.08	0.09	0.10
HD 137704	0.02	−0.01	−0.02	0.03	0.06	−0.04	0.05	0.07
Arcturus	−0.01	0.01	−0.02	0.02	0.05	−0.03	0.04	0.06
HD 12014	−0.03	0.06	−0.01	0.00	0.04	−0.03	0.05	0.08
HD 124186	0.01	−0.01	−0.01	0.01	0.10	−0.08	0.09	0.10
μ Leo	0.01	0.00	0.00	0.01	0.12	−0.09	0.09	0.12
HD 223047	−0.02	0.07	0.01	0.00	0.10	−0.05	0.06	0.12
HD 196755	−0.01	0.03	0.01	0.00	0.07	−0.04	0.04	0.08
HD 204155	−0.02	0.03	0.01	0.00	0.01	−0.03	0.04	0.04
HD 18391	0.00	0.02	0.02	0.03	0.04	−0.03	0.05	0.07

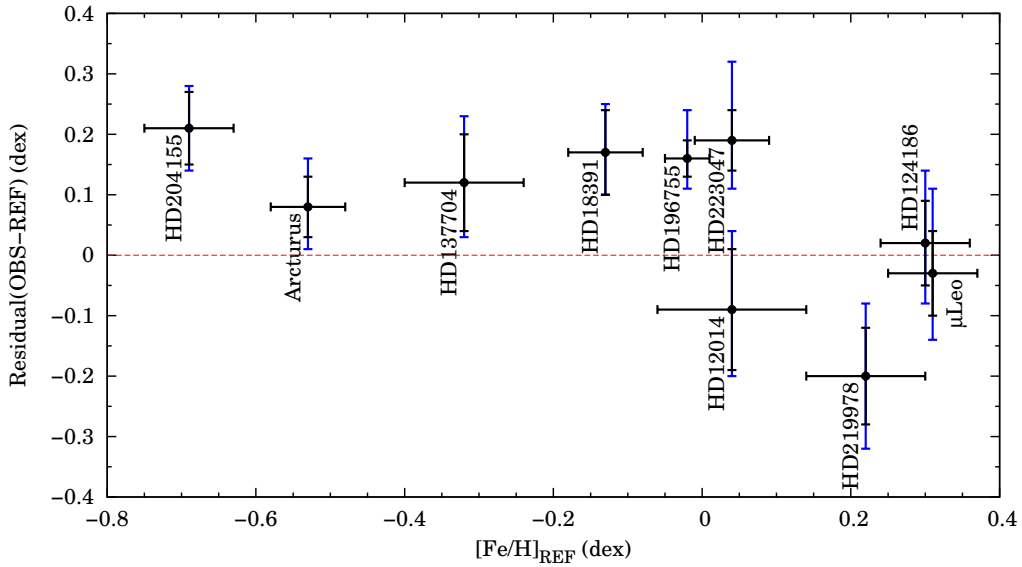

Figure 3.7 The residual ([Fe/H]−[Fe/H]$_{\rm REF}$) as a function of iron abundance. Black bars include only standard errors, while blue ones include the uncertainty from atmospheric parameters.

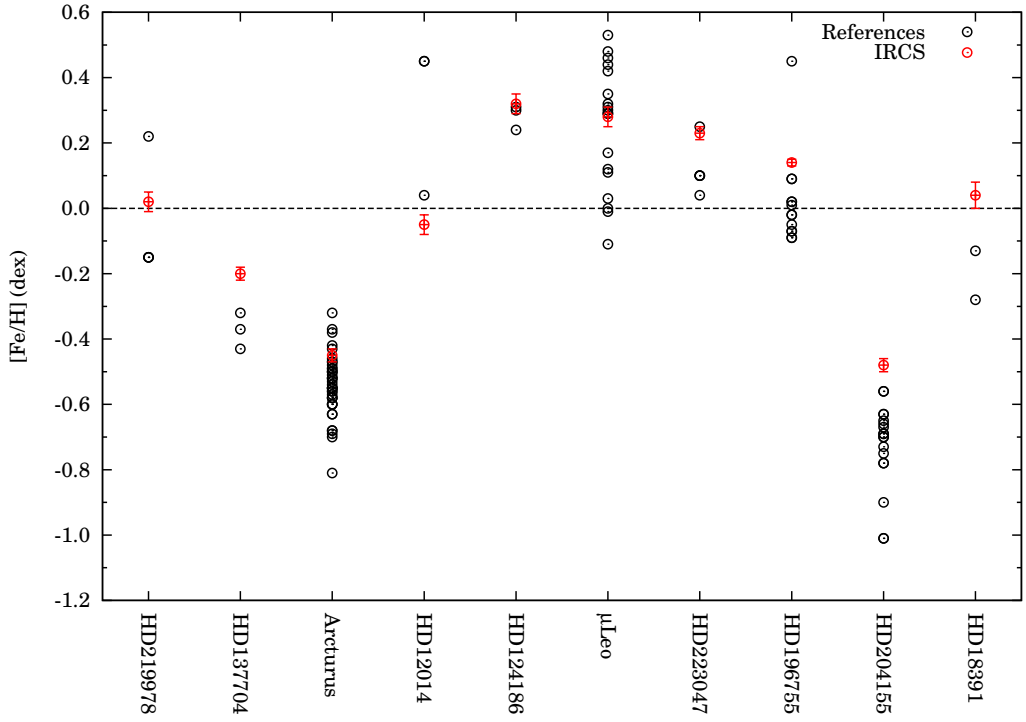

Figure 3.8 Comparing our results, indicated by red points, with literature values.

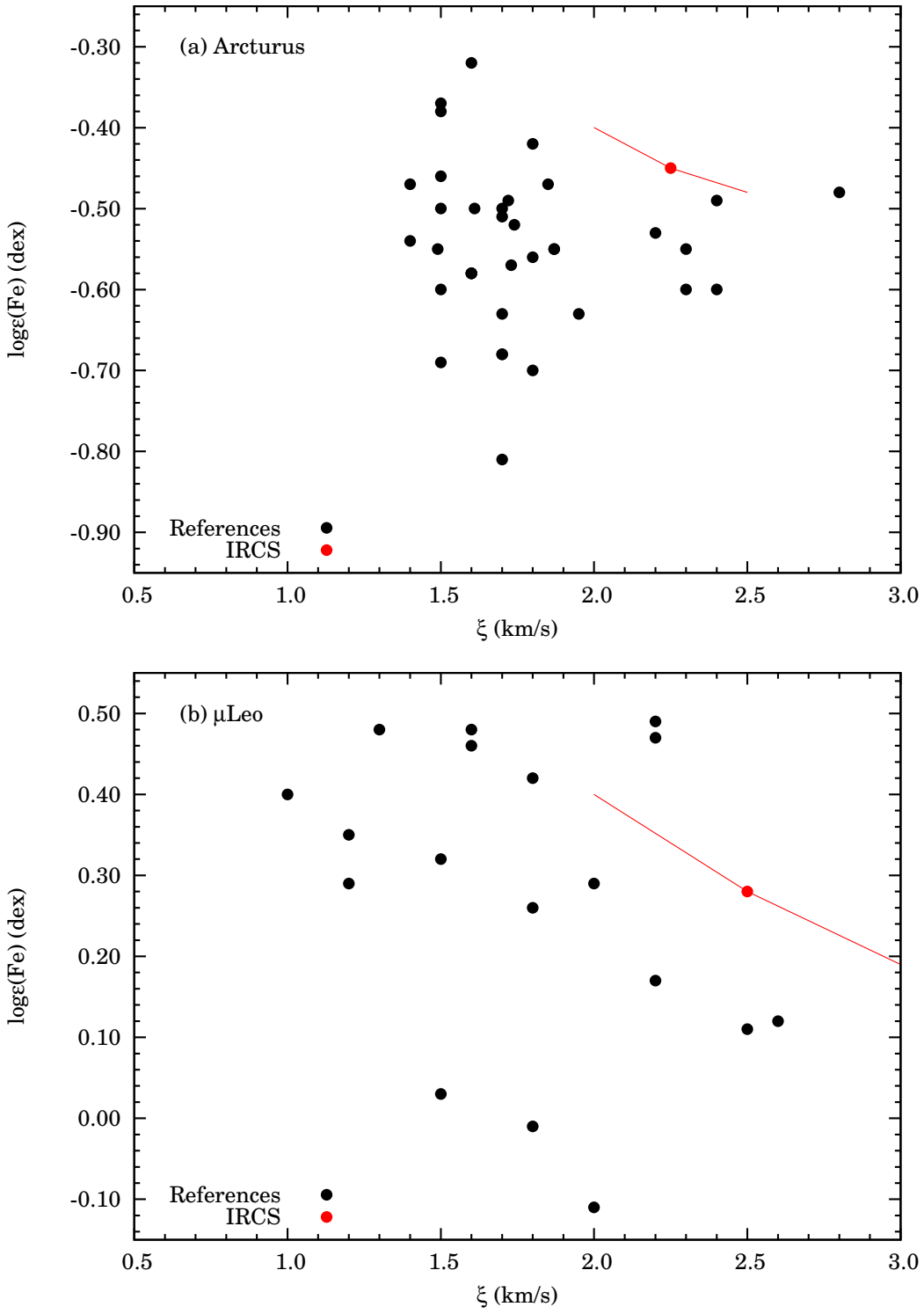

Figure 3.9 Comparing our derived iron abundances and ξ with other reference values for Arcturus (top) and μ Leo (bottom). Red points and lines indicate our results and errors.

Table 3.5. The mass fractions of H(X), He(Y) and metals(Z) from some literature.

Source	X	Y	Z	Z/X
Anders & Grevesse (1989)	0.7314	0.2485	0.0201	0.0274
Grevesse & Noels (1993)	0.7336	0.2485	0.0179	0.0244
Grevesse & Sauval (1998)	0.7345	0.2485	0.0169	0.0231
Lodders (2003)	0.7491	0.2377	0.0133	0.0177
Asplund, Grevesse & Sauval (2005)	0.7392	0.2485	0.0122	0.0165
Lodders, Palme & Gail (2009)	0.7390	0.2469	0.0141	0.0191
Asplund, Grevesse & Sauval (2009)	0.7381	0.2485	0.0134	0.0181

Note. For this table, the He abundances given in Anders & Grevesse (1989) and Grevesse & Noels (1993) have been replaced by the current best estimate from helioseismology (cf. Section 3.9 in Asplund et al., 2009). This table is reproduced from Asplund et al. (2009).

3.5 Effects of the assumed solar abundance ratio

We assumed the solar abundance ratios of Anders & Grevesse (1989), except the iron abundance, $\log \epsilon(\mathrm{Fe}) = 7.50$ that are taken from Genovali et al. (2014). Recent investigations have derived significantly different abundance ratios (e.g. Asplund et al., 2009). The new ratios for example have smaller CNO compositions. Table 3.5 shows mass fractions in literatures including Asplund et al. (2009). The Z/X of Asplund et al. (2009) is two thirds that of Anders & Grevesse (1989), $\Delta \log(Z/X) = -0.18$. In order to estimate the effect of this difference, we made the measurements of [Fe/H] of calibrating stars again with the atmosphere models with metallicity offset by -0.18 dex. The other parameters including ξ are fixed as used in the analysis described in the previous section. Then, the new estimates, Z_2, are compared with the original value, Z_1 (Figure 3.10, Table 3.6). Although the two estimates are consistent in most cases, some Z_2 are smaller than Z_1. We further checked behavior of the residuals, $Z_2 - Z_1$, as functions of stellar parameters ($T_{\rm eff}$, $\log g$, $[\mathrm{Fe/H}]_{\rm REF}$ and ξ). As seen in Figure 3.11, the residuals are within 0.1 dex with the average of -0.04 dex. The left top panel shows that Z_2 become smaller toward to low temperature. If a star has an over-solar metallicity, the derived metallicity might be slightly lower with the solar abundances of Asplund et al. (2009) adopted. The analysis here suggests that when we compare metallicities derived by our method with other results based on Asplund et al. (2009), there may be a small offset in the metallicity scale. On the other hand, previous works on measurements of Cepheids' chemical abundances assumed the older solar abundance, i.e. Anders & Grevesse (1989) or similar ratios. We can directly compare our measurements with previous ones as we do in Chapter 6 and 8.

Table 3.6. Effects of the different solar abundances (details in the text).

Object	$[Fe/H]_{REF}$ (dex)	Z_1 (dex)	$[Fe/H]_{REF-0.18}$ (dex)	Z_2 (dex)	$Z_2 - Z_1$ (dex)
HD 219978	0.22	7.52±0.03	0.04	7.43±0.03	−0.09
HD 137704	−0.32	7.30±0.02	−0.50	7.23±0.03	−0.07
Arcturus	−0.53	7.05±0.02	−0.71	7.02±0.02	−0.03
HD 12014	0.04	7.45±0.03	−0.14	7.41±0.03	−0.04
HD 124186	0.30	7.82±0.03	0.12	7.75±0.03	−0.07
μ Leo	0.31	7.78±0.03	0.13	7.70±0.03	−0.08
HD 223047	0.04	7.73±0.02	−0.14	7.74±0.02	0.01
HD 196755	−0.02	7.64±0.01	−0.20	7.63±0.01	−0.01
HD 204155	−0.69	7.02±0.02	−0.87	7.03±0.01	0.01
HD 18391	−0.13	7.54±0.04	−0.31	7.54±0.04	0.00

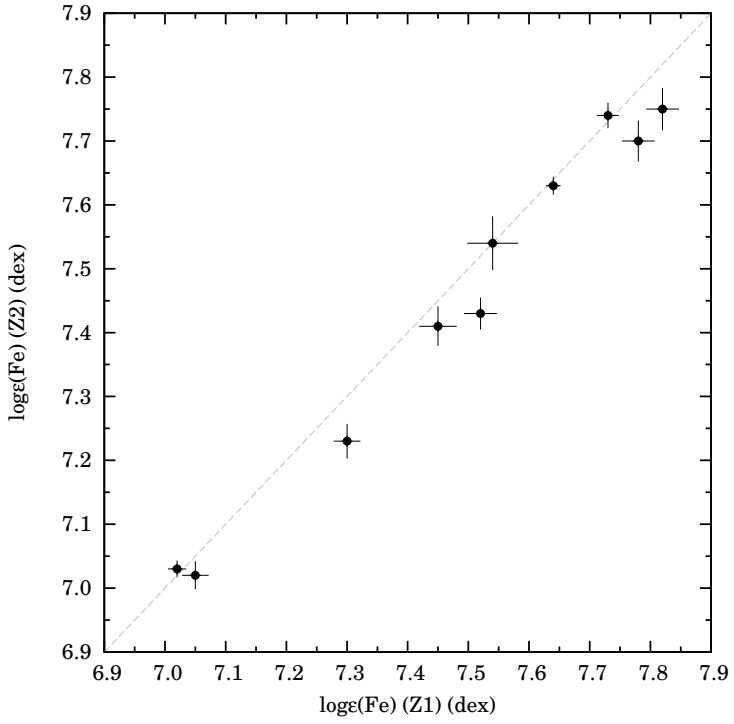

Figure 3.10 Comparison between derived abundances of Z_1 and Z_2.

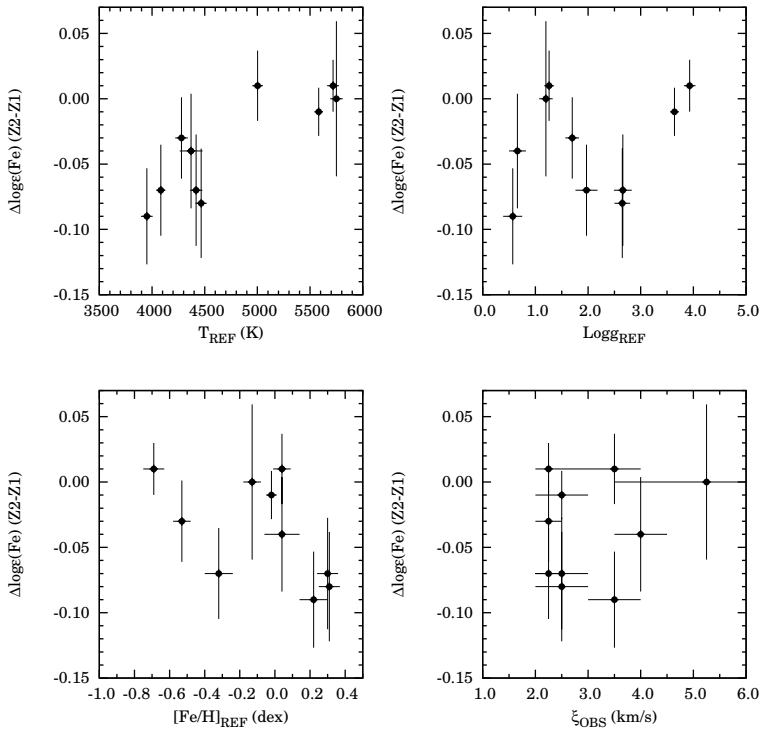

Figure 3.11 Behavior of residual $(Z_1 - Z_2)$ as functions of other parameters ($T_{\rm eff}$, $\log g$, ξ).

3.6 Summary

In this section, we described our method of measuring the iron abundance and made the analysis on *Subaru*/IRCS H-band spectra of 10 metal standard stars. An important step is to determine the microturbulence, and we use the ξ–$\log \epsilon$(Fe) plot but considering only selected groups of strong and weak lines. The iron abundances we derived are more-or-less within the scatters of previous estimates, although there can be a slight offset toward higher iron abundances compared with other metallicity scales. Such a potential difference in the metallicity scale is important when our metallicities are compared with literature values. Because our main targets are Cepheids, comparisons with other measurements done for Cepheids are essential. In Chapter 6, we first investigate iron abundances of calibrating Cepheids to compare our metallicity scale with ones in other works.

Chapter 4

Line-depth ratios in H band to determine $T_{\rm eff}$

In the previous chapter, we discussed determination of microturbulence and iron abundance for stars with atmospheric parameters well known. However, in case of Cepheids whose temperatures change due to pulsation, it is necessary to determine the temperatures based on spectra. Furthermore, photometric colors cannot be used for estimating the temperatures of the target Cepheids in the Galactic Center because of the large foreground reddening and its uncertainty. Here we extend the line-depth ratio (LDR) method, which has been applied to optical spectra of Cepheids and other types of stars, to use with H-band spectra. We develop the temperature scales using spectra of the static calibrating stars in this chapter, and apply these scales to Cepheids in the following chapter. We first ignore secondary effects of other parameters such as metallicity, and then take those effects into account. A large fraction of this chapter, except section 4.3.1, has been published in Fukue et al. (2015).

4.1 Introduction to the LDR method

Atmospheric structures of stars and their spectra are mainly characterized by three parameters: effective temperature, surface gravity and metallicity. Among these, the most influential is the effective temperature ($T_{\rm eff}$). Given appropriate photometric data, the color indices provide a simple and reliable method for measuring the temperature (e.g., Alonso et al., 1996). Alternatively, by using spectroscopic data $T_{\rm eff}$ can be determined by the absence of any correlation between iron abundance and lower-level excitation potential of many iron lines (e.g., Santos et al., 2000; Niemczura et al., 2014). We can also determine the temperature by globally comparing the observed and synthesized spectra (e.g., Prugniel et al., 2011).

The above methods have been established and used for optical spectra. However, objects with strong interstellar extinction, such as those occupying the inner part of the Milky Way, cannot be observed in the optical. Although recent developments in infrared instruments have enabled photometric and spectroscopic observations of these objects, their temperatures are difficult to derive from broad-band colors because the photometric data are largely affected by reddening and extinction. Moreover, as for our target Cepheids, Matsunaga et al. (2011, 2013) assumed their intrinsic colors

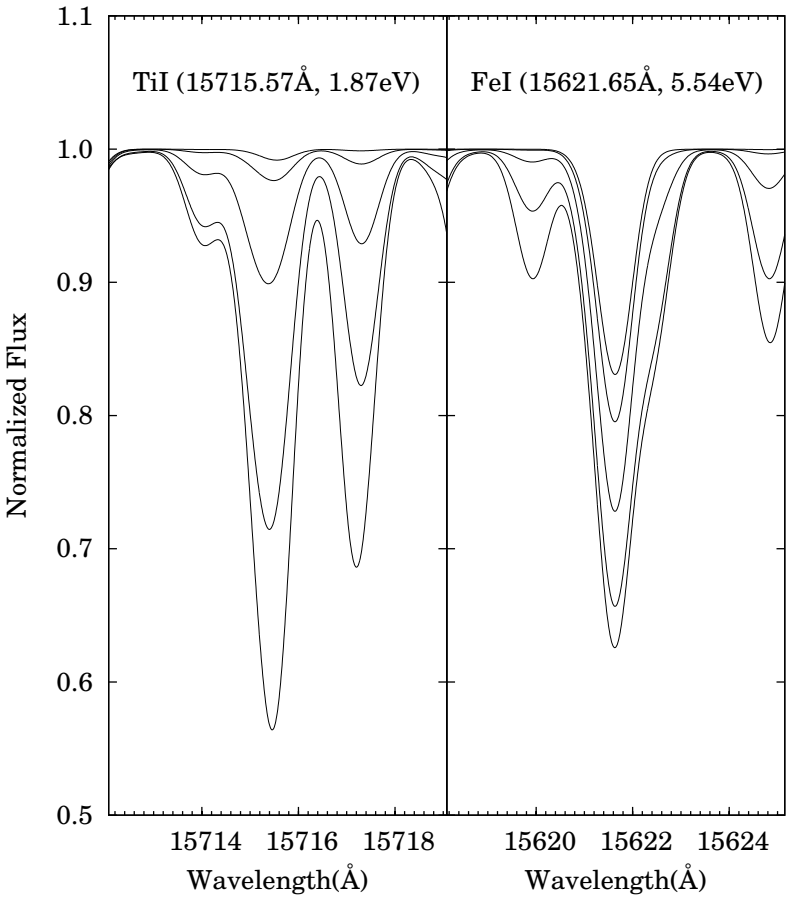

Figure 4.1 Different sensitivity to temperature of absorption lines low-excitation (left) and high-excitation (right) potentials illustrated by using synthesized spectra with fixed stellar parameters except temperature which is varied from 4000 K to 6000 K with an interval of 500 K.

based on period-color relation in order to estimate foreground reddenings (and distances). It is difficult to obtain the foreground reddenings accurately based on neighboring stars because the reddening towards the Galactic Center is very complex with small angular scales down to several arc-seconds. Therefore, temperatures of our targets must be determined from the spectroscopic data. To estimate the temperatures based on the excitation balance among absorption lines or by comparison with synthesized spectra, we require (at least, internal) estimates of chemical abundances. The derivation of the abundances is greatly affected by uncertainties in physical quantities such as oscillator strength ($\log gf$) and by non-LTE effects.

The LDR method compares depths of absorption lines with different excitation potentials (Figure 4.1). The temperature sensitivity of each line depends on the excitation potential (EP) of its lower energy level (Sheminova, 1993). For stars with $T_{\rm eff}$ = 4000 to 6000 K, neutral metal lines with low EP tend to grow rapidly with decreasing temperature. The temperature responses of higher potential lines (EP $\sim$ 5–6 eV) are weaker. At even higher potentials, lines with EP $\sim$ 7 eV strengthen with increasing temperature (see Figure 1 of Sheminova, 1993). Accordingly, the LDRs between lines with different responses are good indicators of the effective temperature. A large number of line pairs would reduce

statistical uncertainties. When high-dispersion spectra with many isolated lines are obtained, we can efficiently determine the temperatures from the depth ratios. Importantly, the empirical indicator can be constructed based on simple observables. The relations between LDR and $T_{\rm eff}$ established from spectroscopic data are unaffected by uncertainties in the line information, such as the $\log gf$ value, which introduce errors in the $T_{\rm eff}$ calculated by many other methods. Although the line strength depends on abundance, we can cancel this effect, to some extent by considering line ratios of the same element or those of elements with similar enrichment history for which the abundance ratios do not greatly change.

Gray & Johanson (1991) investigated the relationship between temperature and the ratio of V I and Fe I lines in approximately 50 dwarfs. They reported that the vanadium line weakens more strongly with increasing temperature. Sasselov & Lester (1990) found that the pair of C I and Si I lines provides a good thermal indicator in Cepheids. In this case, the carbon line with high EP strengthens with increasing temperature. Kovtyukh & Gorlova (2000) derived and combined temperature relations of 32 LDRs, reducing statistical errors down to 10–15 K in Cepheids and F- to G-type supergiants. Later Kovtyukh et al. (2006) and Kovtyukh (2007) derived 100 temperature relations from data for 200 giants, and 130 relations from 160 supergiants, respectively. A combination of such a large number of LDRs significantly improves the accuracy of the determined temperature (to within 5 K in the best cases).

The LDR method has been almost exclusively applied to optical spectra; reports of infrared applications are almost absent. Here, we search and calibrate the LDR temperature relations from high-dispersion near-infrared spectra in the H band, which covers wavelengths between 14000 and 18000 Å and contains numerous atomic lines and molecular bands. The extinction in the H band is ~ 9 times smaller than in the V band, i.e., $A_V/A_H \sim 9$ (Nishiyama et al., 2008). Thus, we can derive the stellar atmospheric parameters of highly-obscured stars from infrared data.

4.2 Temperature scales in the H band

In order to establish the LDR method for H-band spectra, we investigate the *Subaru*/IRCS spectra of the ten static calibrating stars (Table 2.1). For our purpose, their temperatures need to be established well. Among these objects, the prototype K-giants Arcturus and μ Leo have been intensively investigated. For example, Smith et al. (2013, hereafter S13) derived the temperatures of both stars from the $J-K$ colors reported by Johnson et al. (1966). On the other hand, Prugniel et al. (2011, P11) averaged literature values of the temperatures. The temperature of Arcturus was reported to be 4280±60 K by P11 and as 4275±50 K by S13; that of μ Leo was 4466±54 K by P11 and 4550±50 K by S13. Their values agree within the error margins. Previous temperature estimates of these two stars are also found in Heiter et al. (2015). Unfortunately, accurate infrared magnitudes are not available for the other objects. Their 2MASS magnitudes, for example, have large errors (±0.2 mag) caused by saturation. Thus we cannot accurately calculate their temperatures from their photometric colors. As already mentioned in Chapter 2, P11 used global fitting to spectra for estimating the temperature of these objects. We use the temperatures found by P11, so that our temperature scale is based on theirs.

We selected pairs of metal lines for deriving the temperature scales as follows. We examined the

line list of Meléndez & Barbuy (1999), which includes basic line information such as EP and the $\log gf$ data calibrated by the solar spectrum. For the illustrative purpose, the $\log gf$ values of lines in the H band are plotted against the EP in Figure 4.2. A minority of the Fe I lines in the H band have low EP values (EP $<$ 4 eV) and are thus sensitive to temperature, whereas most other lines (EP = 5 to 7 eV) are less sensitive. First, we selected clearly visible spectral lines with low EP We also picked up clearly visible and unblended (as much as possible) lines with high EP We excluded carbon, nitrogen, and oxygen lines, because the abundances of these elements in giant and supergiant stars can be altered by dredge-up. We also excluded lines in spectral parts dominated by the strong molecular bands for cold objects ($T_{\rm eff} \sim 4500$ K) or by telluric lines (near both ends of the H band). After these rejections, 15 low-excitation and 30 high-excitation lines remained as candidates for our LDR indicators.

Combining the above candidate lines, we constructed LDRs using the central line depths, which are less sensitive to blending than equivalent widths (Kovtyukh et al., 1998). We measured the depths of low- and high-excitation lines (denoted d_1 and d_2 respectively) by Gaussian fitting using the splot task in IRAF. The depth d was measured from the continuum level, 0 (with no visible absorption) to the maximum depth, +1. We sampled 450 pairs between the candidate 15 low-excitation lines and 30 high-excitation lines and plotted their ratios $r = d_1/d_2$ against the stellar temperatures. The ratios involving nine of the low-excitation lines including Fe, Ti, Co, and K were strongly correlated with temperature. Finally, by minimizing the wavelength difference between the low- and high-excitation lines and ensuring that no lines were shared among multiple pairs, we selected the nine pairs listed in Table 4.1. The selected lines in our target spectra and their measured depths are presented in Figure 4.3 and Appendix C (Table C.1).

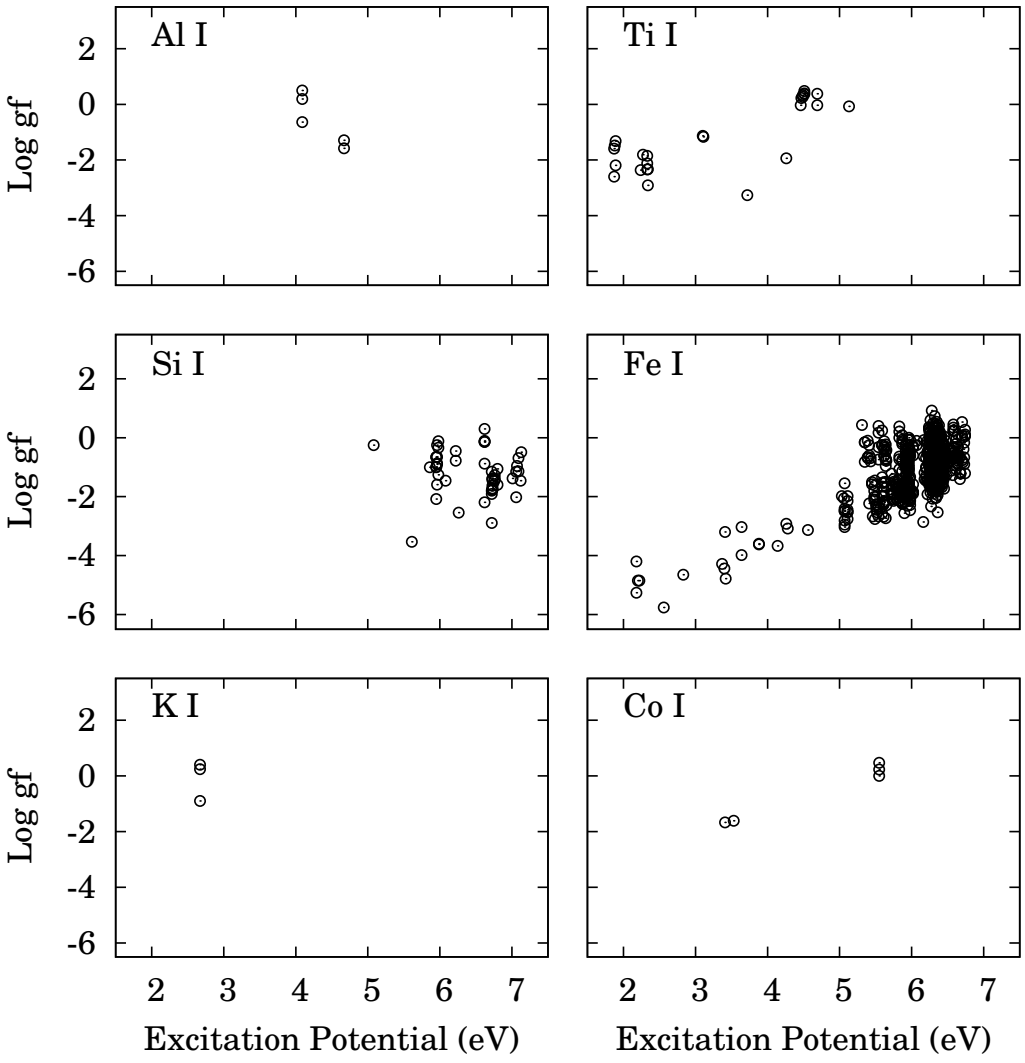

Figure 4.2 EP versus $\log gf$ for metal lines in the H band. For each of six elements, we plot all lines identified by Meléndez & Barbuy (1999) including unidentified lines in this work.

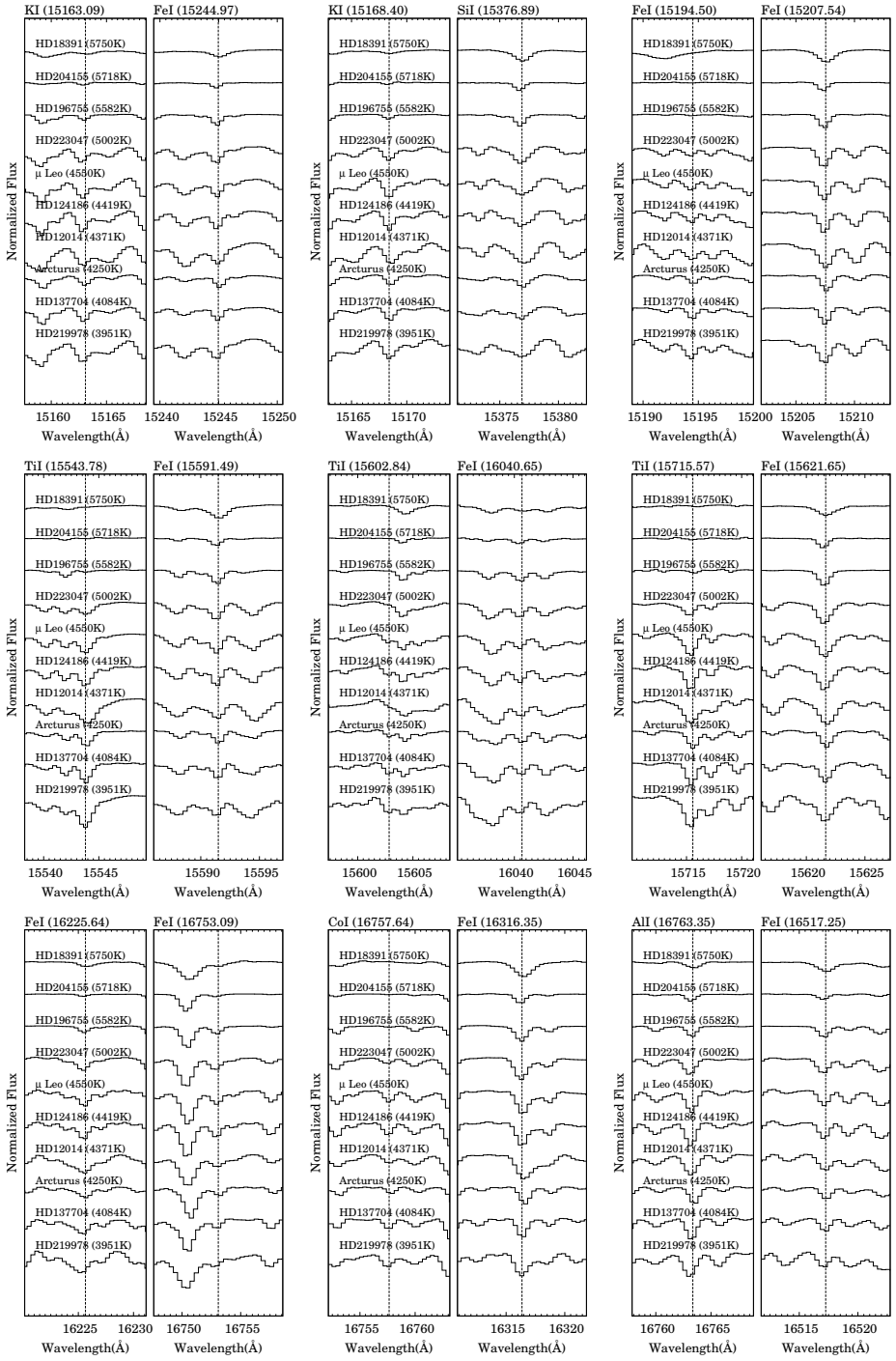

Figure 4.3 Small sections of all spectra around the measured lines for constructing temperature scales. For each pair, the left and right panels show variations of low- and high-excitation lines, respectively.

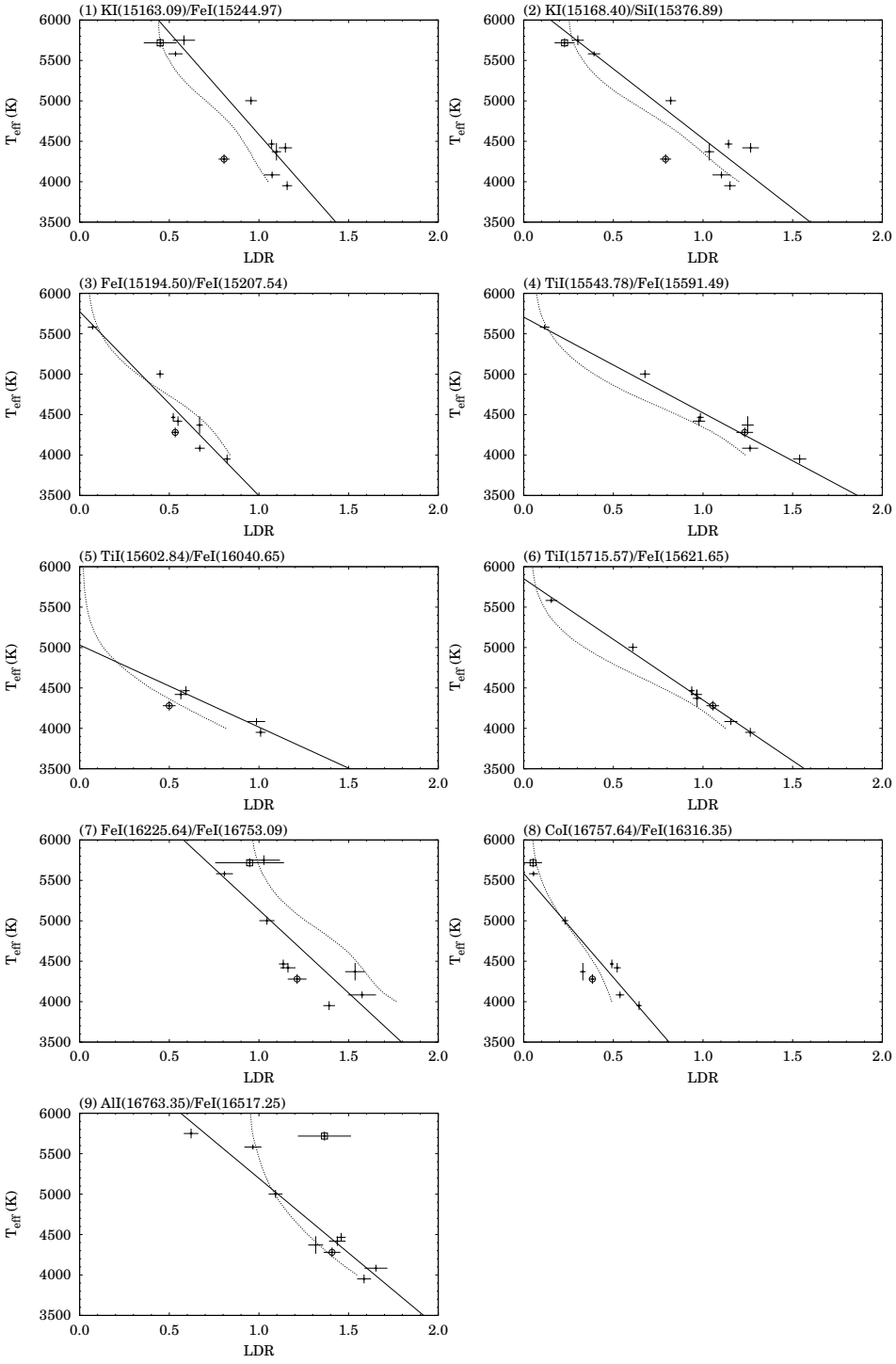

Figure 4.4 Temperature scales constructed by LDRs with H-band spectra. The solid lines indicate linear relations derived by least squares fitting. The open circle and square in each panel indicate Arcturus and HD 204155, respectively, which were not used for the fit. Dashed curves show LDRs constructed from model spectra ($T_{\rm eff}$ = 4000 to 6000 K, $\log g$ = 1.0 dex, [Fe/H] = 0.0 dex).

Table 4.1. Lines used in our indicators and calibrated relations of effective temperature.

	Low-excitation line					High-excitation line						
ID	λ (Å)	m[a]	El	EP (eV)	$\log gf$	λ (Å)	m[a]	El	EP (eV)	$\log gf$	Relation[b] $T_{\rm eff}$=	$\sigma_{\rm fit}$ (K)
(1)	15163.09	37	K I	2.67	0.40	15244.97	37	Fe I	5.59	−0.26	$7107 - 2524 \times r$	238
(2)	15168.40	37	K I	2.67	0.24	15376.89	37	Si I	6.22	−0.78	$6259 - 1726 \times r$	246
(3)	15194.50	37	Fe I	2.22	−4.85	15207.54	37	Fe I	5.39	−0.10	$5775 - 2278 \times r$	163
(4)	15543.78	37	Ti I	1.88	−1.48	15591.49	36	Fe I	6.24	0.36	$5706 - 1185 \times r$	121
(5)	15602.84	36	Ti I	2.27	−1.81	16040.65	35	Fe I	5.87	−0.07	$5031 - 1016 \times r$	67
(6)	15715.57	36	Ti I	1.87	−1.59	15621.65	36	Fe I	5.54	0.17	$5852 - 1502 \times r$	41
(7)	16225.64	35	Fe I	2.18	−5.26	16753.09	34	Fe I	6.38	0.07	$7190 - 2055 \times r$	414
(8)	16757.64	34	Co I	3.41	−1.67	16316.35	35	Fe I	6.28	0.92	$5586 - 2573 \times r$	209
(9)	16763.35	34	Al I	4.09	−0.64	16517.25	34	Fe I	6.29	0.37	$7042 - 1847 \times r$	197

[a]Echelle order in *Subaru*/IRCS H-band spectra.

[b]$r = d_1/d_2$

Thus-selected and derived the LDRs are plotted against temperature in Figure 4.4. The errors in the literature temperatures are taken from Prugniel et al. (2011). The errors in the ratios, σ_r, are computed from the line-depths (d_1 and d_2) and errors in the continuum (σ_1 and σ_2) derived from the residual spectra (as described in section 2.2.2):

$$\sigma_r = \frac{d_1}{d_2}\sqrt{\left(\frac{\sigma_1}{d_1}\right)^2 + \left(\frac{\sigma_2}{d_2}\right)^2}. \tag{4.1}$$

The relationships between r and $T_{\rm eff}$ were fitted to linear functions, as presented in Figure 4.4. Arcturus and HD 204155 were excluded from the calibration because of their lower metal contents than the other stars ([Fe/H] < -0.3 dex) and their offsets from the general trend. The linear relations and their 1 σ scatters ($\sigma_{\rm fit} = 40$–400 K) are listed in Table 4.1.

Table 4.2 lists the temperatures of each target estimated from our scales. The uncertainty of the temperature derived by each line pair (i) takes into account both the scatter around the relation, $\sigma_{\rm fit}$, and the measurement error, σ_r; $\sigma_i = \sqrt{\sigma_r^2 + \sigma_{\rm fit}^2}$. Then we can combine nine estimates, $T_i \pm \sigma_i$ ($i = 1 \cdots 9$), with the weights, $w_i = \frac{1}{{\sigma_i}^2}$, to obtain

$$T_{\rm LDR} = \frac{\sum_{i=1}^{N} w_i T_i}{\sum_{i=1}^{N} w_i}, \tag{4.2}$$

where T_i, σ_i and N indicate the temperature T, and its final error σ obtained with the i-th relation and N indicates the number of line pairs used. The standard error of the weighted mean, calculated by following formula with residuals $\delta_i = T_i - T_{\rm LDR}$,

$$\sigma_{\rm LDR} = \sqrt{\frac{\sum_{i=1}^{N} w_i \delta_i^2}{(N-1)\sum_{i=1}^{N} w_i}}. \tag{4.3}$$

The standard errors in the $T_{\rm LDR}$ tend to be large at the highest temperatures because the numbers of useful lines are limited. In stars with $T_{\rm eff} > 5500$ K, many low-excitation lines, in particular the Ti and Co lines, were too weak for an accurate temperature estimate.

We compared the temperatures of our targets derived by our LDR method ($T_{\rm LDR}$) with those reported in the literature ($T_{\rm REF}$). A plot of the residual ($T_{\rm LDR} - T_{\rm REF}$) versus $T_{\rm REF}$ (Figure 4.5; top panel) shows good agreement between the derived and reported temperatures. Such agreement is expected, as most of the objects appearing in Figure 4.5 were used in the calibration. The scatter in $T_{\rm LDR} - T_{\rm REF}$ indicates the uncertainty (~ 40 K) in the method. The bottom panel of Figure 4.5 plots the residual ($T_{\rm LDR} - T_{\rm REF}$) as a function of [Fe/H]$_{\rm REF}$. Note that derived temperatures of the two low-metal stars, Arcturus and HD 204155, disagree with the reference values. This inconsistency arises from the K lines and the Al line in the LDRs of Arcturus and HD 204155, respectively (Table 4.2). On the other hand, the derived temperature of μ Leo (a prototype metal-rich giant, [Fe/H]$= +0.3$ dex) is consistent with the reference. The temperature dependency on the stellar parameters and relevant uncertainty in our method will be discussed in section 4.3.1.

Table 4.2. Estimated temperatures and errors from the LDR method.

Object	T_i and σ_i from each relation									Mean
	(1)	(2)	(3)	(4)	(5)	(6)	(7)	(8)	(9)	
HD 219978	4186	4273	3902	3882	4006	3954	4331	3930	4112	3981
	±248	±252	±169	±129	±73	±59	±419	±212	±210	±29
HD 137704	4398	4355	4249	4210	4029	4117	3953	4204	3989	4123
	±263	±261	±175	±132	±83	±69	±443	±218	±229	±34
Arcturus	5074	4893	4560	4245	4523	4268	4697	4600	4442	4425
	±250	±252	±170	±133	±76	±67	±428	±215	±215	±68
HD 12014	4336	4472	4251	4225	···	4400	4033	4737	4610	4389
	±247	±250	±168	±127	···	±54	±429	±213	±211	±44
HD 124186	4211	4074	4526	4547	4457	4404	4802	4244	4388	4425
	±256	±259	±171	±128	±76	±61	±423	±215	±215	±34
μ Leo	4404	4287	4586	4539	4429	4444	4856	4321	4348	4447
	±243	±249	±165	±123	±70	±48	±417	±211	±203	±22
HD 223047	4695	4843	4754	4904	···	4937	5044	4993	5024	4917
	±252	±251	±169	±126	···	±56	±423	±214	±210	±26
HD 196755	5757	5582	5611	5567	···	5620	5530	5445	5257	5587
	±258	±253	±174	±125	···	±64	±425	±219	±216	±35
HD 204155	5974	5865	···	···	···	···	5242	5451	4520	5487
	±331	±264	···	···	···	···	±572	±245	±337	±246
HD 18391	5639	5738	···	···	···	···	5079	···	5894	5721
	±285	±253	···	···	···	···	±453	···	±211	±129

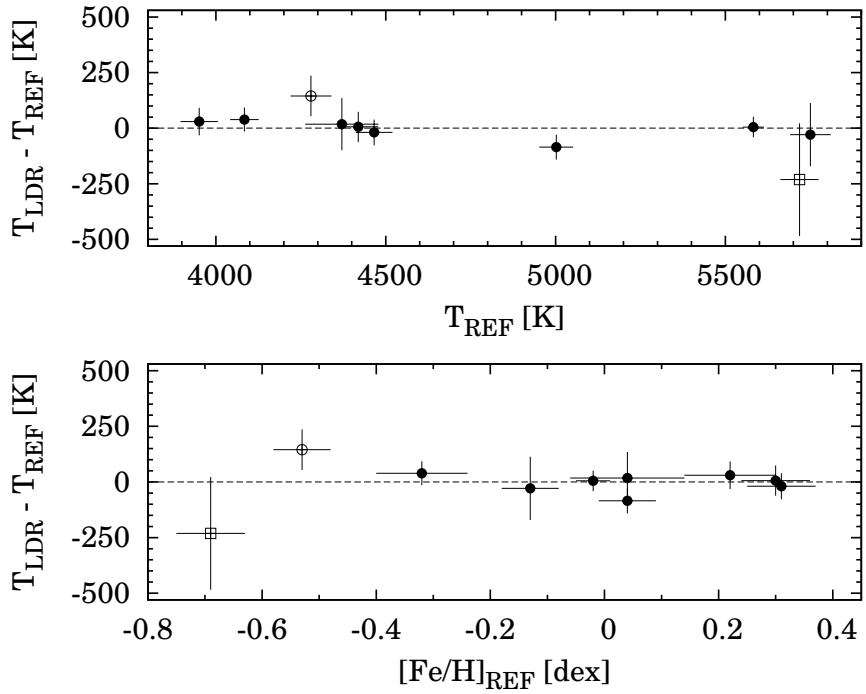

Figure 4.5 The residual ($T_{\rm LDR} - T_{\rm REF}$) as a function of $T_{\rm REF}$ (top) or iron abundance (bottom). The open circle and square in each panel indicate Arcturus and HD 204155, respectively.

4.3 Discussion

4.3.1 Sensitivity to atmospheric parameters

The stellar parameters of the eight giant/supergiant stars used in our calibration are expected to represent those of similar stars in the solar neighborhood; $\log g$ range from 0.5 to 4 dex and [Fe/H] vary within ± 0.3 dex. Here we investigate the dependency of our scales on other parameters such as metallicity. For example, if a line pair is contributed by different elements, the LDR can be influenced by the abundance ratio between those elements. The abundances relative to the iron, at least for most of the elements used in this study, show only small deviations (∼0.1 dex) from their solar values among stars with solar metallicity (Kovtyukh, 2007). In contrast, low-metal objects (especially those with [Fe/H] < -0.3 dex) tend to show non-solar abundance ratios; a typical example is Al (e.g., Bensby et al., 2005; Smith et al., 2013). Considering the low metallicities of Arcturus and HD 204155, their [K/Fe] or [Al/Fe] ratios are suggested to be different from the ratios of the other stars.

In the following, we consider the LDR in the form of $r(T, G, m, \xi, a)$ as a function of effective temperature (T), surface gravity ($G \equiv \log g$), the metallicity ($m \equiv$ [M/H]), the microturbulence (ξ) and the abundance ratio ($a \equiv$ [X/Fe]). Considering its dependency on each parameter to the first order around a given point of $(T_0, G_0, m_0, \xi_0, a_0)$, the Taylor expansion gives:

$$\begin{aligned} r - r_0 &= \left(\frac{\partial r}{\partial \tau}\right)(\tau - \tau_0) + \left(\frac{\partial r}{\partial G}\right)(G - G_0) + \left(\frac{\partial r}{\partial m}\right)(m - m_0) \\ &\quad + \left(\frac{\partial r}{\partial v}\right)(v - v_0) + \left(\frac{\partial r}{\partial a}\right)(a - a_0), \end{aligned} \tag{4.4}$$

where $\tau \equiv \log T$ and $v \equiv \log \xi$. Using this formula, we estimate the sensitivity of our LDR method to the parameters around the following grid points: $T_{\rm eff}$ = (4600, 5000, 5400), G = (1.0, 2.0, 3.0), m = (–0.3, +0.0, +0.3, +0.5), ξ = (2.0, 3.0, 4.0) and a = 0.0. Adjacent synthesized spectra with these parameters are compared and we obtained the partial derivative coefficients in the above formula (Tables 4.3–4.7). For this experiment, we generated model atmospheres and synthesize spectra using SPTOOL as described in section 3.1. We adopted the metal line list in Meléndez & Barbuy (1999), but for CoI(16757) we used the $\log gf$ value calibrated by Smith et al. (2013).

With an offset of a parameter given, we can calculate its effect on the temperature from the LDR method by using the partial derivatives, as follows,

$$\Delta\tau = \left(\frac{\partial r}{\partial \tau}\right)^{-1} \left(-\left(\frac{\partial r}{\partial x}\right)\Delta x\right), \tag{4.5}$$

where x is considered as one of the parameter m,G,v and a. Table 4.8 lists the effects of such changes caused by four parameter-offsets ΔG = +1.0 dex, Δm = +0.1 dex, $\Delta\xi$ = +0.5 km/s and Δa = +0.1 dex. This table indicates that the sensitivities to metallicity and [X/Fe] are higher than those to microturbulence and surface gravity. While the sensitivity to a is not negligible, previous studies indicate that the spread in a is relatively small, less than 0.1 dex, in the metal-rich regime (e.g., Kovtyukh & Gorlova, 2000; Ryde & Schultheis, 2015). Because the determination of the abundance ratios a is beyond the scope of this paper, we consider their effects on the LDR temperature as an uncertainty in temperature. While we consider only one parameter (a) to represent the effects of abundance ratios here, it is required to estimate all the five abundance of Al, K, Co, Ti and Si in order to fully consider their effects. Such a detailed analysis is not possible with our nine LDRs.

Table 4.3. Partial derivatives of $\partial r/\partial\tau$.

m		$\partial r/\partial\tau$										
(dex)		4600	5000	5400		4600	5000	5400		4600	5000	5400
−0.3	(1)	−7.30	−5.99	−4.57	(4)	−9.13	−6.90	−4.48	(7)	−8.32	−6.96	−5.48
0.0		−6.65	−6.43	−6.20		−10.57	−8.55	−6.37		−6.54	−5.83	−5.06
0.3		−5.05	−6.05	−7.12		−11.02	−9.66	−8.17		−5.00	−4.80	−4.59
0.5		−3.58	−5.22	−6.99		−10.63	−9.88	−9.07		−4.32	−4.29	−4.25
−0.3	(2)	−8.72	−7.00	−5.13	(5)	−3.75	−2.63	−1.42	(8)	−3.77	−3.06	−2.28
0.0		−8.11	−7.41	−6.65		−4.77	−3.48	−2.09		−4.89	−4.12	−3.29
0.3		−6.67	−7.04	−7.45		−5.96	−4.51	−2.94		−4.63	−4.42	−4.20
0.5		−5.36	−6.30	−7.32		−6.71	−5.21	−3.59		−4.39	−4.49	−4.59
−0.3	(3)	−6.95	−5.22	−3.34	(6)	−8.20	−6.19	−4.01	(9)	−3.18	−2.54	−1.84
0.0		−7.83	−6.40	−4.84		−9.49	−7.78	−5.93		−3.28	−2.69	−2.04
0.3		−7.82	−7.06	−6.24		−9.79	−8.80	−7.73		−3.47	−2.84	−2.15
0.5		−7.23	−7.08	−6.92		−9.17	−8.89	−8.60		−3.56	−2.94	−2.27

Note. Partial derivatives of $\partial r/\partial\tau$ estimated by using models with various parameters but with $\log g = 1.0$, $\xi = 3.0$ km/s, $a = 0.0$ dex.

Table 4.4. Same as Table 4.3, but for $\partial r/\partial G$.

G		$\partial r/\partial G$										
(dex)		4600	5000	5400		4600	5000	5400		4600	5000	5400
1	(1)	−0.051	0.010	0.033	(4)	0.026	0.021	0.019	(7)	−0.092	−0.013	0.013
2		−0.045	0.000	0.027		0.028	0.017	0.016		−0.084	−0.022	0.008
3		−0.039	−0.009	0.021		0.030	0.014	0.014		−0.075	−0.030	0.003
1	(2)	0.000	0.031	0.035	(5)	−0.025	−0.002	0.004	(8)	−0.051	0.001	0.009
2		0.005	0.027	0.033		−0.015	−0.002	0.004		−0.058	−0.009	0.005
3		0.010	0.024	0.031		−0.005	−0.002	0.003		−0.065	−0.020	0.001
1	(3)	−0.034	0.008	0.011	(6)	−0.016	0.013	0.020	(9)	0.029	0.017	0.014
2		−0.056	−0.003	0.007		−0.016	0.005	0.016		0.055	0.028	0.017
3		−0.078	−0.014	0.004		−0.015	−0.002	0.012		0.082	0.038	0.019

Note. $\partial r/\partial G$ is estimated by using model with m=0.0 dex, ξ=3.0 km/s and a=0.0 dex fixed.

Table 4.5. Same as Table 4.3, but for $\partial r/\partial m$.

m		$\partial r/\partial m$									
(dex)		4600	5000	5400		4600	5000	5400		4600	5000	5400
−0.3	(1)	0.43	0.51	0.33	(4)	0.56	0.39	0.18	(7)	−0.16	0.06	0.10
0.0		0.45	0.61	0.44		0.64	0.50	0.25		−0.18	0.06	0.11
0.3		0.25	0.48	0.42		0.48	0.47	0.29		−0.13	0.04	0.09
0.5		0.18	0.44	0.46		0.44	0.51	0.36		−0.09	0.03	0.09
−0.3	(2)	0.40	0.47	0.30	(5)	0.24	0.12	0.04	(8)	0.38	0.24	0.13
0.0		0.41	0.56	0.41		0.33	0.17	0.07		0.37	0.31	0.18
0.3		0.25	0.45	0.40		0.32	0.18	0.08		0.25	0.29	0.20
0.5		0.19	0.43	0.45		0.35	0.21	0.11		0.27	0.31	0.24
−0.3	(3)	0.41	0.30	0.14	(6)	0.53	0.37	0.16	(9)	0.16	0.15	0.13
0.0		0.46	0.39	0.20		0.59	0.48	0.23		0.19	0.17	0.14
0.3		0.32	0.37	0.23		0.42	0.44	0.26		0.15	0.13	0.11
0.5		0.29	0.39	0.28		0.36	0.47	0.32		0.14	0.13	0.11

Table 4.6. Same as Table 4.3, but for $\partial r/\partial v$.

ξ		$\partial r/\partial v$									
(km/s)		4600	5000	5400		4600	5000	5400		4600	5000	5400
2	(1)	−0.56	−0.49	−0.30	(4)	−0.21	−0.28	−0.16	(7)	−0.09	−0.11	−0.04
3		−0.58	−0.49	−0.29		−0.22	−0.26	−0.15		−0.10	−0.08	−0.03
4		−0.60	−0.48	−0.28		−0.25	−0.24	−0.14		−0.11	−0.04	−0.02
2	(2)	−0.50	−0.41	−0.22	(5)	−0.25	−0.12	−0.04	(8)	0.02	−0.16	−0.12
3		−0.50	−0.41	−0.22		−0.24	−0.11	2.93		−0.12	−0.17	−0.12
4		−0.51	−0.41	−0.22		−0.23	−0.09	7.12		−0.31	−0.19	−0.11
2	(3)	−0.13	−0.23	−0.13	(6)	−0.46	−0.31	−0.14	(9)	−0.48	−0.33	−0.27
3		−0.17	−0.23	−0.13		−0.46	−0.30	−0.13		−0.44	−0.30	−0.24
4		−0.22	−0.23	−0.12		−0.46	−0.28	−0.12		−0.39	−0.26	−0.20

Note. $\partial r/\partial v$ is estimated by using model with m=0.0 dex, $\log g$=1.0 km/s and a=0.0 dex fixed.

Table 4.7. Same as Table 4.3, but for $\partial r/\partial a$.

	4600	5000	5400
(1)	1.38	1.62	1.06
(2)	0.84	1.00	0.53
(3)	0.01	0.02	0.01
(4)	1.18	1.16	0.43
(5)	0.85	0.38	0.13
(6)	1.26	0.98	0.38
(7)	0.98	0.78	0.31
(8)	0.28	0.39	0.25
(9)	1.18	1.06	1.08

Note. $\partial r/\partial a$ is estimated by using model with m=0.0 dex, $\log g$=1.0 km/s and ξ=3.0 km/s fixed and by an offset of a from 0.0 to 0.1 dex.

Table 4.8. Sensitivity of the LDR temperature to stellar parameters.

ID	$\Delta G = +1.0$	$\Delta m = +0.3$	$\Delta \xi = +1.0$	$\Delta a = +0.1$
(1)	18	337	−108	299
(2)	48	268	−79	158
(3)	14	217	−51	4
(4)	28	207	−44	159
(5)	−7	168	−44	128
(6)	19	216	−55	148
(7)	−25	33	−20	156
(8)	3	267	−60	111
(9)	75	217	−157	476
Average	19	214	−69	182

Note. The offsets are calculated based on equation 4.5, or 4.5 for the averaged temperature, for the case of stars with parameter around ($T_{\rm eff} = 5000, \log g = 1.0, \xi = 3.0, a = 0.0$).

The uncertainty of the LDR method due to errors in other stellar parameters can be estimated as follows. Around a given LSR solution, offsets of four parameters (dG, dm, dv, da) lead to the following offset in τ,

$$\frac{1}{N}\sum_{i=1}^{N} d\tau = \frac{1}{N}\sum_{i=1}^{N}\left[\left(\frac{\partial r}{\partial \tau}\right)^{-1}\left(-\left(\frac{\partial r}{\partial G}\right)dG - \left(\frac{\partial r}{\partial m}\right)dm - \left(\frac{\partial r}{\partial v}\right)dv - \left(\frac{\partial r}{\partial a}\right)da\right)\right], \qquad (4.6)$$

where we took an average of the offsets in τ from N line pairs. The uncertainty of temperature caused by other stellar parameters is then estimated to be

$$\delta_\tau^2 = \frac{1}{N}\sqrt{\sum_{i=1}^{N}(d\tau)^2} = \frac{1}{N}\sqrt{\sum_{i=1}^{N}\left[\left(\frac{\partial r}{\partial \tau}\right)^{-2}\left(\left(\frac{\partial r}{\partial G}\right)^2\delta_G^2 + \left(\frac{\partial r}{\partial m}\right)^2\delta_m^2 + \left(\frac{\partial r}{\partial v}\right)^2\delta_v^2 + \left(\frac{\partial r}{\partial a}\right)^2\delta_a^2\right)\right]}, \qquad (4.7)$$

assuming that errors in four parameters $(\delta_G, \delta_m, \delta_v, \delta_a)$ are mutually independent. For example, the total uncertainty of 46 K is caused by errors of $(\delta_G = \pm 0.5, \delta_m = \pm 0.1, \delta_\xi = \pm 0.5, \delta_a = \pm 0.05)$ in case of stars with parameters around $(T = 5000, G = 1.0, m = 0.0, \xi = 3.0, a = 0.0)$ as indicated in Table 4.9.

Table 4.9. Uncertainty of the LDR temperature due to errors of stellar parameters.

Error in parameter	Error in τ (K)
$\delta_G = \pm 0.5$ dex	6
$\delta_m = \pm 0.1$ dex	25
$\delta_\xi = \pm 0.5$ km/s	14
$\delta_a = \pm 0.05$ dex	36
Total, δ_τ	46

Note. Calculated by equation 4.7 for the case of stars with parameters around ($T_{\rm eff} = 5000, \log g = 1.0, \xi = 3.0, a = 0.0$). Values for temperature and microturbulence are converted into those in linear scale, T and ξ.

4.3.2 Line blending

We now discuss how blending contributes to the uncertainty in the LDR method. Blending, or the merging of many strong lines, is a common phenomenon in the spectra of cold stars and a possible source of large uncertainty. The temperature responses of a few regions in the model spectra are presented in Figure 4.6 for example. We compare the depth d_B of a line used in our scales with the depth d_A in an experimental spectrum with the particular line removed (d_A should be zero in the absence of contamination lines). For this experiment, we again use SPTOOL to synthesize model spectra. To estimate the effect of blending, we consider the ratio of the two depths of each line in the normal and simulated spectra ($r_{\rm bl} = d_A/d_B$) as a function of temperature. For example, supposing that d_B involves an Fe line and d_A does not, we can directly estimate the contribution of lines other than the Fe line. We calculated the $r_{\rm bl}$ values in synthesized models under the parameter settings ($T_{\rm eff}$, $\log g$, [Fe/H], ξ) = (4000–6000 K at 100 K intervals, 1.0 dex, 0.0 dex, 2.5 km/s), fixing the abundance ratio to the solar ratio. The results are illustrated in Figure 4.7. For some line pairs $r_{\rm bl}$ is almost zero in the entire range between 4000 and 6000 K, but for others $r_{\rm bl}$ gets significantly large, over 30 – 50 %, toward the lower temperature, $T_{\rm eff} < 5000$ K. For example, line pairs involving Ti and Co give reliable temperatures in the range $T_{\rm eff} = 4000$–6000 K, whereas Fe and Al are more appropriate at higher temperatures ($T_{\rm eff} = 5000$–6000 K). The K and FeI(16225) lines in cold stars ($T_{\rm eff} < 5000$ K) require special care, because the resulting LDR is vulnerable to blending of many absorptions. In the case of TiI(15715)/FeI(15621), on the other hand the scatter around the temperature relation is small despite blending effects in the Ti line.

The effects of line blending naturally depend on the spectral resolution. Figure 4.8 compares the spectra synthesized at two resolutions ($\lambda/\Delta\lambda = 20,000$ and 70,000). Most of the atomic lines are well-resolved at the higher resolution. Because more lines are expected to be available for measurement also with the higher resolution, the temperature could be determined to higher precision. In H-band spectra of Arcturus ($\lambda/\Delta\lambda = 100,000$; Hinkle et al., 1995) and Sun ($\lambda/\Delta\lambda = 300,000$; Wallace et al., 1996) at even higher resolution, we can identify more than 50 low-excitation lines (EP < 5 eV), from which we would be able to construct many relationships between LDR and $T_{\rm eff}$ in the future.

4.4 Summary

We have constructed the stellar temperature indicator involving nine line pairs in the H band. We demonstrated that the LDR method accurately estimates the temperatures of G- and K-type giants/supergiants. Our temperature relations are based on the *Subaru*/IRCS spectra of the eight calibration stars. The temperatures derived from the scales using the low-excitation lines of Fe, Ti, Co, Si, Al, and K are accurate to within ~ 40 K considering only statistical errors, while there are some sensitivity to stellar parameters such as metallicity and relevant abundance ratios.

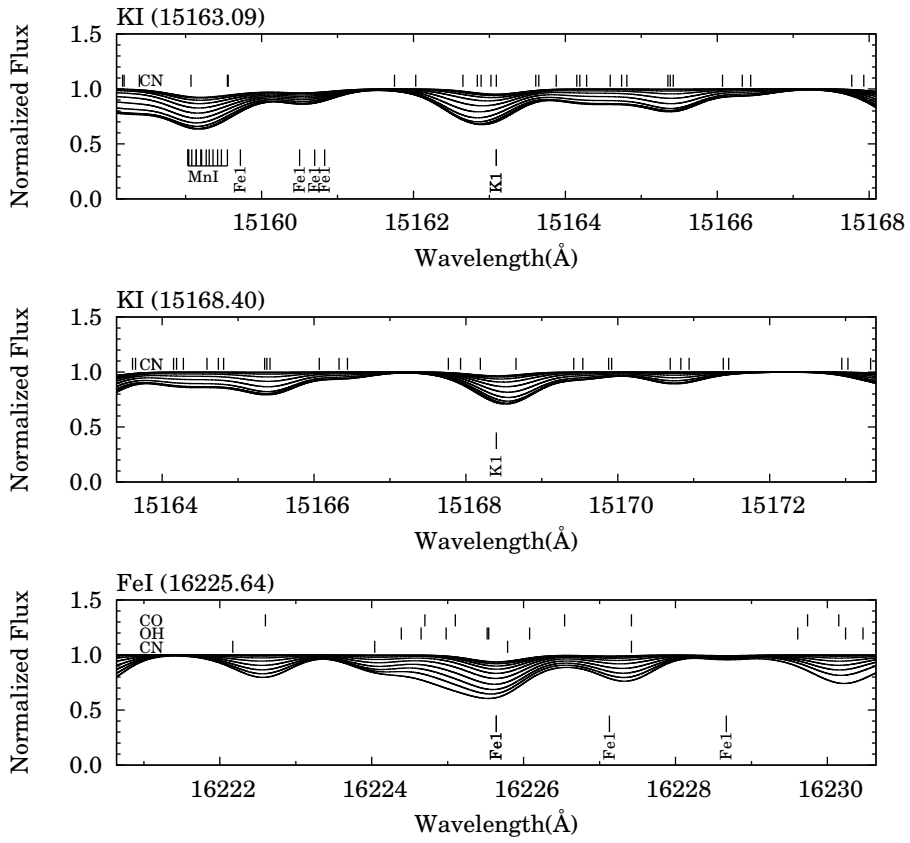

Figure 4.6 Variation of absorption lines changing with the temperature. Temperature range is 4000 (the lowest) to 6000 K (the upmost) at 200 K intervals. Other stellar parameters used are $\log g = 1.0$ dex, [Fe/H]= 0.0 dex, $\xi = 2.0$ km/s and $a = 0.0$ dex.

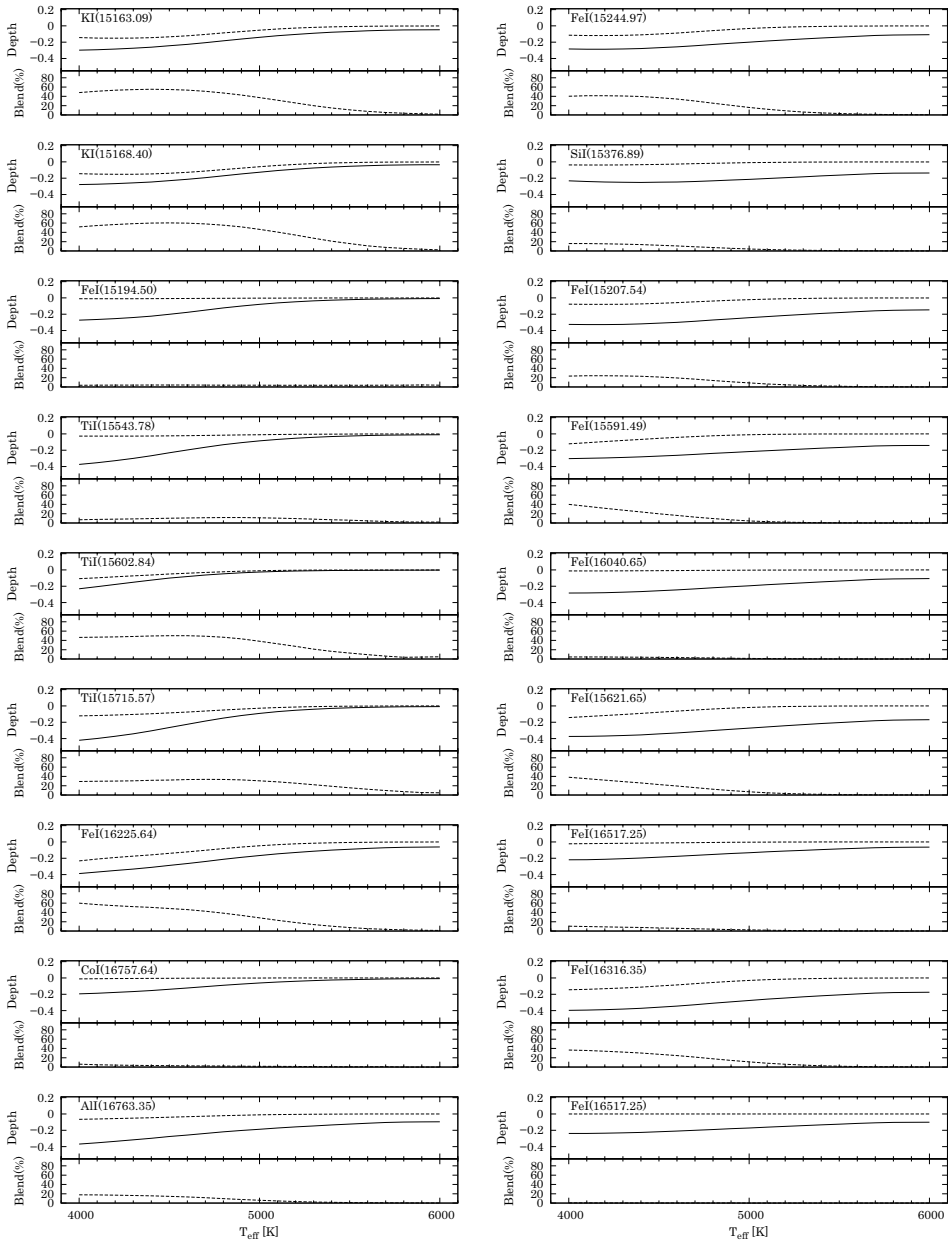

Figure 4.7 Variation of line-depth and blending for each absorption line as functions of the temperature. In the upper panel for each line, the solid and dashed curves indicate depths in normal spectra ($d_{\rm B}$) and those in experimental spectra without the target line considered ($d_{\rm A}$). The two curves are used to estimate blending ($r_{\rm bl}$) for each line which is shown in the lower panel.

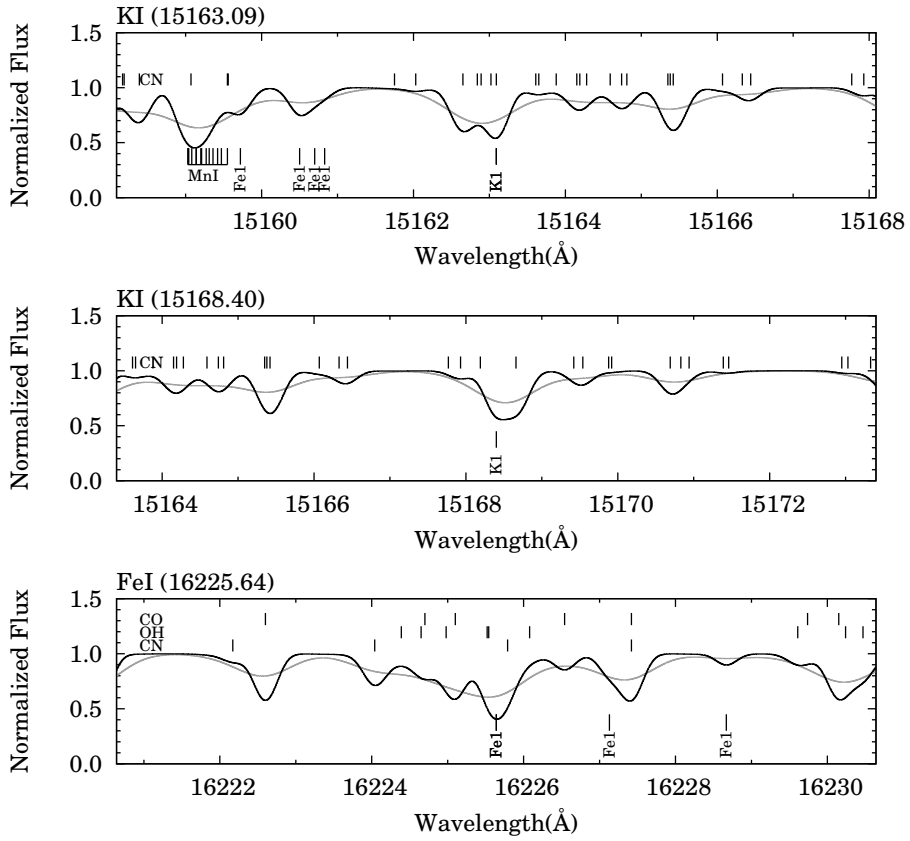

Figure 4.8 The effects of the line blending on absorption lines depending on spectral resolution or instrumental broadening. Gray and black curves indicate synthesized spectra with $\lambda/\Delta\lambda = 20{,}000$ and 70,000, respectively.

Chapter 5

Determination of stellar parameters using LDR

In section 4.3.1, we found that LDRs depend on not only $T_{\rm eff}$ but other parameters such as [Fe/H] and other abundance ratios. Here we consider a method of using such dependency to determine these stellar parameters. The experiment in which we used synthesized (i.e. ideal) spectra demonstrate the potential of the method We also discuss the determination accuracy of stellar parameters in case of observed spectra, and we found that this method tends to be severely affected by observational errors.

5.1 Method

Considering that the LDRs depend on stellar parameters including metallicity it is possible to consider a method of determining the parameters based on the LDRs only. Let us consider that a given parameter set $(T_0, G_0, m_0, \xi_0, a_0)$ predict an LDR r_0 for each line pair but this is different from the observed value r. As we discussed in section 4.3.1, the Taylor expansion of r gives

$$\begin{aligned} r - r_0 &= \left(\frac{\partial r}{\partial \tau}\right)(\tau - \tau_0) + \left(\frac{\partial r}{\partial G}\right)(G - G_0) + \left(\frac{\partial r}{\partial m}\right)(m - m_0) \\ &\quad + \left(\frac{\partial r}{\partial v}\right)(v - v_0) + \left(\frac{\partial r}{\partial a}\right)(a - a_0), \end{aligned} \tag{5.1}$$

Then, considering the sensitivities to the parameters discussed above, we can find a correction $(dT, dG, dm, d\xi, da)$ to remove the discrepancies in LDRs by minimizing the following χ^2,

$$\chi^2 = \sum_{i=1}^{9}\left[(r - r_0)_i - \left(\left(\frac{\partial r}{\partial \tau}\right)_i d\tau + \left(\frac{\partial r}{\partial G}\right)_i dG + \left(\frac{\partial r}{\partial m}\right)_i dm + \left(\frac{\partial r}{\partial v}\right)_i dv + \left(\frac{\partial r}{\partial a}\right)_i da\right)\right]^2, \tag{5.2}$$

we differentiate partially the χ^2, for example by $d\tau$ to find an optimized solution,

$$\begin{aligned} \frac{\partial \chi^2}{\partial (d\tau)} = -2\sum_{i=1}^{9}\left(\frac{\partial r}{\partial \tau}\right)_i \Bigg[(r - r_0)_i - \Bigg(\left(\frac{\partial r}{\partial \tau}\right)_i d\tau &+ \left(\frac{\partial r}{\partial G}\right)_i dG + \left(\frac{\partial r}{\partial m}\right)_i dm \\ &+ \left(\frac{\partial r}{\partial v}\right)_i dv + \left(\frac{\partial r}{\partial a}\right)_i da\Bigg)\Bigg] = 0, \end{aligned} \tag{5.3}$$

leading to an equation,

$$\left[\sum_{i=1}^{9}\left(\frac{\partial r}{\partial \tau}\right)_i^2\right]d\tau + \left[\sum_{i=1}^{9}\left(\frac{\partial r}{\partial \tau}\frac{\partial r}{\partial G}\right)_i\right]dG + \left[\sum_{i=1}^{9}\left(\frac{\partial r}{\partial \tau}\frac{\partial r}{\partial m}\right)_i\right]dm + \left[\sum_{i=1}^{9}\left(\frac{\partial r}{\partial \tau}\frac{\partial r}{\partial v}\right)_i\right]dv + \left[\sum_{i=1}^{9}\left(\frac{\partial r}{\partial \tau}\frac{\partial r}{\partial a}\right)_i\right]da = \sum_{i=1}^{9}\left(\frac{\partial r}{\partial \tau}\right)_i (r-r_0)_i. \quad (5.4)$$

Thus we can make a system of equations as follows:

$$A\begin{pmatrix} d\tau \\ dG \\ dm \\ dv \\ da \end{pmatrix} = \begin{pmatrix} \sum\left(\frac{\partial r}{\partial \tau}\right)_i (r-r_0)_i \\ \sum\left(\frac{\partial r}{\partial G}\right)_i (r-r_0)_i \\ \sum\left(\frac{\partial r}{\partial m}\right)_i (r-r_0)_i \\ \sum\left(\frac{\partial r}{\partial v}\right)_i (r-r_0)_i \\ \sum\left(\frac{\partial r}{\partial a}\right)_i (r-r_0)_i \end{pmatrix}, \quad (5.5)$$

where,

$$A = \begin{pmatrix} \sum\left(\frac{\partial r}{\partial \tau}\right)_i^2 & \sum\left(\frac{\partial r}{\partial \tau}\frac{\partial r}{\partial G}\right)_i & \sum\left(\frac{\partial r}{\partial \tau}\frac{\partial r}{\partial m}\right)_i & \sum\left(\frac{\partial r}{\partial \tau}\frac{\partial r}{\partial v}\right)_i & \sum\left(\frac{\partial r}{\partial \tau}\frac{\partial r}{\partial a}\right)_i \\ \sum\left(\frac{\partial r}{\partial G}\frac{\partial r}{\partial \tau}\right)_i & \sum\left(\frac{\partial r}{\partial G}\right)_i^2 & \sum\left(\frac{\partial r}{\partial G}\frac{\partial r}{\partial m}\right)_i & \sum\left(\frac{\partial r}{\partial G}\frac{\partial r}{\partial v}\right)_i & \sum\left(\frac{\partial r}{\partial G}\frac{\partial r}{\partial a}\right)_i \\ \sum\left(\frac{\partial r}{\partial m}\frac{\partial r}{\partial \tau}\right)_i & \sum\left(\frac{\partial r}{\partial m}\frac{\partial r}{\partial G}\right)_i & \sum\left(\frac{\partial r}{\partial m}\right)_i^2 & \sum\left(\frac{\partial r}{\partial m}\frac{\partial r}{\partial v}\right)_i & \sum\left(\frac{\partial r}{\partial m}\frac{\partial r}{\partial a}\right)_i \\ \sum\left(\frac{\partial r}{\partial v}\frac{\partial r}{\partial \tau}\right)_i & \sum\left(\frac{\partial r}{\partial v}\frac{\partial r}{\partial G}\right)_i & \sum\left(\frac{\partial r}{\partial v}\frac{\partial r}{\partial m}\right)_i & \sum\left(\frac{\partial r}{\partial v}\right)_i^2 & \sum\left(\frac{\partial r}{\partial v}\frac{\partial r}{\partial a}\right)_i \\ \sum\left(\frac{\partial r}{\partial a}\frac{\partial r}{\partial \tau}\right)_i & \sum\left(\frac{\partial r}{\partial a}\frac{\partial r}{\partial G}\right)_i & \sum\left(\frac{\partial r}{\partial a}\frac{\partial r}{\partial m}\right)_i & \sum\left(\frac{\partial r}{\partial a}\frac{\partial r}{\partial v}\right)_i & \sum\left(\frac{\partial r}{\partial a}\right)_i^2 \end{pmatrix}. \quad (5.6)$$

Here we consider that a change in abundance ratio, a, gives offsets in all the elements other than Fe by the same amount. With the derivative coefficients given in Tables 4.3–4.7, for example, we can obtain the correction terms $(d\tau, dG, dm, dv, da)$. Since we only consider linear terms, it is necessary to repeat such a step until the iteration converges.

As an example, we present an experiment of the iteration with the initial parameter set ($T = 4600, G = 1.0, m = 0.0, \xi = 3.0, a = 0.0$) toward r_i of model spectra synthesized with a different parameter set ($T = 5000, G = 1.0, m = 0.3, \xi = 3.0, a = 0.0$). The initial parameter set gives the following matrix,

$$\begin{pmatrix} 473.32 & 1.37 & -25.03 & 19.80 & -56.20 \\ 1.37 & 0.02 & -0.04 & 0.05 & -0.15 \\ -25.03 & -0.04 & 1.65 & -1.14 & 2.89 \\ 19.80 & 0.05 & -1.14 & 1.15 & -2.93 \\ -56.20 & -0.15 & 2.89 & -2.93 & 8.75 \end{pmatrix}\begin{pmatrix} d\tau \\ dG \\ dm \\ dv \\ da \end{pmatrix} = \begin{pmatrix} -10.72 \\ -0.03 \\ 0.52 \\ -0.41 \\ 1.27 \end{pmatrix}, \quad (5.7)$$

with which we can calculate the step $(d\tau, dG, dm, dv, da)$ corresponding to the first step in Figure 5.1. This figure illustrates that the iteration reaches well close to the goal after four steps.

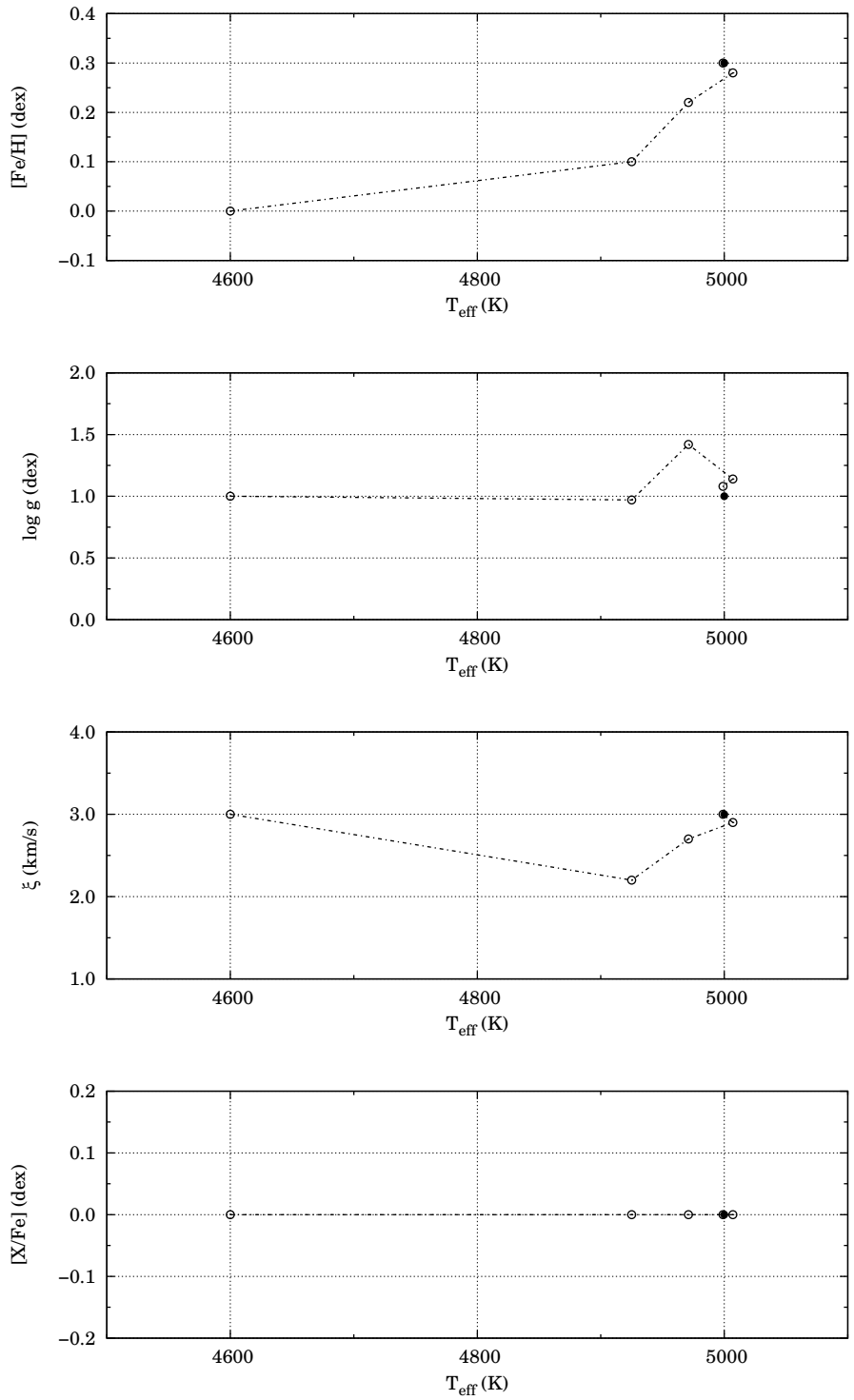

Figure 5.1 Iteration steps projected to various parameter planes. The filled circles indicate the true parameter set (T = 5000 K, G =1.0 dex, m =0.3 dex, ξ =3.0 km/s, a = 0.0 dex), while the iteration starts from (T = 4600 K, G = 1.0 dex, m = 0.0 dex, ξ = 3.0 km/s, a = 0.0 dex).

5.2 Effects of observational errors

The above equations also give expected errors after the iteration caused by observational errors in LDRs. The inversion of the above matrix,

$$A^{-1} = \begin{pmatrix} a_{11} & a_{12} & a_{13} & a_{14} & a_{15} \\ a_{21} & a_{22} & a_{23} & a_{24} & a_{25} \\ a_{31} & a_{32} & a_{33} & a_{34} & a_{35} \\ a_{41} & a_{42} & a_{43} & a_{44} & a_{45} \\ a_{51} & a_{52} & a_{53} & a_{54} & a_{55} \end{pmatrix}, \tag{5.8}$$

gives the following solution of the correction terms

$$\begin{pmatrix} d\tau \\ dG \\ dm \\ dv \\ da \end{pmatrix} = \begin{pmatrix} \sum \left[a_{11} \left(\frac{\partial r}{\partial \tau}\right)_i + a_{12} \left(\frac{\partial r}{\partial G}\right)_i + a_{13} \left(\frac{\partial r}{\partial m}\right)_i + a_{14} \left(\frac{\partial r}{\partial v}\right)_i + a_{15} \left(\frac{\partial r}{\partial a}\right)_i \right] dr_i \\ \sum \left[a_{21} \left(\frac{\partial r}{\partial \tau}\right)_i + a_{22} \left(\frac{\partial r}{\partial G}\right)_i + a_{23} \left(\frac{\partial r}{\partial m}\right)_i + a_{24} \left(\frac{\partial r}{\partial v}\right)_i + a_{25} \left(\frac{\partial r}{\partial a}\right)_i \right] dr_i \\ \sum \left[a_{31} \left(\frac{\partial r}{\partial \tau}\right)_i + a_{32} \left(\frac{\partial r}{\partial G}\right)_i + a_{33} \left(\frac{\partial r}{\partial m}\right)_i + a_{34} \left(\frac{\partial r}{\partial v}\right)_i + a_{35} \left(\frac{\partial r}{\partial a}\right)_i \right] dr_i \\ \sum \left[a_{41} \left(\frac{\partial r}{\partial \tau}\right)_i + a_{42} \left(\frac{\partial r}{\partial G}\right)_i + a_{43} \left(\frac{\partial r}{\partial m}\right)_i + a_{44} \left(\frac{\partial r}{\partial v}\right)_i + a_{45} \left(\frac{\partial r}{\partial a}\right)_i \right] dr_i \\ \sum \left[a_{51} \left(\frac{\partial r}{\partial \tau}\right)_i + a_{52} \left(\frac{\partial r}{\partial G}\right)_i + a_{53} \left(\frac{\partial r}{\partial m}\right)_i + a_{54} \left(\frac{\partial r}{\partial v}\right)_i + a_{55} \left(\frac{\partial r}{\partial a}\right)_i \right] dr_i \end{pmatrix}. \tag{5.9}$$

Thus, uncertainties of the parameters (σ_τ, σ_G, σ_m, σ_v, σ_a) are estimated by the following formulae

$$\begin{pmatrix} \sigma_\tau^2 \\ \sigma_G^2 \\ \sigma_m^2 \\ \sigma_v^2 \\ \sigma_a^2 \end{pmatrix} = \begin{pmatrix} \sum \left[a_{11} \left(\frac{\partial r}{\partial \tau}\right)_i + a_{12} \left(\frac{\partial r}{\partial G}\right)_i + a_{13} \left(\frac{\partial r}{\partial m}\right)_i + a_{14} \left(\frac{\partial r}{\partial v}\right)_i + a_{15} \left(\frac{\partial r}{\partial a}\right)_i \right]^2 \sigma_i^2 \\ \sum \left[a_{21} \left(\frac{\partial r}{\partial \tau}\right)_i + a_{22} \left(\frac{\partial r}{\partial G}\right)_i + a_{23} \left(\frac{\partial r}{\partial m}\right)_i + a_{24} \left(\frac{\partial r}{\partial v}\right)_i + a_{25} \left(\frac{\partial r}{\partial a}\right)_i \right]^2 \sigma_i^2 \\ \sum \left[a_{31} \left(\frac{\partial r}{\partial \tau}\right)_i + a_{32} \left(\frac{\partial r}{\partial G}\right)_i + a_{33} \left(\frac{\partial r}{\partial m}\right)_i + a_{34} \left(\frac{\partial r}{\partial v}\right)_i + a_{35} \left(\frac{\partial r}{\partial a}\right)_i \right]^2 \sigma_i^2 \\ \sum \left[a_{41} \left(\frac{\partial r}{\partial \tau}\right)_i + a_{42} \left(\frac{\partial r}{\partial G}\right)_i + a_{43} \left(\frac{\partial r}{\partial m}\right)_i + a_{44} \left(\frac{\partial r}{\partial v}\right)_i + a_{45} \left(\frac{\partial r}{\partial a}\right)_i \right]^2 \sigma_i^2 \\ \sum \left[a_{51} \left(\frac{\partial r}{\partial \tau}\right)_i + a_{52} \left(\frac{\partial r}{\partial G}\right)_i + a_{53} \left(\frac{\partial r}{\partial m}\right)_i + a_{54} \left(\frac{\partial r}{\partial v}\right)_i + a_{55} \left(\frac{\partial r}{\partial a}\right)_i \right]^2 \sigma_i^2 \end{pmatrix}. \tag{5.10}$$

using noises of r from individual line pairs, σ_i. For the parameter set ($T = 5000, \log g = 1.0, m = 0.3, \xi = 3.0, a = 0.0$), the inversion matrix is given by

$$A^{-1} = \begin{pmatrix} 0.04 & -2.17 & 0.72 & 0.42 & 0.11 \\ -2.17 & 1492.46 & -45.94 & 56.68 & 4.00 \\ 0.72 & -45.94 & 23.33 & 23.55 & 2.64 \\ 0.42 & 56.68 & 23.55 & 45.41 & 5.94 \\ 0.11 & 4.00 & 2.64 & 5.94 & 1.39 \end{pmatrix}. \tag{5.11}$$

Table 5.1 lists the corresponding errors in cases of four different S/N, 200, 100, 50 and 30. The errors in temperature and metallicity are of reasonable size in case of S/N=200, but they grow rapidly toward the lower S/N. Furthermore, note that we need to consider r values to get dr in order to use this method. We here use synthesized spectra which can be directly compared with each other, and thus the convergence was good as illustrated in Figure 5.1. When we compare synthesized spectra and observed ones, however, additional uncertainties such as errors in $\log gf$ are introduced. These errors are often as large as $\sigma_r = 0.1$ (e.g., see Figure 4.4), and this makes it hard to use the method described in this Chapter for observed spectra. For example, the uncertainties of metallicity in Table 5.1 are larger than the counterparts which we found in the method using MPFIT (described in Chapter 3). Such a difference is expected because we can reduce statistical errors by using up to 95 Fe I lines. Thus, we discuss iterative method to estimate the temperature and metallicity using both LDR and MPFIT in the next Chapter.

Table 5.1. Estimated errors in the five parameters in cases of four different S/N.

S/N	σ_τ (K)	σ_G (dex)	σ_m (dex)	σ_v (km/s)	σ_a (dex)
200	63	0.87	0.13	0.85	0.02
100	125	1.74	0.26	1.46	0.04
50	247	3.47	0.52	2.21	0.09
30	366	5.21	0.78	2.60	0.13

Note. The σ_τ and σ_v originally give the errors in logarithmic values, $\tau \equiv \log T$ and $v \equiv \log \xi$, but listed in this table are errors in T and ξ.

Chapter 6

Abundance analysis of Standard Cepheids

In this chapter, we are going to deal with iron abundances of the calibrating Cepheids, δ Cep and X Cyg (Table 2.1). We apply the LDR method (Chapter 4) to determine the temperatures at the epochs of our spectroscopic observations, and the method described in Chapter 3 to determine the iron abundances. We adopted surface gravities of Cepheids from literature values. The analysis on the calibrating Cepheids is important for checking if our methods are applicable to Cepheids and for comparing our metallicity scale with those in the previous works.

6.1 Atmospheric parameters

We determined effective temperatures of the two Cepheids using the LDR method introduced in Chapter 4. Figure 6.1 shows the parts of the Cepheids' spectra around the absorption lines for the LDR method. We then calculated weighted averages of temperatures from line pairs detected as described in section 4.2. Table C.2 lists the derived temperatures and the errors; both δ Cep and X Cyg are warmer than 5000 K. The top panels of Figures 6.2 and 6.3 show phase variations of their temperatures (Andrievsky et al., 2005; Kovtyukh et al., 2005). Red points indicate the derived temperatures and phases at our observations which were calculated using epochs and periods in literature. We found that our temperatures are consistent with expected values from the previous works. In addition, the bottom panels of these figures show radial velocities plotted against phase (Storm et al., 2004). These plots show that temperature becomes high after the maximum of radial velocity.

For the gravity, we adopt an average for each Cepheid from Takeda et al. (2013), $\log g$=2.3 (δ Cep) and 1.4 (X Cyg). Takeda et al. (2013) determined the gravities and other atmospheric parameters considering excitation balance and ionization balance (Figure 6.4). The gravity of each Cepheid shows a periodic change with a typical peak-to-valley amplitude of 1.0 dex in $\log g$, so that we consider the error of $\log g$ as $\pm$0.5 dex. As we see below, such an error does not give a significant effect on the iron abundance estimate.

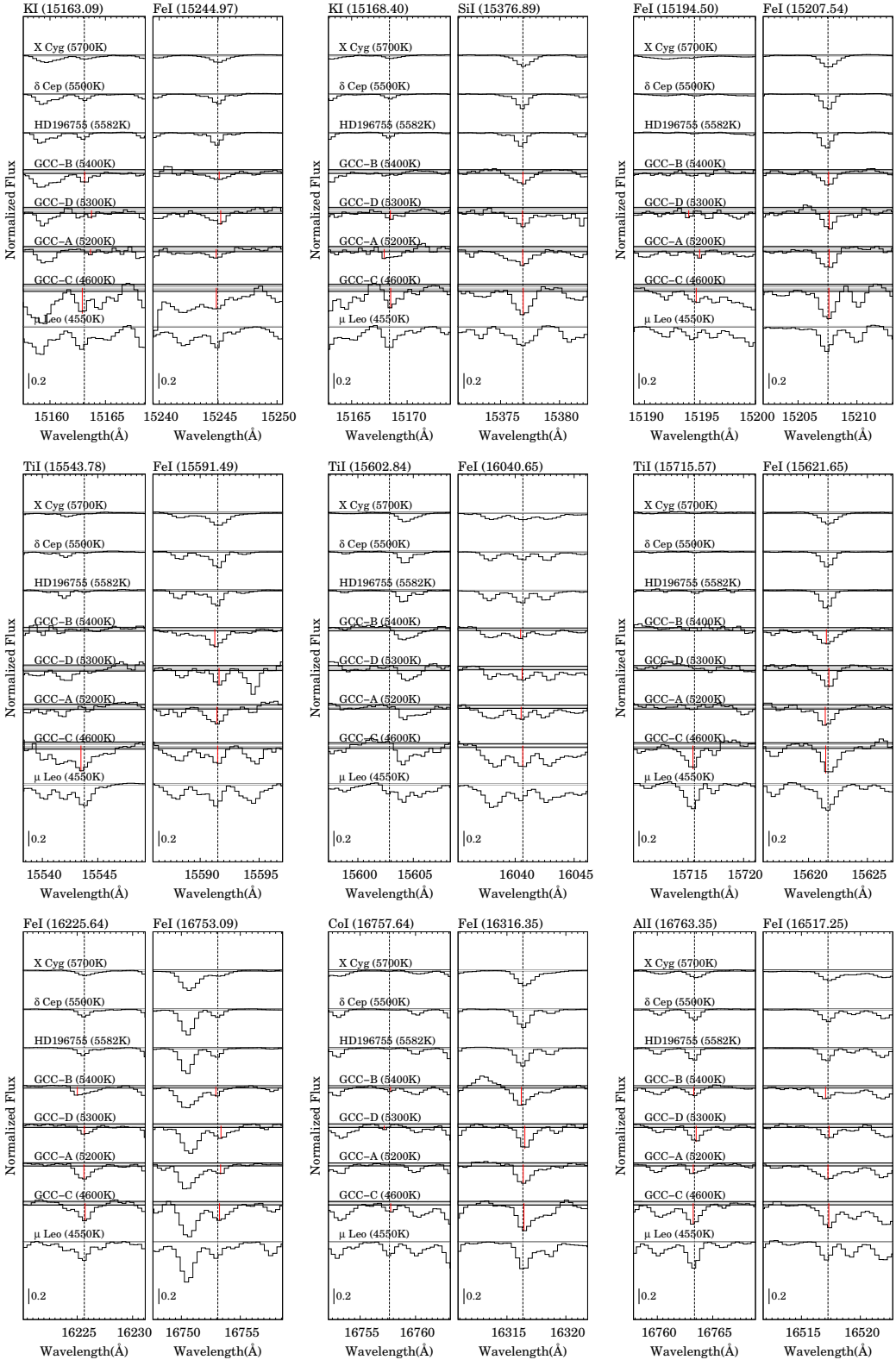

Figure 6.1 Spectra of Cepheids and two stars (μ Leo and HD196755) for comparison, around the absorption lines relevant to the LDR method.

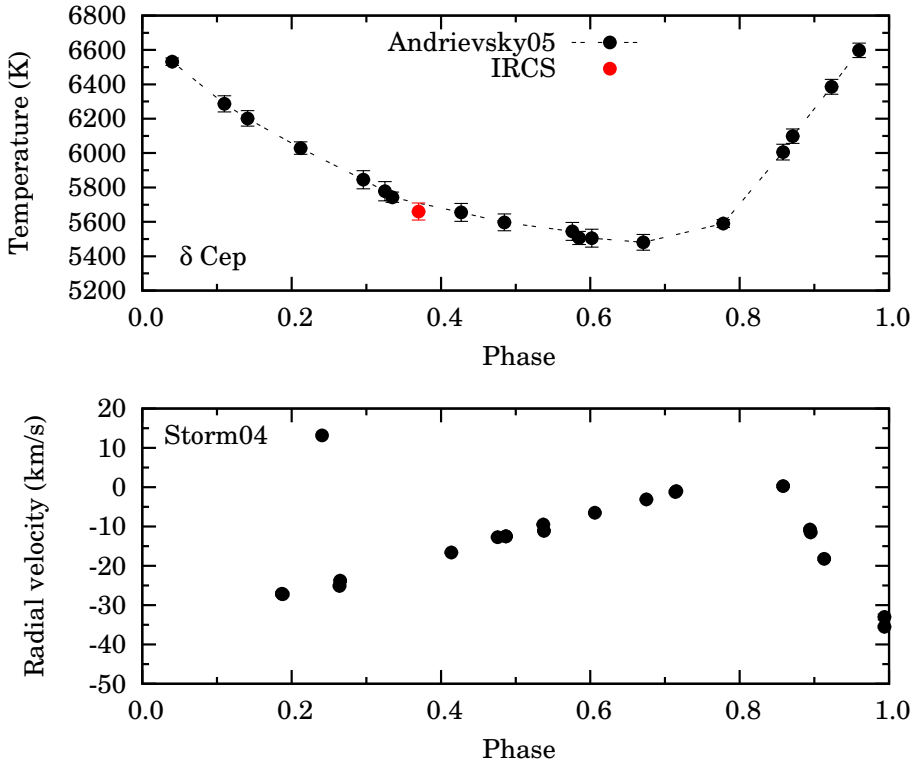

Figure 6.2 Variations of the temperature (top panel) and the radial velocity (bottom) during the pulsation cycle of δ Cep. The red points in the top panel indicates our result, while the others indicate literature data (top–Andrievsky et al., 2005; bottom–Storm et al., 2004). For calculating the observed phase, we adopted the epoch and period from Andrievsky et al. (2005).

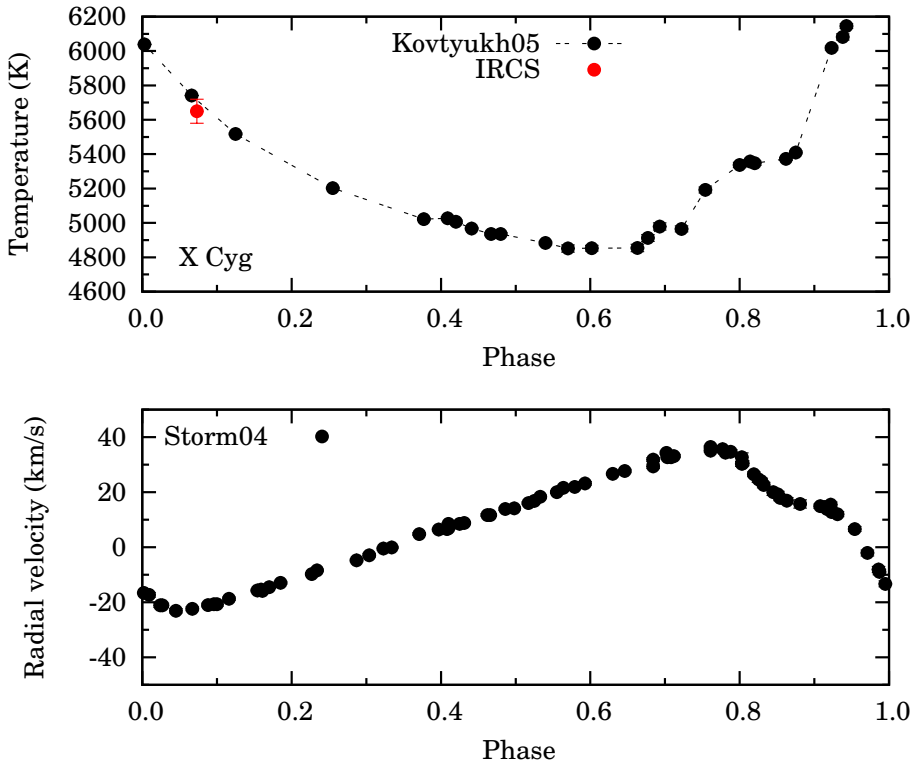

Figure 6.3 Similar to Figure 6.2 but for X Cyg. The black points in the top panel are adopted from Kovtyukh et al. (2005). For calculating the observed phase, we adopted the epoch and period from the same reference.

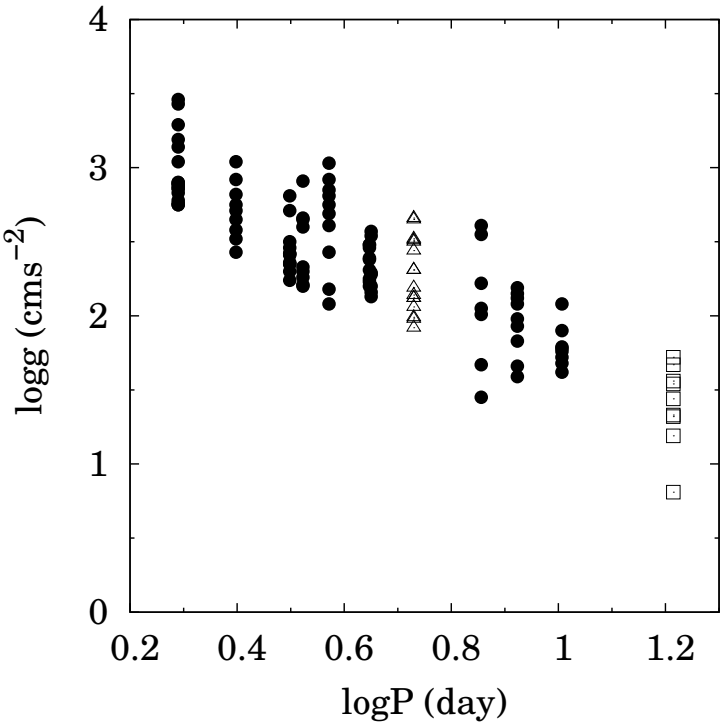

Figure 6.4 Surface gravities, derived from 122 spectra for 12 Cepheids, plotted against the pulsation period ($\log P$) from Takeda et al. (2013). The open triangles and squares indicate δ Cep and X Cyg, respectively. A range of gravity is observed for each Cepheid due to pulsation.

Table 6.1. Derived final parameters of calibrating Cepheids.

Object	$T_{\rm eff}$ (K)	$\log g$ (dex)	[M/H] (dex)	ξ (km/s)	[Fe/H] (dex)
δ Cep	5660±50	2.3±0.5	0.15	$3.0^{+0.5}_{-0.5}$	0.17±0.02
X Cyg	5650±70	1.4±0.5	0.05	$4.0^{+1.0}_{-0.5}$	0.06±0.02

Table 6.2. Effects of adopted stellar parameters on [Fe/H] estimates for calibrating Cepheids.

Object	$\sigma_{-\Delta T}$ (dex)	$\sigma_{+\Delta T}$ (dex)	$\sigma_{-\Delta G}$ (dex)	$\sigma_{+\Delta G}$ (dex)	$\sigma_{-\Delta \xi}$ (dex)	$\sigma_{+\Delta \xi}$ (dex)	σ_{all_-} (dex)	σ_{all_+} (dex)
δ Cep	–0.03	0.02	0.04	–0.03	0.04	–0.04	0.06	0.06
X Cyg	–0.04	0.07	0.05	–0.03	0.04	–0.05	0.07	0.10

6.2 Abundance analysis of standard Cepheids

Using the $T_{\rm eff}$ and $\log g$ given in the previous section, we constructed initial atmospheric models with the solar metallicity. Then we derived the microturbulence and the iron abundances following the method described in Chapter 3. If a derived iron-abundance is significantly different from the solar, there is an inconsistency between the iron abundance used for the atmospheric model and the result. In such cases we repeat the procedures iteratively until we find the two iron abundances agree within the error. Figures B.10 and B.11 in Appendix B show results of ξ and $\log \epsilon$(Fe) for δ Cep and X Cyg, respectively. Table 6.1 lists the derived ξ and $\log \epsilon$(Fe) values. Similarly to the case of the calibrating stars in Chapter 3, we estimated the errors of iron abundance caused by the uncertainty of parameters (Table 6.2). The errors are as small as those for the static calibration stars, $\leq$0.1 dex in total.

Figure 6.5 plots the comparison of our results with reference values (Table 6.3), which shows a good agreement within the error of $\sim$0.05 dex. Therefore, we conclude that our method is applicable to H-band spectra of Cepheid variable stars (at least to those with high S/N ratios, $\sim$100). Moreover, the iron abundances we derived are consistent with the scale in literature, supporting that it is reasonable to compare our results directly with the previous results in the context of the metallicity gradient.

Table 6.3. Iron abundances of δ Cep and X Cyg in the literature.

Object	[Fe/H] (dex)	Reference
δ Cep	0.09	Luck & Lambert(2011)
	0.12	Luck et al.(2011)
	0.04±0.05	Takeda et al.(2013)
X Cyg	0.10	Luck et al.(2011)
	0.09±0.07	Takeda et al.(2013)

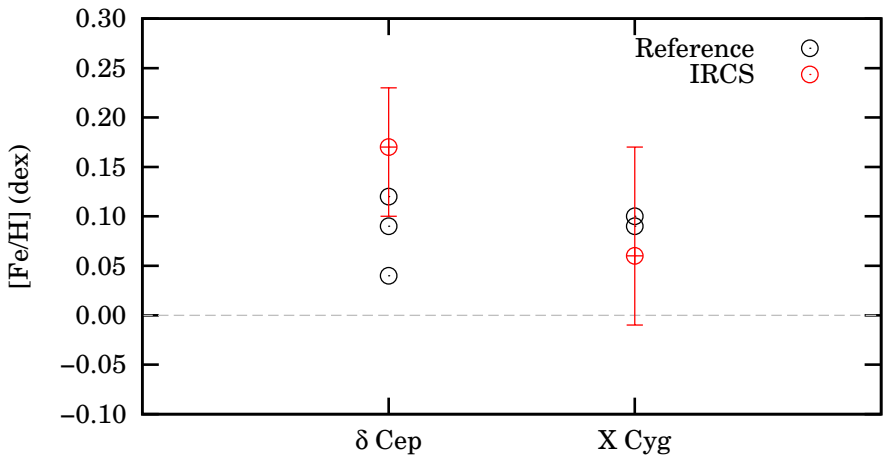

Figure 6.5 The iron abundances we derived for δ Cep and X Cyg (red circles) are compared with literature values (black, Table 6.3).

Chapter 7

Abundance analysis of GC Cepheids

In this chapter, we determine iron abundances of target Cepheids in the Nuclear Stellar Disk. We determine temperatures and iron abundances using same methods describe in Chapter 6. We adopted surface gravities of Cepheids from to be values expected for Cepheids with given periods.

7.1 The effects of low signal-to-noise ratios

As seen in Table 2.4, the spectra of the GC-Cepheids have significantly lower S/N, 30∼70, than those of the calibrating objects. Therefore, weakest lines are expected to become undetectable. In order to further examine the effect of the higher noise levels, we made a few simulations as follows. We synthesized a model spectra with $T_{\rm eff}$ = 5000, $\log g$ = 1.3, [Fe/H]= 0.0, and ξ = 3.0, and added random noises to produce simulated spectra corresponding to S/N = 200, 100, 50, and 30. We then measured iron abundances and compared the scatters of $\log \epsilon$(Fe) values for the four spectra. As presented in Figure 7.1, we found a significantly large scatter in case of the spectrum with S/N=30. The statistical error of $\log \epsilon$(Fe) gets larger, as expected, if the S/N is lower (Table 7.1).

We check the effects of noise on determination iron abundances considering all the available Fe I lines in the four simulated spectra (Figure 7.1 and Table 7.1). While the error of the iron abundance becomes larger in the lower S/N, the derived iron abundances, between 7.48±0.01 and 7.59±0.06 dex, are more-or-less within the errors.

Thirdly, we produced 100 spectra with S/N=30 as a Monte-Carlo simulation. Figure 7.3 shows examples of simulated spectra around some Fe I lines (left panels) and the results of repeated measurements of $\log \epsilon$(Fe) (right panels). This figure indicates that absorption lines and inferred [Fe/H] are largely affected. Along with the large width of the fitted Gaussians, a significant fraction of the simulated spectra give very high $\log \epsilon$(Fe) values for some lines (see, e.g. the bottom panel of Figure 7.2 and Figure 7.3). Such a trend can be understood by considering the curve-of-growth. In addition, MPFIT tends to fail to obtain $\log \epsilon$(Fe) values for weak lines in low-S/N spectra, as clearly seen in the top panel of Figure 7.3.

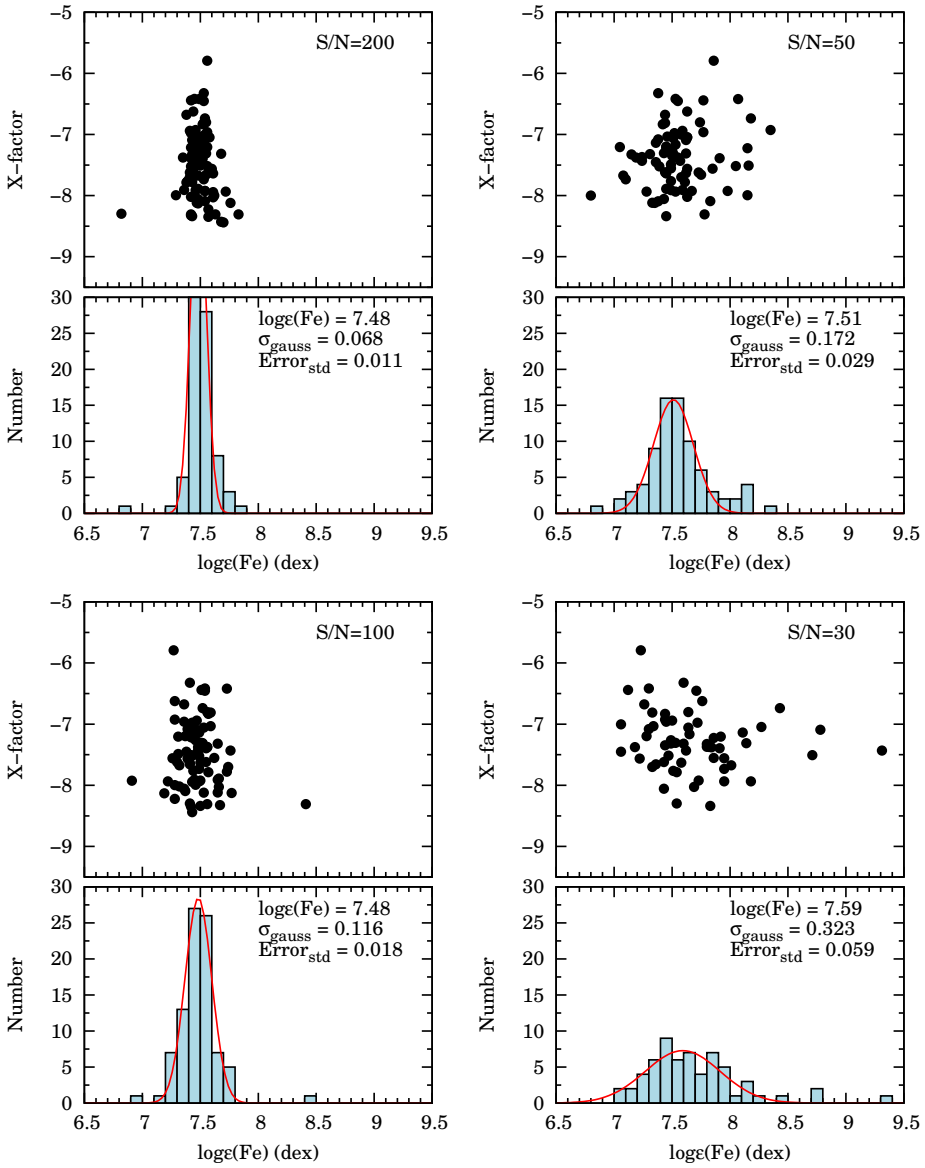

Figure 7.1 Iron abundance derivation using MPFIT for simulated spectra with different S/N.

Table 7.1. Variation of mean iron abundances derived in Figure 7.1.

S/N	[Fe/H] (dex)	Δ[Fe/H] (dex)
200	7.48±0.01	–0.02
100	7.48±0.02	–0.02
50	7.51±0.03	0.01
30	7.59±0.06	0.09

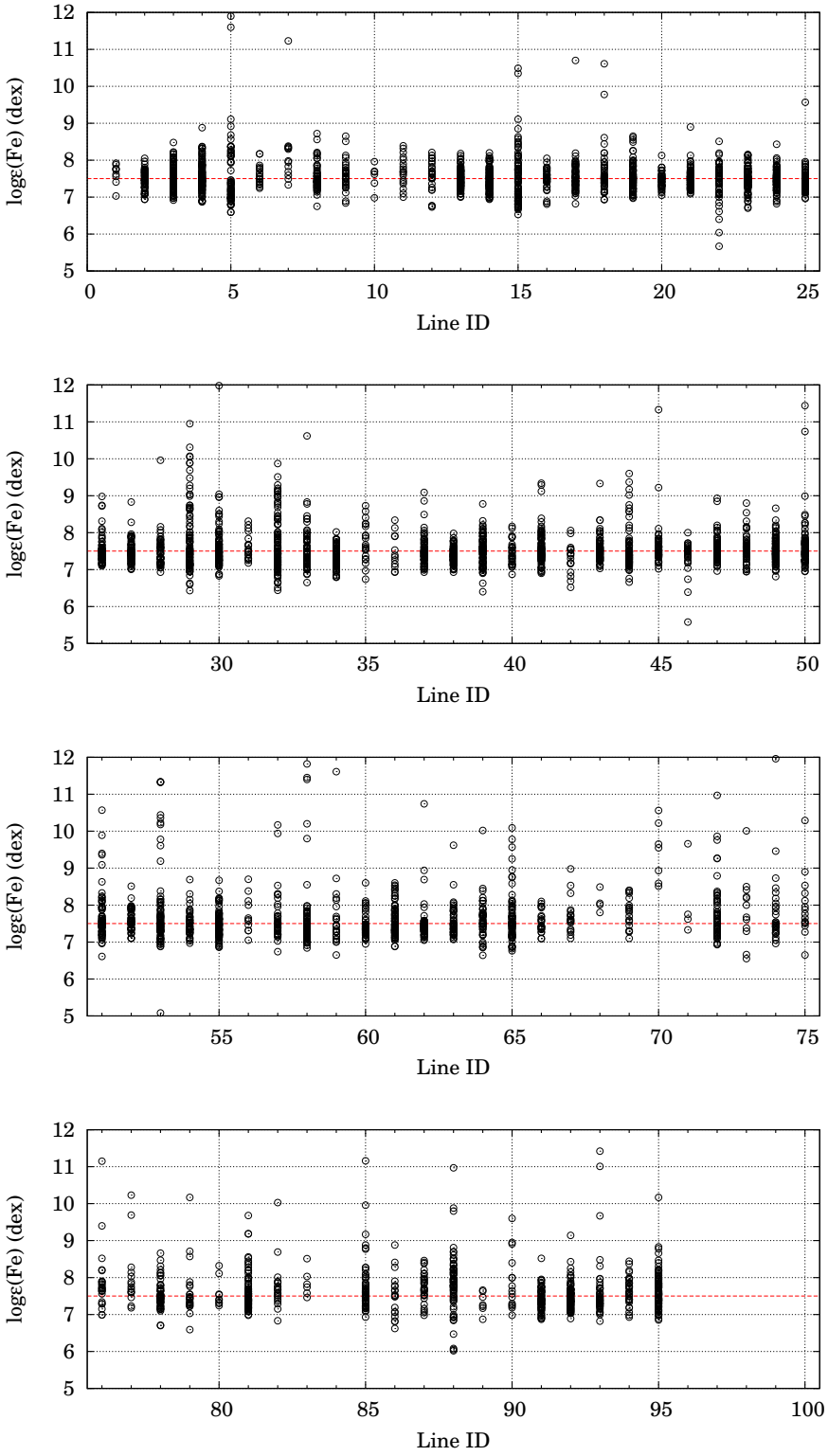

Figure 7.2 Scatters of derived iron abundances for individual Fe I lines present in simulated spectra with S/N=30.

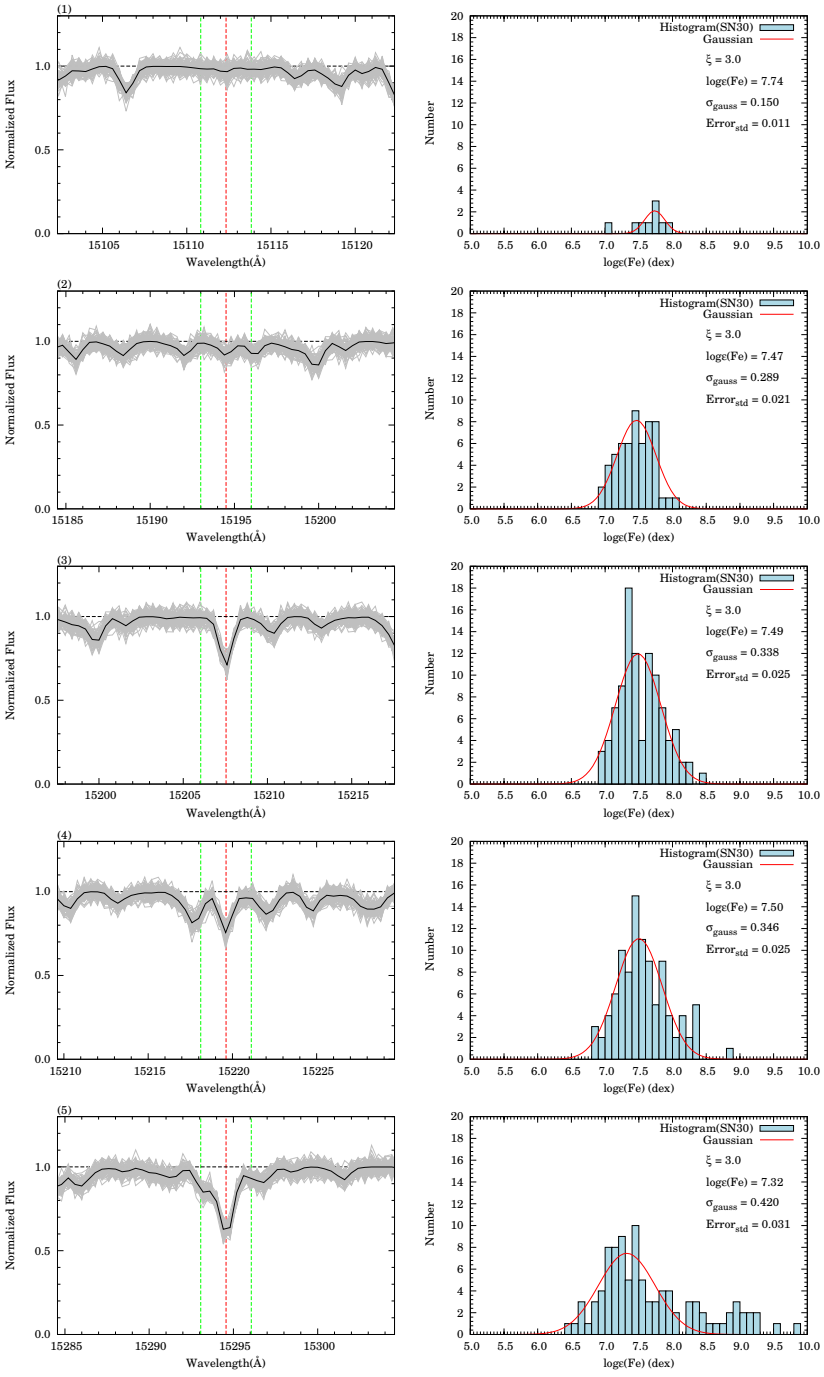

Figure 7.3 Left–simulated synthetic spectra with a high noise level (S/N=30). Right–determination of iron abundances for five Fe I lines as an example.

7.2 Atmospheric parameters

We made use of the LDR method to determine the temperatures of the targets. The lines measured for the LDR indicators are shown in Figure 6.1; but some of the lines for the LDR method are not detected due to the low S/N and/or because some lines are intrinsically too shallow. Table C.3 in Appendix C also list the derived temperatures and the errors. GCC-c shows more atomic and molecule lines than others, which is consistent with its low temperature. Red shapes indicate fitted Gaussian profiles.

The observed phase of GCC-c is different from the others (Table 2.3). Temperatures and radial velocities of Cepheids are related with each other as shown in Figure 6.2 and 6.3. The radial velocities of the target Cepheids at the epoch of our spectroscopic observations were obtained by Matsunaga et al. (2015); GCC-a,b and d are expected to be slightly after the maximum temperatures, and GCC-c is near the phase of the minimum temperature (see Figure 6 of Matsunaga et al., 2015).

7.3 Abundance analysis of the targets

Now, we discuss the microturbulence and the iron abundances of the Cepheids in the Nuclear Stellar Disk. We adopted $\log g = 1.3 \pm 0.5$ dex as the value expected for Cepheids with the period of $\sim$20 days (Takeda et al., 2013), and we set the initial iron abundance of atmosphere models to solar abundance similarly to the analysis for calibration Cepheids. Table 7.2 lists these parameters and the results we obtain as follows.

Figure 7.4–7.7 show how the microturbulences and iron abundances are constrained. These figures indicate that their scatters of abundances are clearly larger than those in case of standard stars. Furthermore, MPFIT failed to get solutions converged for some lines with some given microturbulences. We rejected such lines if we cannot trace well the variations with the microturbulence. There were also rather unexpected variations found for some lines. As seen in the top-left panel of Figure 7.6, for example, a few lines show non-smooth curves and some others are largely offset, (more than 0.5 dex toward the high iron abundance). In some cases, weak lines show unexpectedly large variations with ξ. We rejected these lines as illustrated in Figure 7.4–7.7, and obtained the microturbulence around 3–4 km/s (Table 7.2). We then derived iron abundances based on Gaussian fitting to histograms of measured abundances, as we did for the calibrating objects but with the bin-width of 0.2 dex considering the larger scatters. We found that the averaged abundances are slightly higher than solar, $\sim$0.2 dex, except GCC-c which has a larger iron abundance than the others. The uncertainty due to the errors in atmospheric parameters are listed in Table 7.3.

Table 7.2. Same as Table 6.1, but for target Cepheids.

Object	$T_{\rm eff}$ (K)	$\log g$ (dex)	[M/H] (dex)	ξ (km/s)	[Fe/H] (dex)
GCC-a	5300±290	1.3±0.5	0.20	$4.50^{+1.0}_{-1.0}$	0.23±0.06
GCC-b	5250±250	1.3±0.5	0.20	$2.50^{+0.5}_{-0.5}$	0.20±0.04
GCC-c	4780±160	1.3±0.5	0.50	$3.50^{+0.5}_{-1.0}$	0.51±0.07
GCC-d	5000±120	1.3±0.5	0.10	$2.50^{+0.5}_{-0.5}$	0.11±0.06

Table 7.3. Effects of adopted stellar parameters on [Fe/H] estimates for target Cepheids.

Object	$\sigma_{-\Delta T}$ (dex)	$\sigma_{+\Delta T}$ (dex)	$\sigma_{-\Delta G}$ (dex)	$\sigma_{+\Delta G}$ (dex)	$\sigma_{-\Delta \xi}$ (dex)	$\sigma_{+\Delta \xi}$ (dex)	σ_{all_-} (dex)	σ_{all_+} (dex)
GCC-a	–0.25	0.13	0.01	–0.03	0.01	–0.05	0.26	0.14
GCC-b	–0.10	0.22	0.10	–0.03	0.10	–0.02	0.12	0.27
GCC-c	–0.06	0.04	0.03	–0.02	0.11	–0.05	0.10	0.14
GCC-d	–0.03	0.07	0.07	–0.01	0.06	–0.07	0.10	0.13

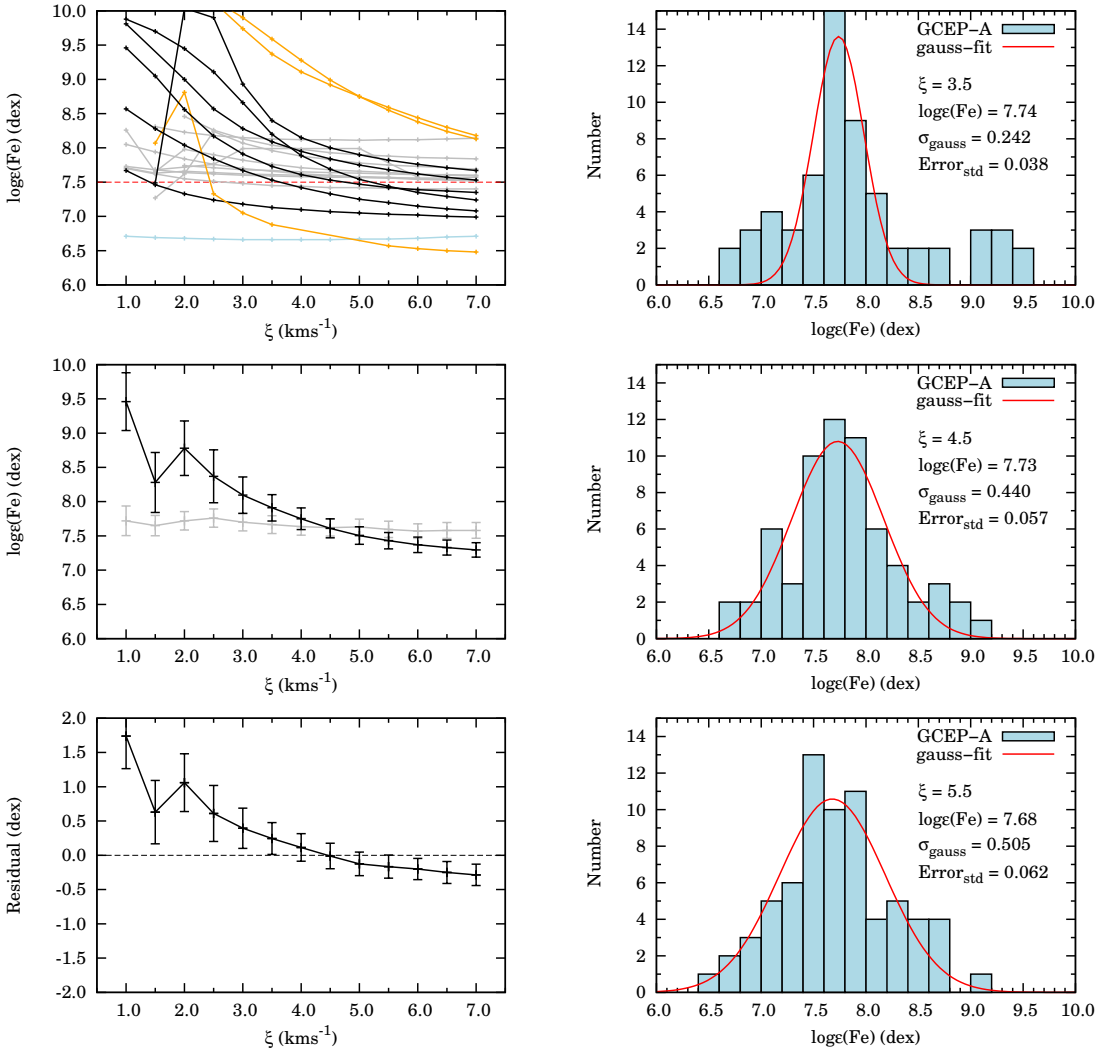

Figure 7.4 The ξ–log ϵ(Fe) plot (left) and histograms of log ϵ(Fe) values (right) from individual lines for GCC-a. See the captions of Figures 3.5 and 3.6 for more details.

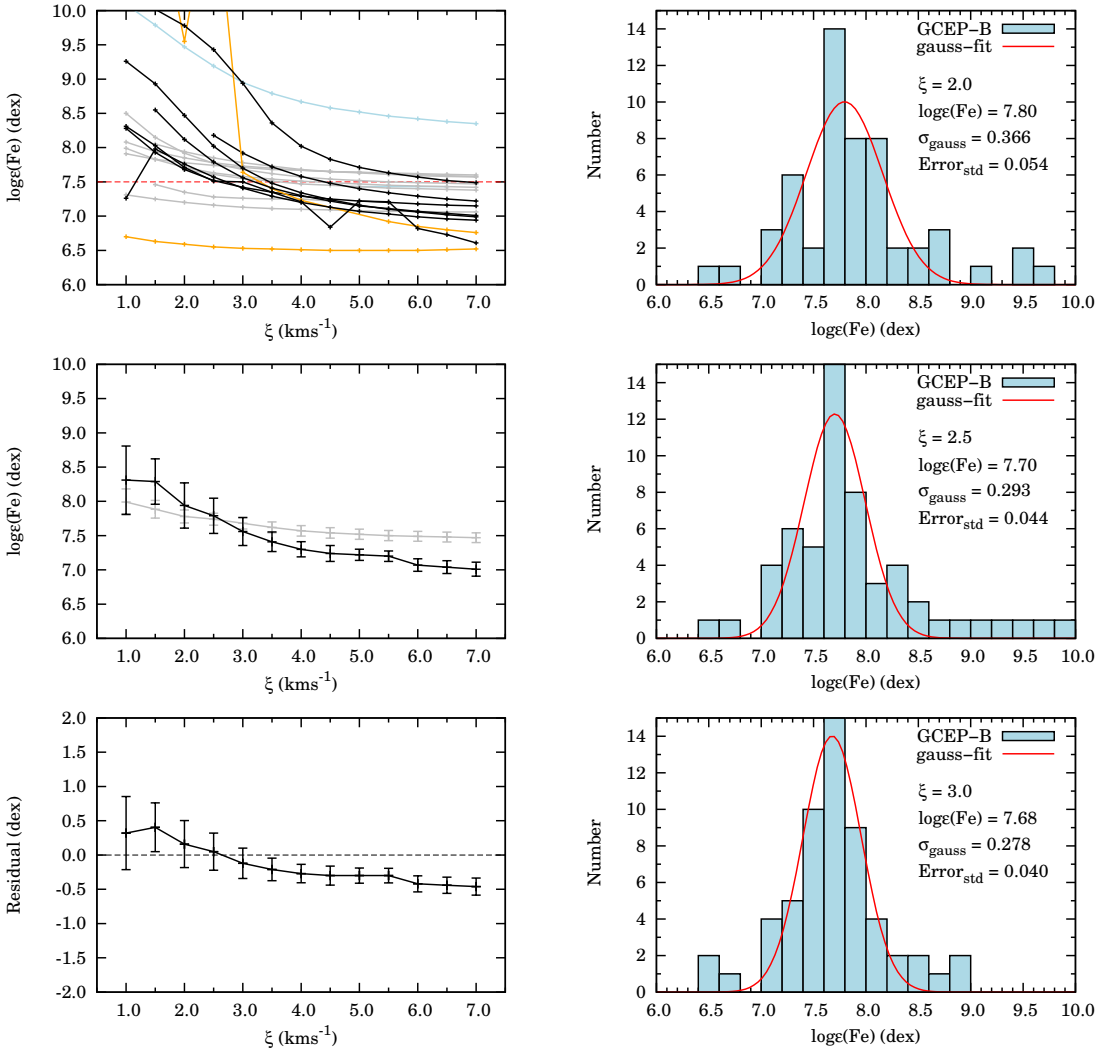

Figure 7.5 Same as Figure 7.4, but for GCC-b.

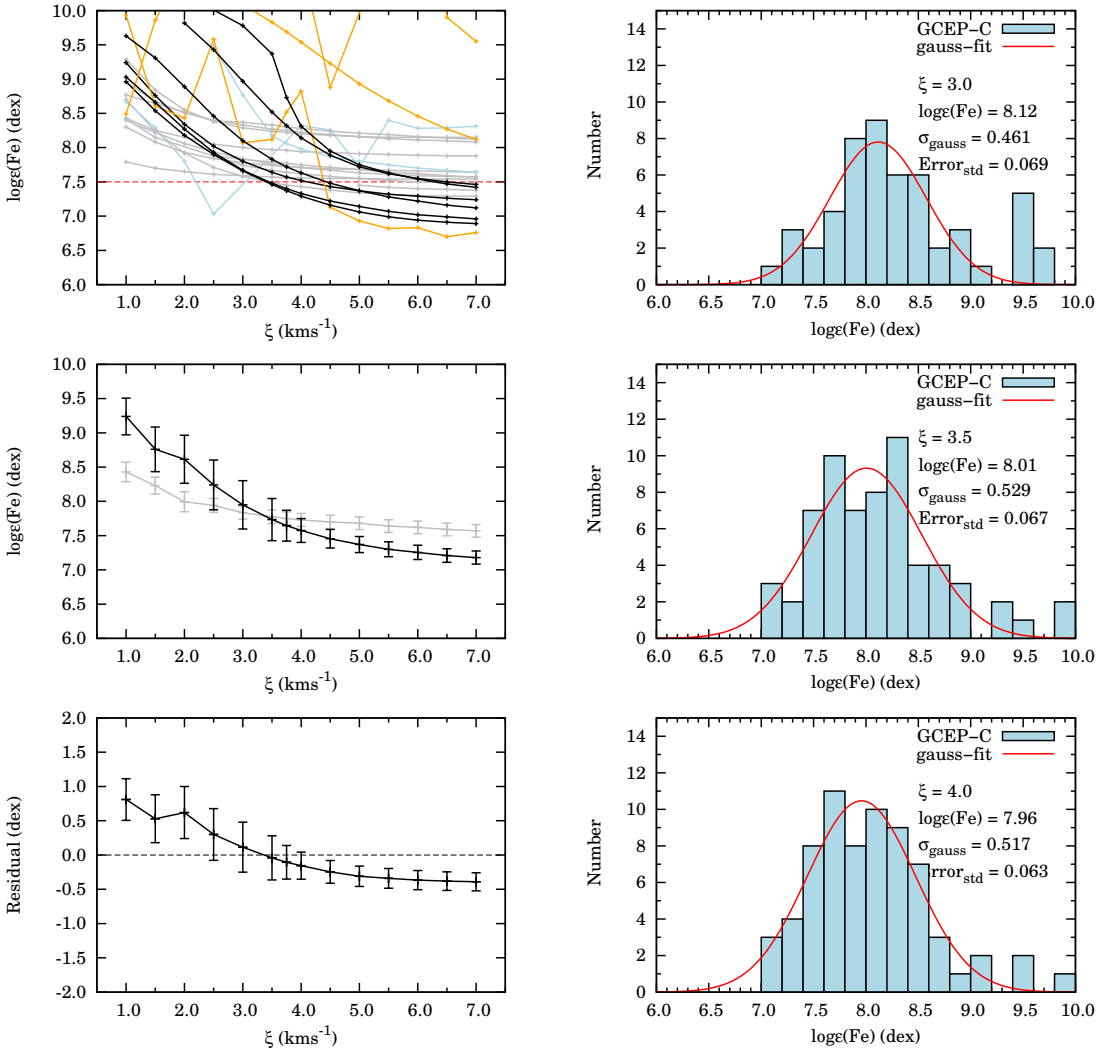

Figure 7.6 Same as Figure 7.4, but for GCC-c.

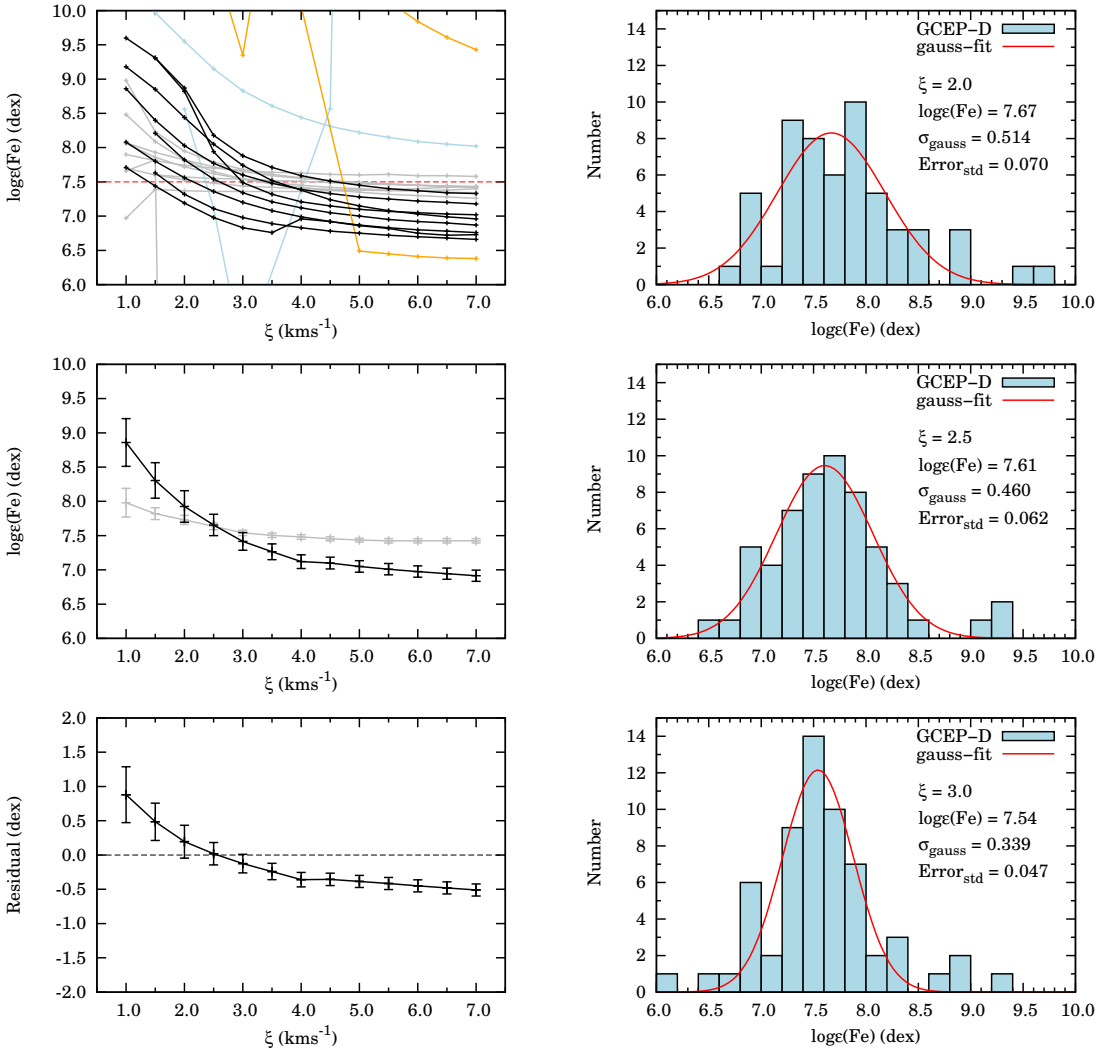

Figure 7.7 Same as Figure 7.4, but for GCC-d.

Table 7.4. Iteration steps in deriving temperature and iron abundance of GCC-c.

	T (K)	[M/H] (dex)	[Fe/H] (dex)	Δ[M/H] (dex)	ΔT (K)
Initial	4780±157	0.00	0.37±0.06	0.37	160
Iteration 1	4940±146	0.37	0.54±0.07	0.17	101
Iteration 2	4940±146	0.54	0.58±0.07	0.04	–

7.4 Iteration to re-determine temperature and iron abundance considering the LDR dependency on metallicity

The derived iron abundance of GCC-c (0.5 dex) is outside the metallicity range of standard stars which were used for the calibration of the LDR temperature scales in Chapter 4. The sensitivity of the LDR method discussed in section 4.3.1 suggests that the offset of Δm =0.5 dex leads to a significant bias in $T_{\rm eff}$, > 100 K. Here we consider a method of incorporating such an bias to re-estimate the temperature and iron abundance iteratively. First, we determine the initial temperature using the LDR relations and derive the iron abundance by MPFIT as already described. When the derived iron abundance m=[Fe/H] is significantly different from the solar value which is the fiducial value for the LDR calibrators, its effect on the temperature at the constant LDR is considered as

$$\Delta T \equiv T - T_0 = \left(\frac{\partial r}{\partial T}\right)^{-1} \left(-\left(\frac{\partial r}{\partial m}\right)(m - m_0)\right), \tag{7.1}$$

where T_0 and m_0 indicate the initial values and effects of other parameters are ignored. As mentioned in section 4.3.1, the effects of $\log g$ and ξ are negligible while that of [X/Fe], ±0.1 dex, is considered as the error source. At the same time, the metallicity [M/H] of the atmosphere model used in the previous stage may be inconsistent with the newly-obtained iron abundance [Fe/H], which requires a correction of the metallicity, Δ[M/H]. With these new parameters, we make another estimate of iron abundance m=[Fe/H] using MPFIT. This estimate can be slightly different from the previous estimate and indicates further offsets in T and [M/H]. We repeat these steps iteratively if necessary. Table 7.4 and Figure 7.8 show the result of the iteration, and we obtained $T_{\rm eff}$ = 4940±146 K and [Fe/H]= 0.58±0.07 dex. The temperature corrections, ΔT, of GCC-a,b and d are smaller than their errors of temperature, so that no iterative corrections were made.

Figure 7.9 plots [Fe/H] of individual lines against excitation potential for GCC-c before and after the iteration. No trend is seen and thus the derived temperature seems to be consistent with the assumption of the excitation balance, although the large scatter and the uneven distribution in EP prevent a firm conclusion based on this plot.

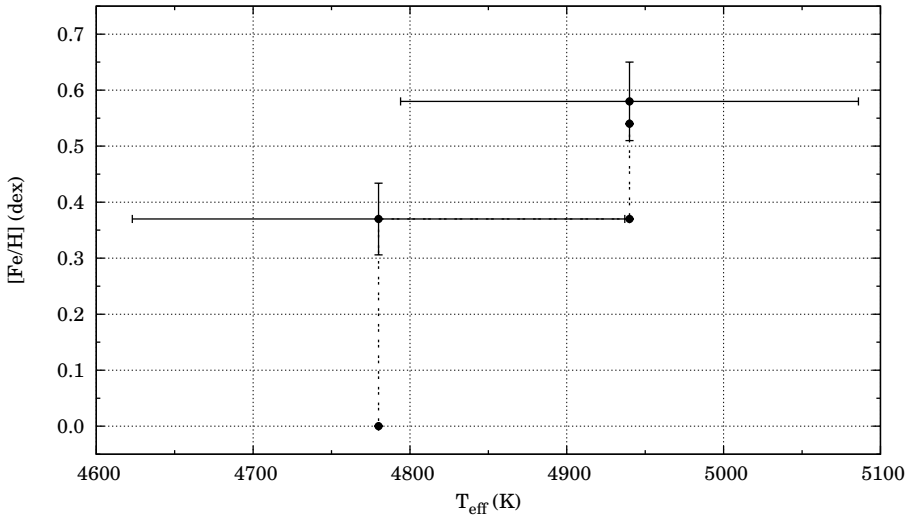

Figure 7.8 The result of the iteration to derive $T_{\rm eff}$ and [Fe/H] of GCC-c (data listed in Table 7.4).

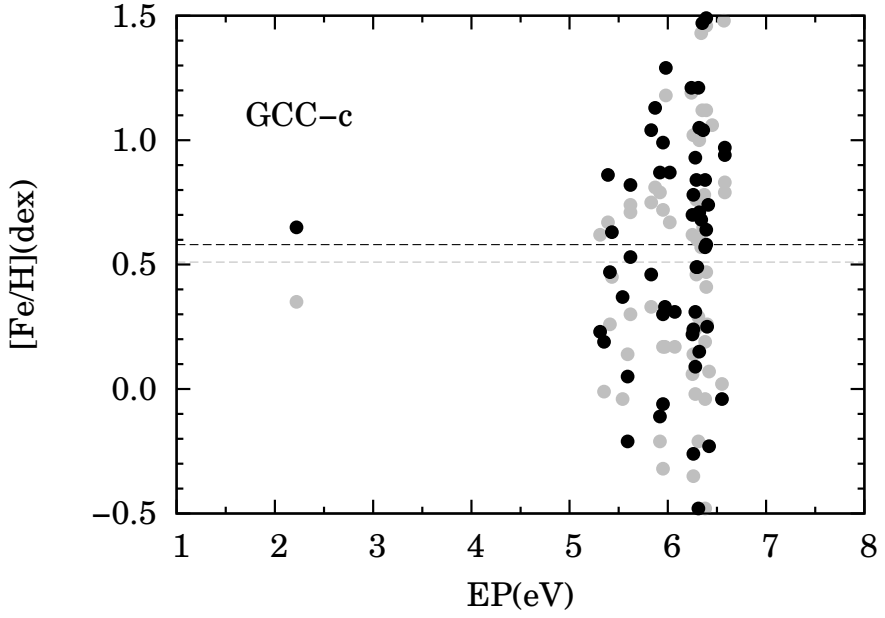

Figure 7.9 [Fe/H] of individual lines plotted against EP to test the excitation balance for GCC-c. Gray points indicate the result without the iteration, while black points indicate the result after the iteration. Horizontal lines indicate the derived iron abundance values.

Chapter 8

Discussion and Summary

8.1 Discussion

In the preceding chapter, we obtained iron abundances of the target Cepheids in the Nuclear Stellar Disk (NSD). Three of them have iron abundances slightly higher than the solar, ∼0.1–0.2 dex, but the other one GCC-c only has a significantly higher value, ∼0.6 dex. Here we compare these with iron abundances of other relevant objects and discuss the implications on the evolution of the NSD. In the following discussions, iron abundances [Fe/H] are scaled with respect to the solar value of $\log \epsilon(\mathrm{Fe})_\odot = 7.50$ dex.

In the Galactic Center region within $R_{\mathrm{GC}} < 60$ pc, there are three prominent clusters, the Central Cluster (a few pc around Sgr A*), the Arches and Quintuplet Clusters (24 and 30 pc, respectively, form Sgr A* in projected distance). Recently, iron abundances of stars in the Central Cluster and Quintuplet have been measured. Cunha et al. (2007) derived abundances of iron, carbon, nitrogen and oxygen of the giant/supergiant stars in the Central Cluster and a supergiant (VR5-7) in Quintuplet with high-resolution H- and K-band spectra. Their iron abundances of the objects in both clusters, 0.01–0.17 dex, agree very well with those of the target Cepheids we derived. Since Cunha et al. (2007) determined effective temperatures with spectroscopic data and ξ by considering the balance between line strength (equivalent width) and iron abundance, their results can be directly compared with ours. Davies et al. (2009b) observed two red supergiants (IRC7 and VR5-7) among the targets of Cunha et al. (2007) and obtained similar values. The youngest stars in these two clusters are 3–9 Myr (the Central Cluster, Blum et al., 1996; Cunha et al., 2007, and references therein) and 3–5 Myr (Quintuplet; Figer et al., 1999). Ryde & Schultheis (2015) investigated nine red giants around the Galactic Center (within 7–9 pc). Ages of their targets are not well constrained, but they are generally considered to be several Gyr or higher. Iron abundances of these red giants are higher than the solar except two (−0.04 and −0.13 dex). These previous results are summarized in Table 8.1 and compared with our result on the NSD Cepheids in Figure 8.1. Almost all of the objects have comparable iron abundances slightly higher than the solar irrespective of the ages and the locations within the NSD. Histogram of the iron abundances of the aforementioned objects in the NSD is given in the top panel of Figure 8.2. The sharp peak, at around the mean value of $\langle[\mathrm{Fe/H}]\rangle = 0.07$ dex, is in contrast to a large spread of the iron abundances of stars in the surrounding Galactic bulge. As an example, the second panel of Figure 8.2 shows the histogram for red clump stars in the bulge (Hill et al., 2011). This suggests

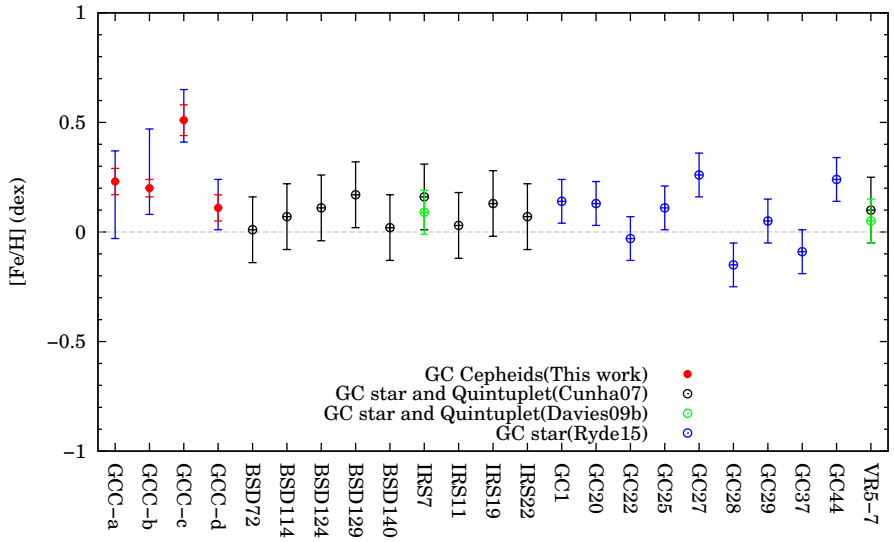

Figure 8.1 Comparison of iron abundances of stars in the Galactic Center region (the four Cepheids we investigated, on the left, and others in the literature in the middle). Table 8.1 gives the literature values.

that chemical evolution of the NSD is completely different from that of the bulge and that the iron abundances of stars in the NSD have remained more-or-less constant since few Gyr ago although the number of stars with iron abundance measured is still limited.

Figure 8.3 compares our result with metallicity distribution of Galactic Cepheids (Genovali et al., 2014). Iron abundances of calibration Cepheids we derived, as expected, fall well within the metallicity distribution of others. Our measurements allow us to compare the iron abundances in the NSD directly with the metallicity gradient of the disk ($R_{\rm GC} > 4$ kpc) using tracers of the same kind. The last three panel of Figure 8.2 show histograms for Cepheids in different ranges of $R_{\rm GC}$. The metallicity gradient is again clearly illustrated by decreasing mean values from $\langle$[Fe/H]$\rangle = 0.24$ dex ($4 < R_{\rm GC} < 6$ kpc) to 0.04 dex ($6 < R_{\rm GC} < 9$ kpc) and -0.08 dex ($9 < R_{\rm GC} < 13$ kpc) toward the outer disk.

Star formation in the NSD has been taking plane since at least a few Gyr ago (Blum et al., 2003; Figer et al., 2004). For explaining such prolonged star formation, mechanism to supply gas to the NSD is required. The following three sources of gas supply can be considered. (1) The gas of the Galactic disk falling into NSD through the Galactic bar (Stark et al., 2004). Such gas is likely as metal-rich as the Cepheids in the inner disk (Figure 8.2). (2) Mass-loss gas ejected from old stars in the Galactic bulge (Cunha et al., 2007). While the bulge stars have a wide range iron abundances (–1∼0.5 dex), recycled gas would be well mixed so that stars formed from this mechanism are considered to be rather chemically homogeneous at around the average iron abundance. (3) Gas falling from the halo (Barger et al., 2012). Such gas represented by high-velocity clouds in the halo are metal-poor (e.g., Richter et al., 2015).

Metallicity distributions and the averages illustrated in Figure 8.2 provide an important clue to the scenario of the gas fueling. The average iron abundance of the NSD stars and that of the bulge stars agree with each other. This supports that star formation in the NSD has been fueled by mass-loss gas from the bulge. Cunha et al. (2007) also indicated the contribution of the mass-loss gas in the

Table 8.1. Iron abundances of stars in the Galactic Center region found in the literature.

Region	Object	Spectral Type	R_{GC} (pc)	[Fe/H] (dex)	Reference
Central Cluster	BSD72	M	1.60	0.01±0.15	Cunha et al.(2007)
	BSD114	M	2.10	0.07±0.15	Cunha et al.(2007)
	BSD124	M	1.90	0.11±0.15	Cunha et al.(2007)
	BSD129	M	2.20	0.17±0.15	Cunha et al.(2007)
	BSD140	M	2.00	0.02±0.15	Cunha et al.(2007)
	IRS7	M2 I	0.21	0.16±0.15	Cunha et al.(2007)
	IRS7	M2 I	0.21	0.09±0.10	Davies et al.(2009)
	IRS11	M	0.62	0.03±0.15	Cunha et al.(2007)
	IRS19	M	1.00	0.13±0.15	Cunha et al.(2007)
	IRS22	M	1.00	0.07±0.15	Cunha et al.(2007)
	Average	—	2.00	0.04±0.12	Cunha et al.(2007)
Quintuplet	VR5-7	M I	31.00	0.10±0.15	Cunha et al.(2007)
	VR5-7	M I	31.00	0.05±0.10	Davies et al.(2009)
Galactic Center	GC1	M III	10.00	0.14±0.10	Ryde & Schultheis(2015)
	GC20	M III	10.00	0.13±0.10	Ryde & Schultheis(2015)
	GC22	M III	10.00	−0.03±0.10	Ryde & Schultheis(2015)
	GC25	M III	10.00	0.11±0.10	Ryde & Schultheis(2015)
	GC27	M III	10.00	0.26±0.10	Ryde & Schultheis(2015)
	GC28	M III	10.00	−0.15±0.10	Ryde & Schultheis(2015)
	GC29	M III	10.00	0.05±0.10	Ryde & Schultheis(2015)
	GC37	M III	10.00	−0.09±0.10	Ryde & Schultheis(2015)
	GC44	M III	10.00	0.24±0.10	Ryde & Schultheis(2015)
	Average	—	10.00	0.06±0.15	Ryde & Schultheis(2015)

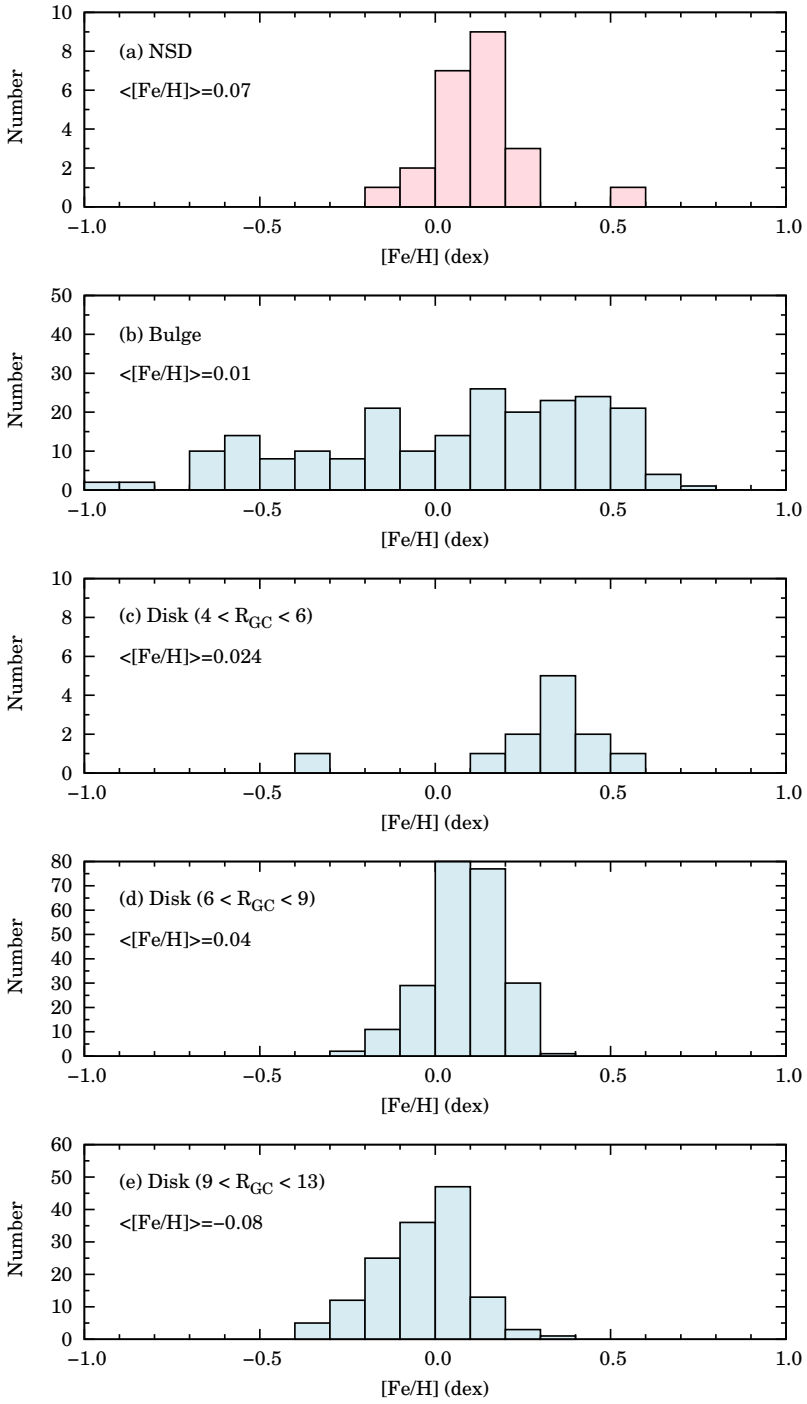

Figure 8.2 Histogram of the iron abundances of stars in a few different regions: (a) 23 giant and supergiant stars in the NSD from Cunha et al. (2007), Davies et al. (2009b), Ryde & Schultheis (2015) and this work, (b) 218 red clump stars in the bulge from Hill et al. (2011), (c) to (e) histograms for 385 Cepheids in different ranges of $R_{\rm GC}$ from Genovali et al. (2014).

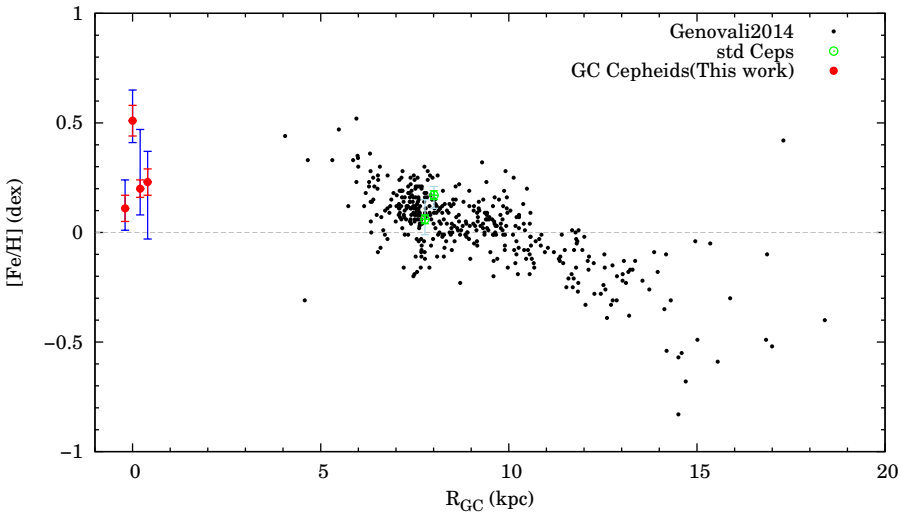

Figure 8.3 Metallicity gradient of Cepheids. Red and green open circle indicate our four Cepheids and two standard Cepheids, respectively. Black dots are taken from Genovali et al. (2014).

bulge. However, it is difficult to explain the high iron abundance of GCC-c by this process. Each old evolved star in the bulge supplies only a small amount of gas, $\sim 0.3 M_{\odot}$, with slow stellar wind. A large number of stars should contribute to clouds where star formation can occur, and thus the iron abundance spread should be averaged out. The iron abundance of GCC-c may be explained by a fall of metal-rich gas cloud from the inner disk. Stars formed in such a cloud would be metal-rich if star formation occurs before it is mixed with other (solar-metal) gas in the NSD. Although the low S/N of its spectrum alerts us to the need for further careful investigations, e.g. independent measurements of the iron abundance with a higher-S/N spectrum, this object can be the first object in the NSD which shows a chemical signature indicative of gas from the inner disk.

8.2 Summary

In this thesis, we determined iron abundances of four Cepheids in the Nuclear Stellar Disk (NSD) with high-resolution H-band spectra of *Subaru*/IRCS. In the first step, for standard stars with well-defined parameters, we examined abundance analysis tool based on ATLAS9 and MPFIT, and selected the atomic linelist to use. The analysis tool worked quite well and we found that the linelist by Meléndez & Barbuy (1999) gives reasonable abundances with the H-band spectra. In addition, we found that we can determine microturbulence using the ξ–$\log\epsilon$(Fe) plot to the accuracy of $\sim$0.5 km/s. The next step was determination of effective temperature using the LDR. With the same static stars, we defined nine temperature indicators constructed with Fe, K, Ti, Co, Al, Si lines. We achieved determination accuracy of $\sim$40 K in weighted averages from the nine pairs. Then, we applied the above methods to calibration Cepheids (δ Cep and X Cyg). The derived temperatures using LDRs agree with those expected from the cyclic variations in the literature, and iron abundances we obtained are also consistent with previous results. Finally, we determined temperatures and iron abundances of our target Cepheids in the NSD. For these Cepheids, however, we only obtained low-quality spectra with S/N=30–70. Statistical errors of the temperatures and iron abundances are 120–300 K and 0.06 dex, respectively. Our results on the NSD Cepheids show super-solar metallicities, $\sim$0.2 dex in three of the Cepheids, but the rest one is significantly metal-rich ($\geq$ 0.5 dex). Previous results for other stars in the same region, 0.0–0.2 dex, are in good agreement with ours for the first three stars, which suggests that iron abundances in the NSD have remained almost constant over the last few Gyrs. The bulk of the star formations in the NSD is suggested to be fueled by mass-loss gas in the bulge, because the averaged iron abundance of NSD stars consistent with that of the bulge stars. Besides, the one star with the high iron abundance may indicate inflowing of metal-rich gas from the inner disk.

In this study, we focused on iron abundance. Abundances of other elements, e.g. α elements, would provide us with further crucial constraints on the chemical evolution (e.g., Genovali et al., 2015). Since H-band spectra include lines of a large number of elements, it is possible to extract more clues to chemical composition of the inner Galaxy from the spectra of our Cepheids.

Acknowledgment

First of all, I am very grateful to my supervisor Dr. Naoto Kobayashi for encouraging me through my graduate course. I also would like to express my deepest appreciation to Dr. Noriyuki Matsunaga for giving me invaluable suggestions throughout my thesis work. Without his supervision and dedicated encouragement, this thesis could not have been finished. He also fully supported my graduate-course life at the Department of Astronomy in Hongo, which became my fond memory. I am very grateful to my collaborators, Dr. Sohei Kondo, Dr. Yuji Ikeda. Dr. Sohei Kondo who helped me with developing the methods of abundance analysis. Dr. Yuji Ikeda gave me fundamental knowledge of spectrometric observation and optics design.

My project was also supported by observations and discussions with Mr. Ryo Yamamoto, Dr. Satoshi Hamano, Dr. Chikako Yasui and Dr. Takayuki Arasaki. I appreciate the feedback offered by Dr. Yoichi Takeda. I would like to thank Dr. Takuji Tsujimoto, Dr. Giuseppe Bono and Dr. Laura Inno for their valuable comments. We are grateful to Subaru support astronomers, Dr. Miki Ishii, Dr. Yosuke Minowa, and Dr. Tae-Soo Pyo, for their help during our Subaru observations in 2010 and 2012.

I also thank all of the students and staffs of LiH at Koyama Astronomical Observatory, Kyoto Sangyo University for their cooperation for my study. Especially, Dr. Hideyo Kawakita, Mr. Kensi Nakanishi, Mr. Takafumi Kawanishi, Mr. Tetsuya Nakaoka, Mr. Shogo Otsubo for their cooperation for my study. I am also grateful to my colleagues, Ms. Natsuko Izumi, Mr. Misaki Mizumoto, Ms. Haruka Takahasi and Mr. Daisuke Taniguchi.

Finally, I would like to appreciate my family for supporting and encouraging me.

Bibliography

Alonso, A., Arribas, S., & Martinez-Roger, C. 1996, A&A, 313, 873

Anders, E., & Grevesse, N. 1989, Geochim. Cosmochim. Acta, 53, 197

Andrievsky, S. M., Luck, R. E., Martin, P., & Lépine, J. R. D. 2004, A&A, 413, 159

Andrievsky, S. M., Luck, R. E., & Kovtyukh, V. V. 2005, AJ, 130, 1880

Asplund, M., Grevesse, N., & Sauval, A. J. 2005, Cosmic Abundances as Records of Stellar Evolution and Nucleosynthesis, 336, 25

Asplund, M., Grevesse, N., Sauval, A. J., & Scott, P. 2009, ARA&A, 47, 481

Axer, M., Fuhrmann, K., & Gehren, T. 1994, A&A, 291, 895

Barger, K. A., Haffner, L. M., Wakker, B. P., et al. 2012, ApJ, 761, 145

Bell, R. A., Edvardsson, B., & Gustafsson, B. 1985, MNRAS, 212, 497

Bensby, T., Feltzing, S., Lundström, I., & Ilyin, I. 2005, A&A, 433, 185

Bergemann, M., Hansen, C. J., Bautista, M., & Ruchti, G. 2012, A&A, 546, A90

Blackwell, D. E., & Willis, R. B. 1977, MNRAS, 180, 169

Blum, R. D., Sellgren, K., & Depoy, D. L. 1996, AJ, 112, 1988

Blum, R. D., Ramírez, S. V., Sellgren, K., & Olsen, K. 2003, ApJ, 597, 323

Bono, G., Marconi, M., Cassisi, S., et al. 2005, ApJ, 621, 966

Branch, D., Bonnell, J., & Tomkin, J. 1978, ApJ, 225, 902

Britavskiy, N. E., Andrievsky, S. M., Tsymbal, V. V., et al. 2012, A&A, 542, A104

Brown, J. A., & Wallerstein, G. 1992, AJ, 104, 1818

Bruntt, H., Frandsen, S., & Thygesen, A. O. 2011, A&A, 528, A121

Castro, S., Rich, R. M., McWilliam, A., et al. 1996, AJ, 111, 2439

Carr, J. S., Sellgren, K., & Balachandran, S. C. 2000, ApJ, 530, 307

Cayrel de Strobel, G., Chauve-Godard, J., Hernandez, G., & Vaziaga, M. J. 1970, A&A, 7, 408

Cayrel, R., Perrin, M. N., Buser, R., Barbuy, B., & Coupry, M. F. 1991, A&A, 247, 122

Cenarro, A. J., Cardiel, N., Gorgas, J., et al. 2001, MNRAS, 326, 959

Cenarro, A. J., Peletier, R. F., Sánchez-Blázquez, P., et al. 2007, MNRAS, 374, 664

Chiappini, C., Matteucci, F., & Romano, D. 2001, ApJ, 554, 1044

Clementini, G., Gratton, R. G., Carretta, E., & Sneden, C. 1999, MNRAS, 302, 22

Coelho, P., Barbuy, B., Meléndez, J., Schiavon, R. P., & Castilho, B. V. 2005, A&A, 443, 735

Cunha, K., Sellgren, K., Smith, V. V., et al. 2007, ApJ, 669, 1011

Davies, B., Origlia, L., Kudritzki, R.-P., et al. 2009a, ApJ, 694, 46

Davies, B., Origlia, L., Kudritzki, R.-P., et al. 2009b, ApJ, 696, 2014

Davies, B., de La Fuente, D., Najarro, F., et al. 2012, MNRAS, 419, 1860

Dékány, I., Minniti, D., Majaess, D., et al. 2015, ApJ, 812, L29

Edvardsson, B. 1988, A&A, 190, 148

Feast, M. W., Menzies, J. W., Matsunaga, N., & Whitelock, P. A. 2014, Nature, 509, 342

Feltzing, S., & Gonzalez, G. 2001, A&A, 367, 253

Fernandez-Villacanas, J. L., Rego, M., & Cornide, M. 1990, AJ, 99, 1961

Figer, D. F., McLean, I. S., & Morris, M. 1999, ApJ, 514, 202

Figer, D. F., Rich, R. M., Kim, S. S., Morris, M., & Serabyn, E. 2004, ApJ, 601, 319

Frasca, A., Covino, E., Spezzi, L., et al. 2009, A&A, 508, 1313

Friel, E. D., & Janes, K. A. 1993, A&A, 267, 75

Fukue, K., Matsunaga, N., Yamamoto, R., et al. 2015, ApJ, 812, 64

Fuhrmann, K. 1998, A&A, 338, 161

Fulbright, J. P. 2000, AJ, 120, 1841

Fulbright, J. P., McWilliam, A., & Rich, R. M. 2006, ApJ, 636, 821

Gehren, T., Liang, Y. C., Shi, J. R., Zhang, H. W., & Zhao, G. 2004, A&A, 413, 1045

Genovali, K., Lemasle, B., Bono, G., et al. 2014, A&A, 566, A37

Genovali, K., Lemasle, B., da Silva, R., et al. 2015, A&A, 580, A17

Gilmore, G., Randich, S., Asplund, M., et al. 2012, The Messenger, 147, 25

Gonzalez, G., & Wallerstein, G. 1998, AJ, 116, 765

Gouda, N., & Working Group, J. 2010, Transactions of the Japanese Society for Artificial Intelligence, Aerospace Technology Japan, 8,

Gratton, L., Gaudenzi, S., Rossi, C., & Gratton, R. G. 1982, MNRAS, 201, 807

Gratton, R. G., & Ortolani, S. 1986, A&A, 169, 201

Gratton, R. G., & Sneden, C. 1990, A&A, 234, 366

Gratton, R. G., Carretta, E., Claudi, R., Lucatello, S., & Barbieri, M. 2003, A&A, 404, 187

Gratton, R., Bragaglia, A., Carretta, E., & Tosi, M. 2006, ApJ, 642, 462

Gray, D. F., & Johanson, H. L. 1991, PASP, 103, 439

Grevesse, N., & Noels, A. 1993, Origin and Evolution of the Elements, 15

Grevesse, N., Noels, A., & Sauval, A. J. 1996, Cosmic Abundances, 99, 117

Gustafsson, B., Bell, R. A., Eriksson, K., & Nordlund, A. 1975, A&A, 42, 407

Hauschildt, P. H., Baron, E., & Allard, F. 1997, ApJ, 483, 390

Hayano, Y., Takami, H., Oya, S., et al. 2010, Proc. SPIE, 7736, 77360N

Haywood, M., Di Matteo, P., Lehnert, M. D., Katz, D., & Gómez, A. 2013, A&A, 560, A109

Heiter, U., Jofré, P., Gustafsson, B., et al. 2015, arXiv:1506.06095

Hekker, S., & Meléndez, J. 2007, A&A, 475, 1003

Hill, V. 1997, A&A, 324, 435

Hill, V., Lecureur, A., Gómez, A., et al. 2011, A&A, 534, A80

Hinkle, K., Wallace, L., & Livingston, W. 1995, PASP, 107, 1042

Ivezić, Ž., Beers, T. C., & Jurić, M. 2012, ARA&A, 50, 251

Jacobson, H. R., Friel, E. D., & Pilachowski, C. A. 2011, AJ, 141, 58

Johnson, H. L., Mitchell, R. I., Iriarte, B., & Wisniewski, W. Z. 1966, Communications of the Lunar and Planetary Laboratory, 4, 99

Kobayashi, N., Tokunaga, A. T., Terada, H., et al. 2000, Proc. SPIE, 4008, 1056

Koleva, M., & Vazdekis, A. 2012, A&A, 538, A143

Kovtyukh, V. V., Gorlova, N. I., & Klochkova, V. G. 1998, Astronomy Letters, 24, 372

Kovtyukh, V. V., & Gorlova, N. I. 2000, A&A, 358, 587

Kovtyukh, V. V., Andrievsky, S. M., Belik, S. I., & Luck, R. E. 2005, AJ, 129, 433

Kovtyukh, V. V., Soubiran, C., Bienaymé, O., Mishenina, T. V., & Belik, S. I. 2006, MNRAS, 371, 879

Kovtyukh, V. V. 2007, MNRAS, 378, 617

Kuroczkin, D., & Wiszniewski, A. 1977, AcA, 27, 145

Kurucz, R. 1993a, ATLAS9 Stellar Atmosphere Programs and 2 km/s grid. Kurucz CD-ROM No. 13. Cambridge, Mass.: Smithsonian Astrophysical Observatory, 1993., 13,

Kurucz, R. 1993b, Diatomic Molecular Data for Opacity Calculations. Kurucz CD-ROM No. 15. Cambridge, Mass.: Smithsonian Astrophysical Observatory, 1993., 15,

Kyrolainen, J., Tuominen, I., Vilhu, O., & Virtanen, H. 1986, A&AS, 65, 11

Lambert, D. L., & Ries, L. M. 1981, ApJ, 248, 228

Launhardt, R., Zylka, R., & Mezger, P. G. 2002, A&A, 384, 112

Lee, Y. S., Beers, T. C., Allende Prieto, C., et al. 2011, AJ, 141, 90

Leep, E. M., Wallerstein, G., & Oke, J. B. 1987, AJ, 93, 338

Lemasle, B., François, P., Piersimoni, A., et al. 2008, A&A, 490, 613

Luck, R. E. 1977, ApJ, 212, 743

Luck, R. E. 1982, ApJ, 256, 177

Luck, R. E., & Challener, S. L. 1995, AJ, 110, 2968

Luck, R. E., & Heiter, U. 2005, AJ, 129, 1063

Luck, R. E., & Heiter, U. 2006, AJ, 131, 3069

Luck, R. E., Kovtyukh, V. V., & Andrievsky, S. M. 2006, AJ, 132, 902

Luck, R. E., Andrievsky, S. M., Kovtyukh, V. V., Gieren, W., & Graczyk, D. 2011, AJ, 142, 51

Luck, R. E., & Lambert, D. L. 2011, AJ, 142, 136

Maeckle, R., Holweger, H., Griffin, R., & Griffin, R. 1975, A&A, 38, 239

Mashonkina, L., & Gehren, T. 2000, A&A, 364, 249

Matsunaga, N., Kawadu, T., Nishiyama, S., et al. 2011, Nature, 477, 188

Matsunaga, N., Feast, M. W., Kawadu, T., et al. 2013, MNRAS, 429, 385

Matsunaga, N. 2014, EAS Publications Series, 67, 279

Matsunaga, N., Fukue, K., Yamamoto, R., et al. 2015, ApJ, 799, 46

McWilliam, A. 1990, ApJS, 74, 1075

McWilliam, A., & Rich, R. M. 1994, ApJS, 91, 749

Meléndez, J., & Barbuy, B. 1999, ApJS, 124, 527

Meléndez, J., Asplund, M., Alves-Brito, A., et al. 2008, A&A, 484, L21

Minchev, I., Chiappini, C., & Martig, M. 2013, A&A, 558, A9

Mishenina, T. V., & Kovtyukh, V. V. 2001, A&A, 370, 951

Mishenina, T. V., Kovtyukh, V. V., Korotin, S. A., & Soubiran, C. 2003, Astronomy Reports, 47, 422

Mucciarelli, A. 2011, A&A, 528, A44

Niemczura, E., Smalley, B., & Pych, W. 2014, Determination of Atmopsheric Parameters of B-, A-, F- and G-Type Stars Lectures from the School of Spectroscopic Data Analyses, ed Niemczura, E., Smalley, B., Pych, W. (Berlin, Springer-Verlag), 85

Nishiyama, S., Nagata, T., Tamura, M., et al. 2008, ApJ, 680, 1174

Notsu, S., Honda, S., Notsu, Y., et al. 2013, PASJ, 65, 112

Oinas, V. 1974, ApJS, 27, 405

Oinas, V. 1977, A&A, 61, 17

Origlia, L., Oliva, E., Maiolino, R., et al. 2013, A&A, 560, A46

Origlia, L., Oliva, E., Sanna, N., et al. 2015, arXiv:1510.06870

Pedicelli, S., Bono, G., Lemasle, B., et al. 2009, A&A, 504, 81

Perryman, M. A. C., Lindegren, L., Kovalevsky, J., et al. 1997, A&A, 323,

Peterson, R. 1976, ApJS, 30, 61

Peterson, R. C., Dalle Ore, C. M., & Kurucz, R. L. 1993, ApJ, 404, 333

Prugniel, P., Vauglin, I., & Koleva, M. 2011, A&A, 531, A165

Qui, H.-M., Zhao, G., Takada-Hidai, M., et al. 2002, PASJ, 54, 103

Ramírez, I., Allende Prieto, C., & Lambert, D. L. 2007, A&A, 465, 271

Ramírez, I., & Allende Prieto, C. 2011, ApJ, 743, 135

Randich, S., Gratton, R., Pallavicini, R., Pasquini, L., & Carretta, E. 1999, A&A, 348, 487

Reylé, C., Marshall, D. J., Schultheis, M., & Robin, A. C. 2008, SF2A-2008, 29

Richter, P., de Boer, K. S., Werner, K., & Rauch, T. 2015, A&A, 584, L6

Ryde, N., Edvardsson, B., Gustafsson, B., et al. 2009, A&A, 496, 701

Ryde, N., & Schultheis, M. 2015, A&A, 573, A14

Saffe, C., & Levato, H. 2004, A&A, 418, 1083

Sánchez-Blázquez, P., Peletier, R. F., Jiménez-Vicente, J., et al. 2006, MNRAS, 371, 703

Sandage, A., Tammann, G. A., Saha, A., et al. 2006, ApJ, 653, 843

Santos, N. C., Israelian, G., & Mayor, M. 2000, A&A, 363, 228

Sasselov, D. D., & Lester, J. B. 1990, ApJ, 360, 227

Schönrich, R., & Binney, J. 2009, MNRAS, 396, 203

Sheffield, A. A., Majewski, S. R., Johnston, K. V., et al. 2012, ApJ, 761, 161

Sheminova, V. A. 1993, Kinematika i Fizika Nebesnykh Tel, 9, 27

Smith, G., & Ruck, M. J. 2000, A&A, 356, 570

Smith, V. V., Cunha, K., Shetrone, M. D., et al. 2013, ApJ, 765, 16

Sneden, C., Kraft, R. P., Langer, G. E., Prosser, C. F., & Shetrone, M. D. 1994, AJ, 107, 1773

Soubiran, C., Bienaymé, O., Mishenina, T. V., & Kovtyukh, V. V. 2008, A&A, 480, 91

Sozzetti, A., Torres, G., Latham, D. W., et al. 2009, ApJ, 697, 544

Stark, A. A., Martin, C. L., Walsh, W. M., et al. 2004, ApJ, 614, L41

Storm, J., Carney, B. W., Gieren, W. P., et al. 2004, VizieR Online Data Catalog, 341, 50531

Takeda, Y. 1995, PASJ, 47, 287

Takeda, Y., Ohkubo, M., Sato, B., Kambe, E., & Sadakane, K. 2005, PASJ, 57, 27

Takeda, Y. 2007, PASJ, 59, 335

Takeda, Y., Kaneko, H., Matsumoto, N., et al. 2009, PASJ, 61, 563

Takeda, Y., Kang, D.-I., Han, I., Lee, B.-C., & Kim, K.-M. 2013, MNRAS, 432, 769

Thévenin, F., & Idiart, T. P. 1999, ApJ, 521, 753

Thygesen, A. O., Frandsen, S., Bruntt, H., et al. 2012, A&A, 543, A160

Tomkin, J., & Lambert, D. L. 1999, ApJ, 523, 234

Tsujimoto, T., Bland-Hawthorn, J., & Freeman, K. C. 2010, PASJ, 62, 447

Twarog, B. A., Ashman, K. M., & Anthony-Twarog, B. J. 1997, AJ, 114, 2556

Wallace, L., Livingston, W., Hinkle, K., & Bernath, P. 1996, ApJS, 106, 165

Worley, C. C., Cottrell, P. L., Freeman, K. C., & Wylie-de Boer, E. C. 2009, MNRAS, 400, 1039

Zhang, H. W., & Zhao, G. 2006, A&A, 449, 127

Appendix A

Solar abundance ratios

We list here the solar abundances in literatures, Anders & Grevesse (1989), Grevesse et al. (1996), and Asplund et al. (2005, 2009), together with that we used with SPTOOL in this study.

Table A.1. The solar abundance ratios.

N	El.	SPTOOL spshow	Anders89 Photosphere	Grevesse96 Photosphere	Asplund05 Photosphere	Asplund09 Photosphere
1	H	12.00	12.00	12.00	12.00	12.00
2	He	10.99	10.99	10.99	10.93	10.93
3	Li	1.16	1.16	1.16	1.05	1.05
4	Be	1.15	1.16	1.15	1.38	1.38
5	B	2.60	2.60	2.60	2.70	2.70
6	C	8.56	8.56	8.55	8.39	8.43
7	N	8.05	8.05	7.97	7.78	7.83
8	O	8.93	8.93	8.87	8.66	8.69
9	F	4.56	4.56	4.56	4.56	4.56
10	Ne	8.09	8.09	8.08	7.84	7.93
11	Na	6.33	6.33	6.33	6.17	6.24
12	Mg	7.58	7.58	7.58	7.53	7.60
13	Al	6.47	6.47	6.47	6.37	6.45
14	Si	7.55	7.55	7.55	7.51	7.51
15	P	5.45	5.45	5.45	5.36	5.41
16	S	7.21	7.21	7.33	7.14	7.12
17	Cl	5.50	5.50	5.50	5.50	5.50
18	Ar	6.56	6.56	6.52	6.18	6.40
19	K	5.12	5.12	5.12	5.08	5.03
20	Ca	6.36	6.36	6.36	6.31	6.34
21	Sc	3.10	3.10	3.17	3.05	3.15
22	Ti	4.99	4.99	5.02	4.90	4.95
23	V	4.00	4.00	4.00	4.00	3.93
24	Cr	5.67	5.67	5.67	5.64	5.64
25	Mn	5.39	5.39	5.39	5.39	5.43
26	Fe	7.50	7.67	7.50	7.45	7.50
27	Co	4.92	4.92	4.92	4.92	4.99
28	Ni	6.25	6.25	6.25	6.23	6.22
29	Cu	4.21	4.21	4.21	4.21	4.19
30	Zn	4.60	4.60	4.60	4.60	4.56
31	Ga	2.88	2.88	2.88	2.88	3.04
32	Ge	3.41	3.41	3.41	3.58	3.65
33	As	2.37	...	...	...	...
34	Se	3.35	...	...	...	...

(continues)

Table A.1 (continued)

N	El.	SPTOOL spshow	Anders89 Photosphere	Grevesse96 Photosphere	Asplund05 Photosphere	Asplund09 Photosphere
35	Br	2.63	···	···	···	···
36	Kr	3.23	···	···	3.28	3.25
37	Rb	2.60	2.60	2.60	2.60	2.52
38	Sr	2.90	2.90	2.97	2.92	2.87
39	Y	2.24	2.24	2.24	2.21	2.21
40	Zr	2.60	2.60	2.60	2.59	2.58
41	Nb	1.42	1.42	1.42	1.42	1.46
42	Mo	1.92	1.92	1.92	1.92	1.88
43	Tc	−7.96	···	···	···	···
44	Ru	1.84	1.84	1.84	1.84	1.75
45	Rh	1.12	1.12	1.12	1.12	0.91
46	Pd	1.69	1.69	1.69	1.69	1.57
47	Ag	0.94	0.94	0.94	0.94	0.94
48	Cd	1.86	1.86	1.77	1.77	···
49	In	1.66	1.66	1.66	1.60	0.80
50	Sn	2.00	2.00	2.00	2.00	2.04
51	Sb	1.00	1.00	1.00	1.00	···
52	Te	2.24	···	···	···	···
53	I	1.51	···	···	···	···
54	Xe	2.23	···	···	2.27	2.24
55	Cs	1.12	···	···	···	···
56	Ba	2.13	2.13	2.13	2.17	2.18
57	La	1.22	1.22	1.17	1.13	1.10
58	Ce	1.55	1.55	1.58	1.58	1.58
59	Pr	0.71	0.71	0.71	0.71	0.72
60	Nd	1.50	1.50	1.50	1.45	1.42
61	Pm	−7.96	···	···	···	···
62	Sm	1.00	1.00	1.01	1.01	0.96
63	Eu	0.51	0.51	0.51	0.52	0.52
64	Gd	1.12	1.12	1.12	1.12	1.07
65	Tb	−0.10	−0.10	−0.10	0.28	0.30
66	Dy	1.10	1.10	1.14	1.14	1.10
67	Ho	0.26	0.26	0.26	0.51	0.48
68	Er	0.93	0.93	0.93	0.93	0.92

(continues)

Table A.1 (continued)

N	El.	SPTOOL spshow	Anders89 Photosphere	Grevesse96 Photosphere	Asplund05 Photosphere	Asplund09 Photosphere
69	Tm	0.00	0.00	0.00	0.00	0.10
70	Yb	1.08	1.08	1.08	1.08	0.84
71	Lu	0.76	0.76	0.76	0.06	0.10
72	Hf	0.88	0.88	0.88	0.88	0.85
73	Ta	0.13	···	···	···	···
74	W	1.11	1.11	1.11	1.11	0.85
75	Re	0.27	···	···	···	···
76	Os	1.45	1.45	1.45	1.45	1.40
77	Ir	1.35	1.35	1.35	1.38	1.38
78	Pt	1.80	1.80	1.80	···	···
79	Au	1.01	1.01	1.01	1.01	0.92
80	Hg	1.09	···	···	···	···
81	Tl	0.90	0.90	0.90	0.90	0.90
82	Pb	1.85	1.85	1.95	2.00	1.75
83	Bi	0.71	···	···	···	···
84	Po	−7.96	···	···	···	···
85	At	−7.96	···	···	···	···
86	Rn	−7.96	···	···	···	···
87	Fr	−7.96	···	···	···	···
88	Ra	−7.96	···	···	···	···
89	Ac	−7.96	···	···	···	···
90	Th	0.12	0.12	···	···	0.02
91	Pa	−7.96	···	···	···	···
92	U	−0.47	< -0.47	< -0.47	< -0.47	···
93	Np	−7.96	···	···	···	···
94	Pu	−7.96	···	···	···	···
95	Am	−7.96	···	···	···	···
96	Cm	−7.96	···	···	···	···
97	Bk	−7.96	···	···	···	···
98	Cf	−7.96	···	···	···	···
99	Es	−7.96	···	···	···	···

Appendix B

Histograms of [Fe/H] and literature values

We here plot the diagrams like Figures 3.5 and 3.6 for all the 10 calibrating stars (Chapter 3) and two standard Cepheids (Chapter 6). And we list atmospheric parameters and iron abundances of calibration stars in the literature (Chapter 3).

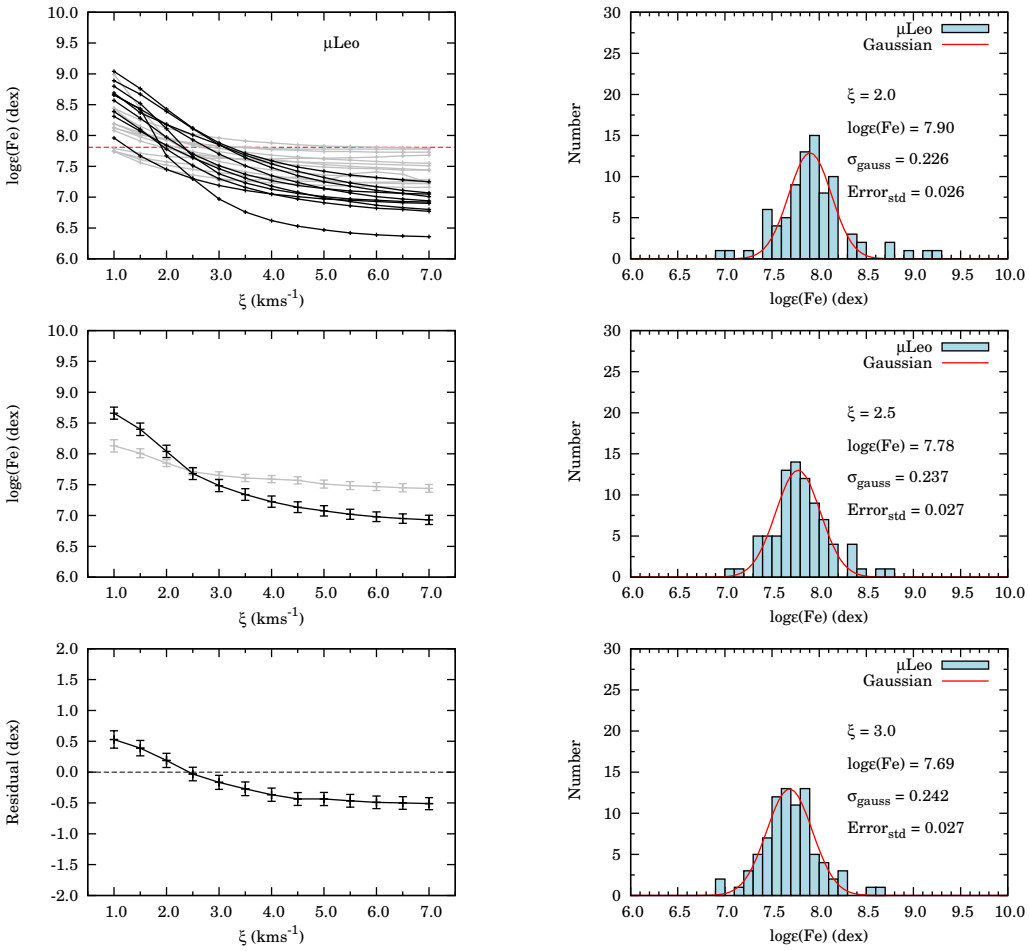

Figure B.1 The ξ–$\log \epsilon$(Fe) plot (left) and histograms of $\log \epsilon$(Fe) (right) values from individual lines for μ Leo. See the captions of Figures 3.5 and 3.6 for more details.

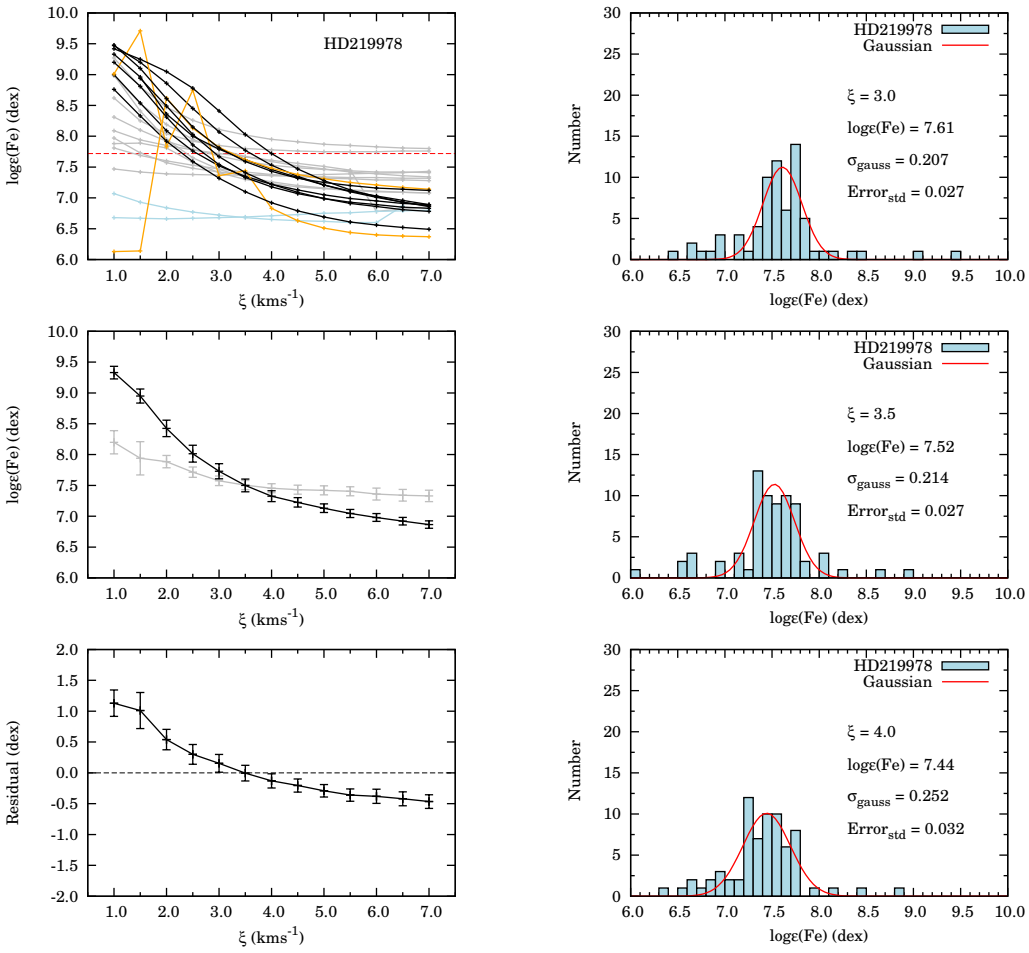

Figure B.2 Same as Figure B.1, but for HD 219978.

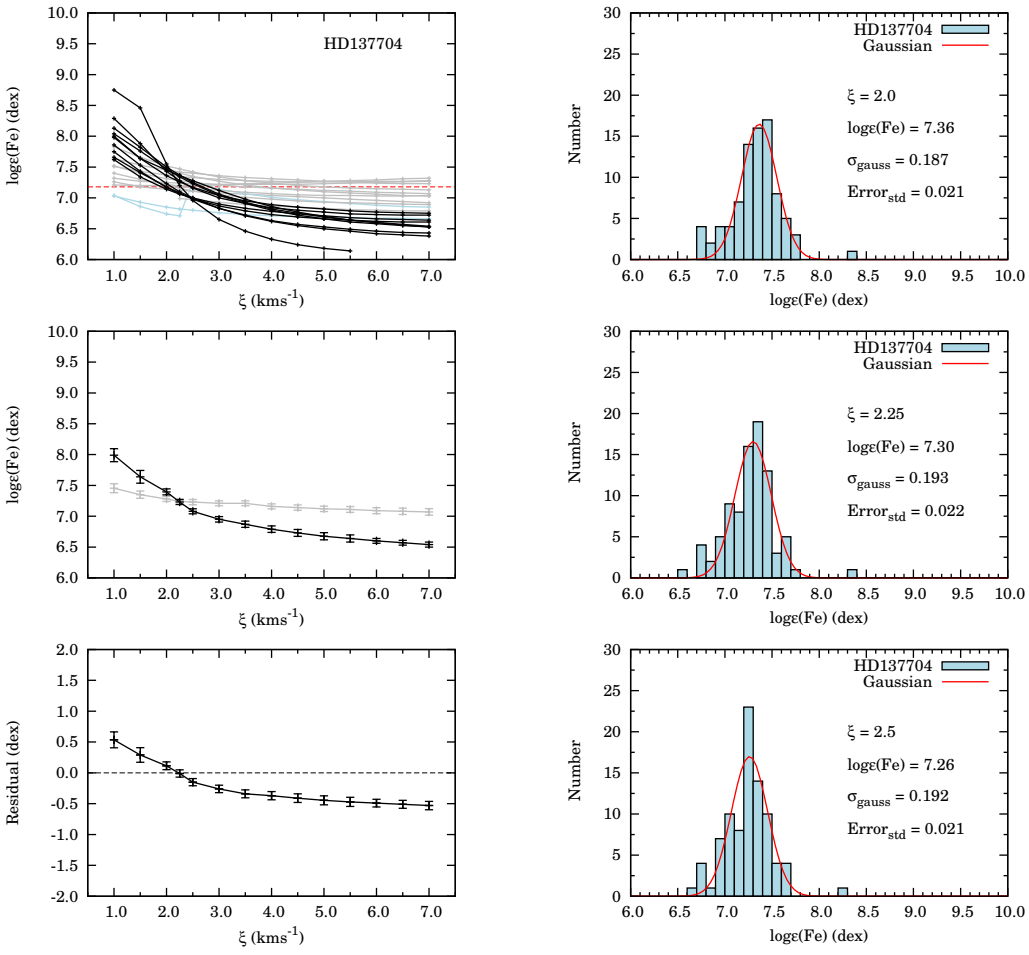

Figure B.3 Same as Figure B.1, but for HD 137704.

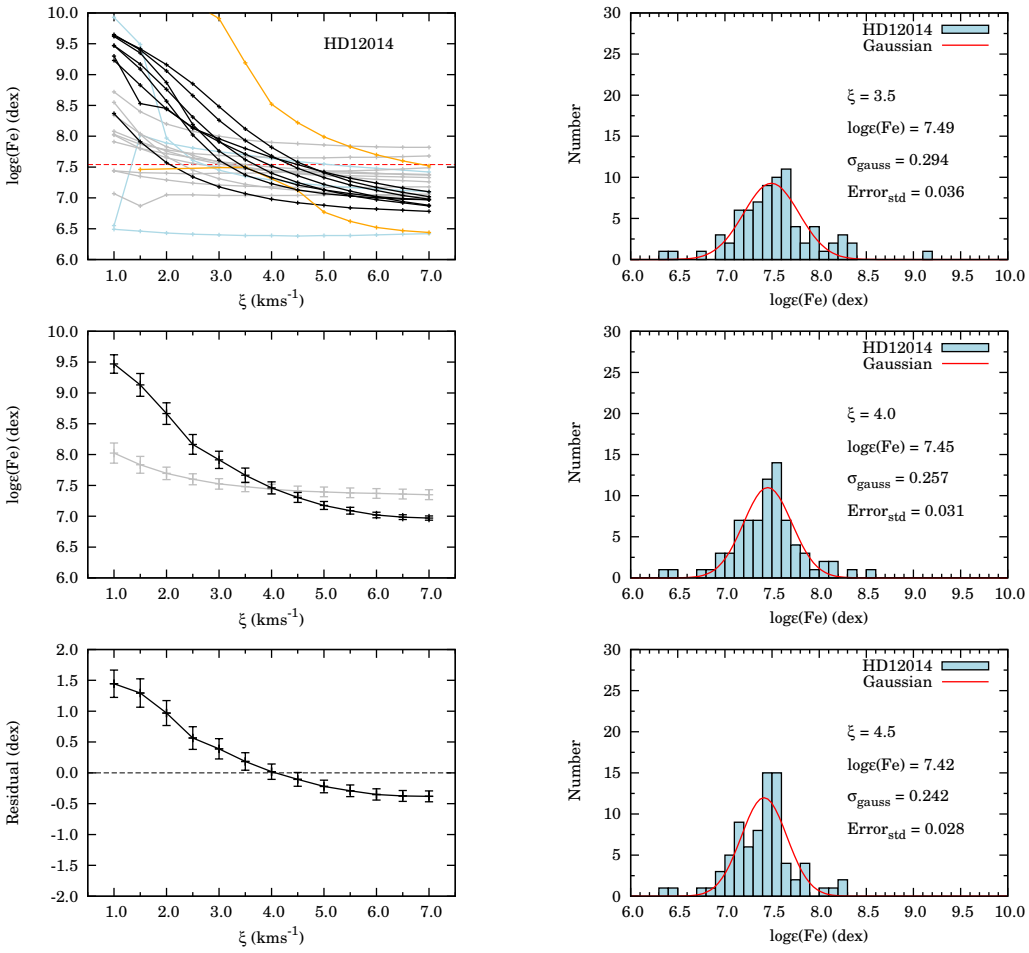

Figure B.4 Same as Figure B.1, but for HD 12014.

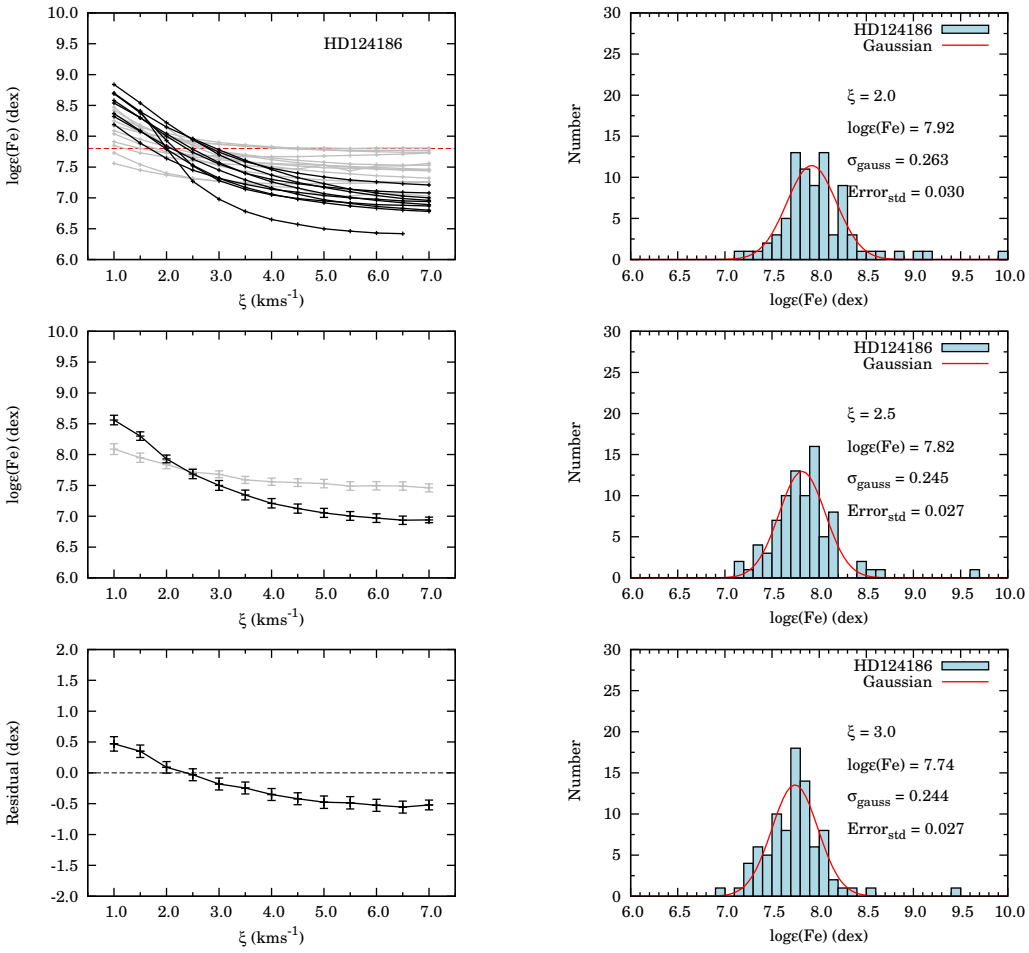

Figure B.5 Same as Figure B.1, but for HD 124186.

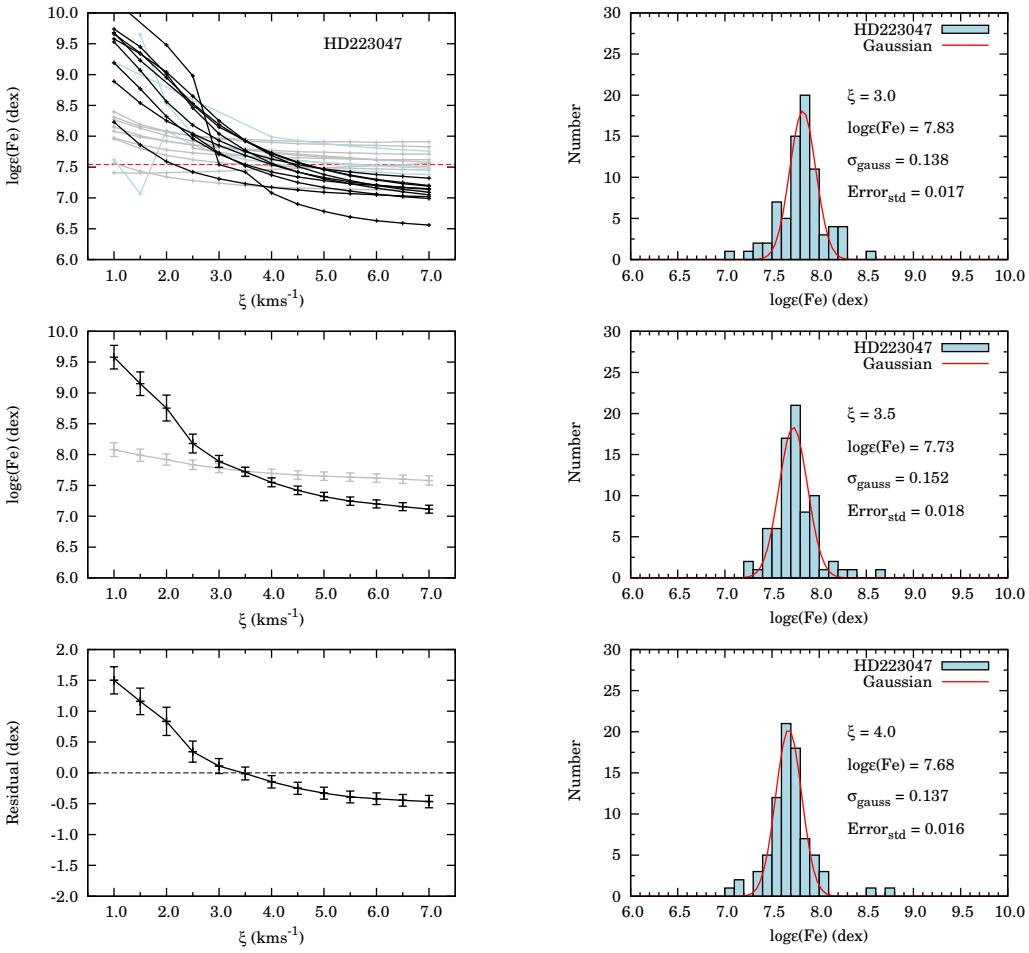

Figure B.6 Same as Figure B.1, but for HD 223047.

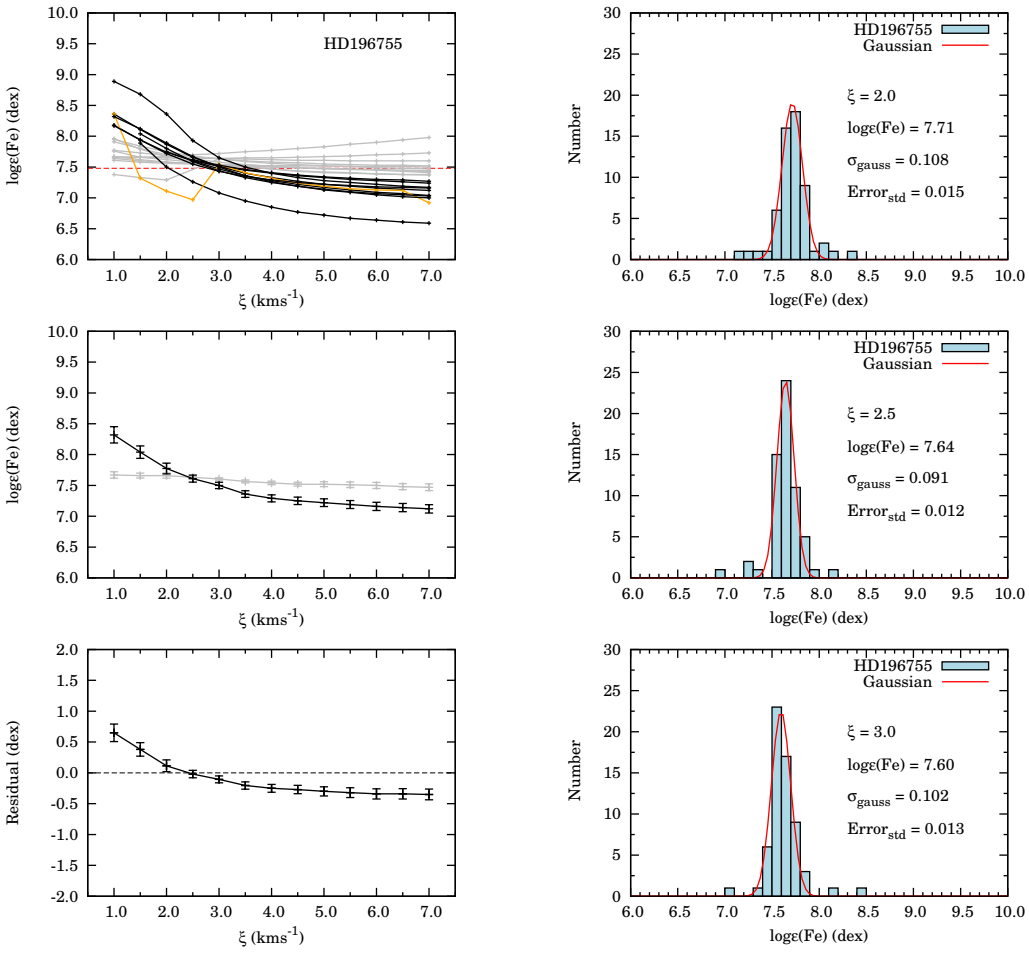

Figure B.7 Same as Figure B.1, but for HD 196755.

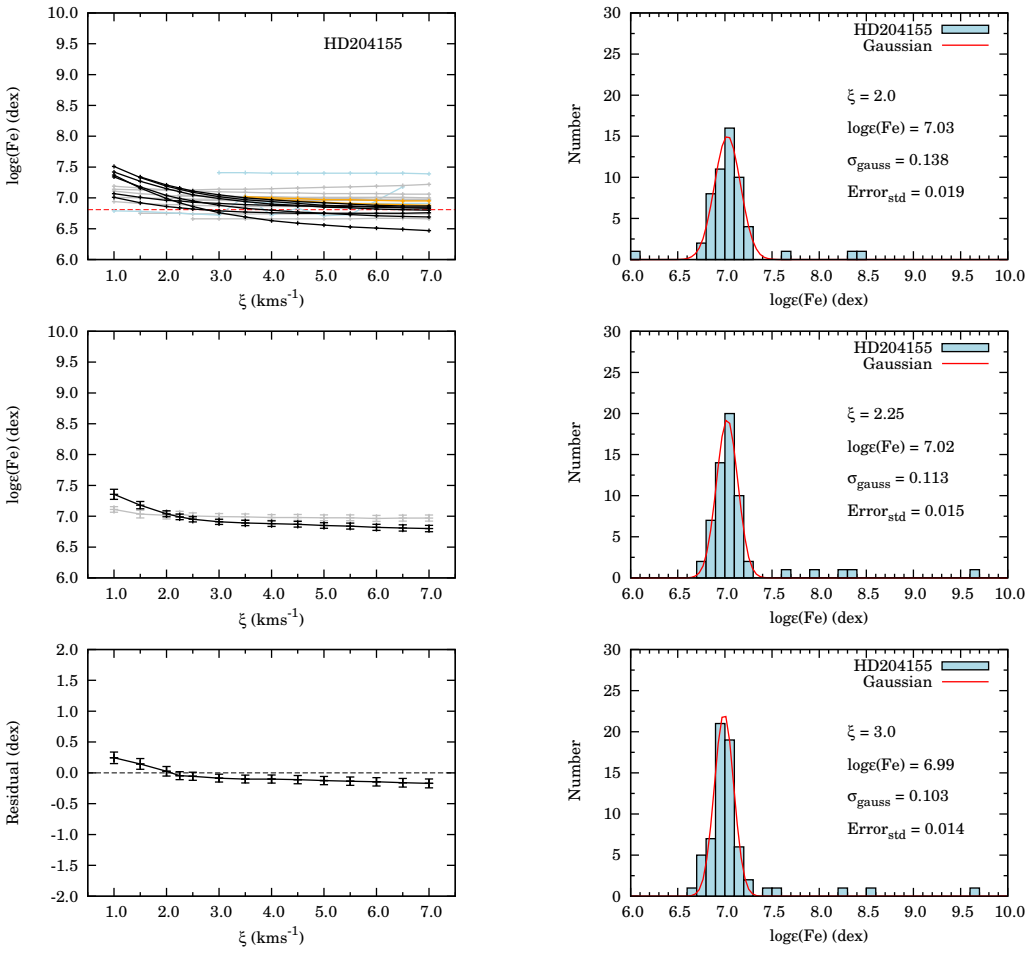

Figure B.8 Same as Figure B.1, but for HD 204155.

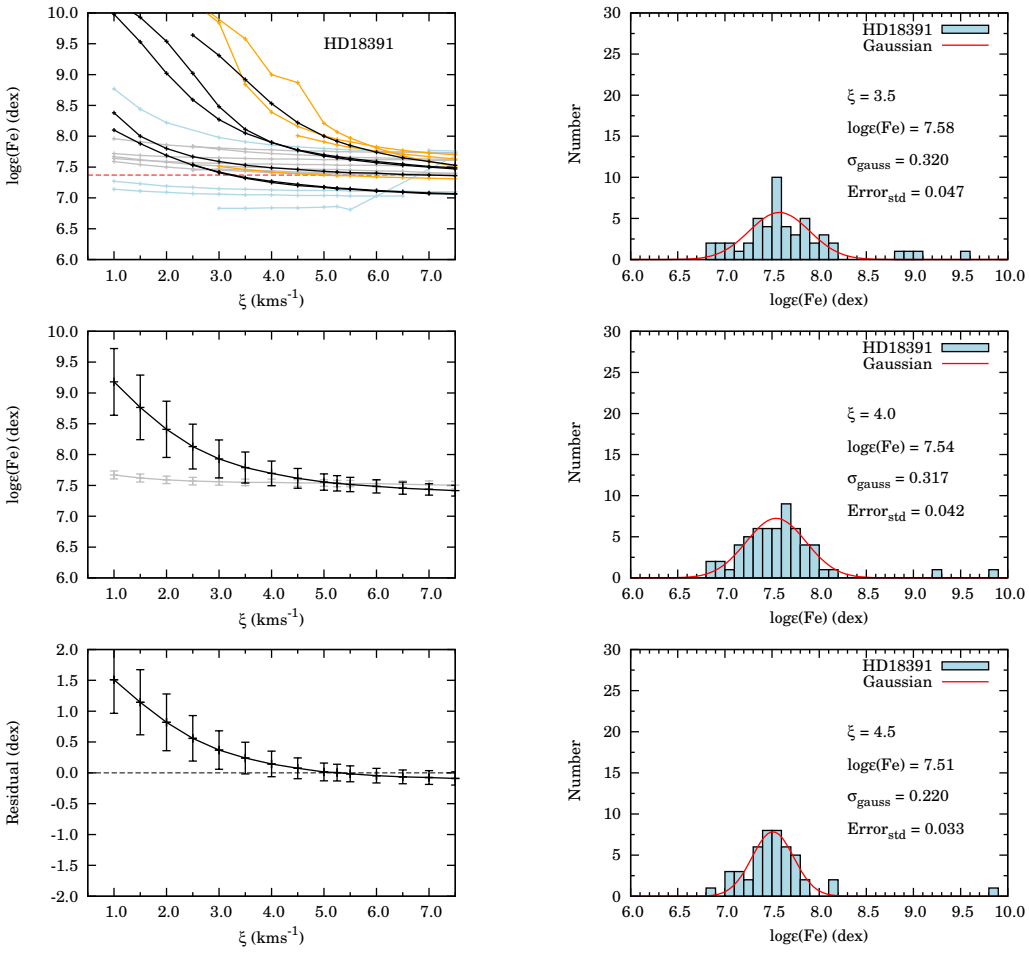

Figure B.9 Same as Figure B.1, but for HD 18391.

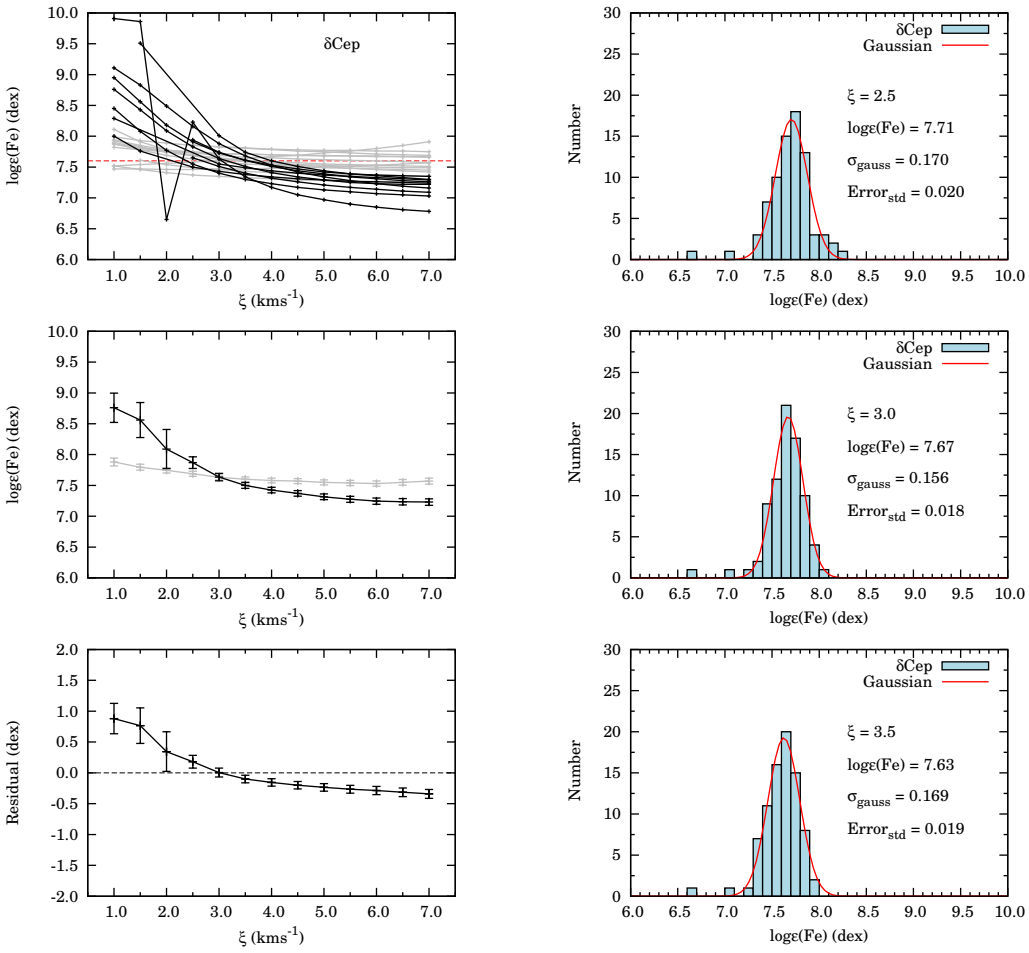

Figure B.10 Same as Figure B.1, but for δ Cep.

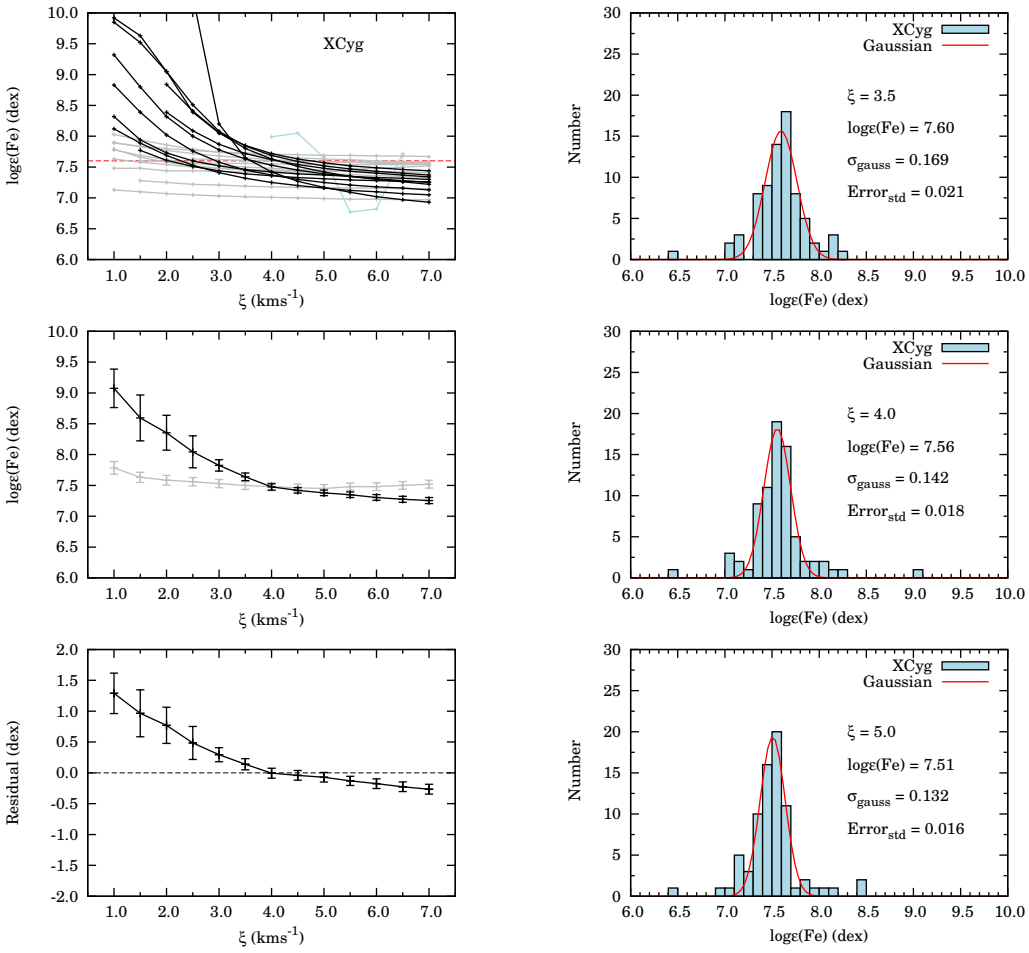

Figure B.11 Same as Figure B.1, but for X Cyg.

Table B.1. Iron abundances of calibration stars in the literature.

Object	$T_{\rm eff}$ (K)	$\log g$ (dex)	[Fe/H] (dex)	ξ (km/s)	Reference
HD 219978	3951	0.57	0.22	···	Prugniel et al.(2011)
	4242	0.80	−0.15	···	Cenarro et al.(2007)
	4242	0.80	−0.15	···	Sánchez−Blázquez et al.(2006)
	4250	0.80	−0.15	···	Cenarro et al.(2001)
HD 137704	4084	1.97	−0.32	···	Prugniel et al.(2011)
	4109	1.97	−0.37	···	Cenarro et al.(2007)
	4109	1.97	−0.37	···	Sánchez−Blázquez et al.(2006)
	4040	1.93	−0.43	···	McWilliam(1990)
Arcturus	4200	2.00	−0.32	1.60	Oinas(1977)
	4230	1.65	−0.63	1.95	Hekker & Meléndez(2007)
	4235	1.70	−0.49	2.40	Branch et al.(1978)
	4235	1.70	−0.60	2.40	Leep et al.(1987)
	4250	1.30	−0.68	1.70	Gonzalez & Wallerstein(1998)
	4271	0.90	−0.70	1.80	Maeckle et al.(1975)
	4271	1.73	−0.43	···	Cayrel de Strobel et al.(1970)
	4280	1.30	−0.54	1.40	McWilliam & Rich(1994)
	4280	1.69	−0.52	···	Meléndez et al.(2008)
	4280	2.19	−0.60	2.30	McWilliam(1990)
	4286	1.66	−0.52	1.74	Ramírez & Allende Prieto(2011)
	4300	1.50	−0.46	1.50	Britavskiy et al.(2012)
	4300	1.50	−0.47	1.40	Sneden et al.(1994)
	4300	1.50	−0.49	1.72	Carr et al.(2000)
	4300	1.50	−0.51	1.70	Hill(1997)
	4300	2.00	−0.69	1.50	Fernandez−Villacanas et al.(1990)
	4300	1.43	−0.52	···	Bruntt et al.(2011)
	4300	1.50	−0.63	1.70	Tomkin & Lambert(1999)
	4330	2.10	−0.58	1.60	Brown & Wallerstein(1992)
	4337	2.00	−0.56	···	Ramírez et al.(2007)
	4340	1.93	−0.55	1.87	Luck & Heiter(2006)
	4340	1.93	−0.55	1.87	Luck & Heiter(2005)
	4345	1.50	−0.38	1.50	Gratton & Ortolani(1986)
	4345	1.60	−0.81	1.70	Bell et al.(1985)
	4345	2.05	−0.37	1.50	Thévenin & Idiart(1999)
	4350	1.60	−0.58	1.60	Mishenina et al.(2003)

(continues)

Table B.1 (continued)

Object	$T_{\rm eff}$ (K)	$\log g$ (dex)	[Fe/H] (dex)	ξ (km/s)	Reference
	4350	1.60	−0.58	1.60	Mishenina & Kovtyukh(2001)
	4383	1.48	−0.53	2.20	Blackwell(1977)
	4383	1.70	−0.55	2.30	Kyrolainen et al.(1986)
	4383	1.97	−0.42	1.80	Edvardsson(1988)
	4421	0.980(1.06)	−0.48	2.80	Gratton et al.(1982)
	4500	2.01	−0.56	1.80	Lambert & Ries(1981)
	4275	1.70	−0.47	1.85	Smith et al.(2013)
	4300	1.50	−0.50	1.70	Peterson et al.(1993)
	4283	1.55	−0.50	1.61	Fulbright et al.(2006)
	4300	1.50	−0.50	1.50	Bergemann et al.(2012)
	4270	1.70	−0.60	1.50	Worley et al.(2009)
	4281	1.72	−0.55	1.49	Takeda et al.(2009)
	4250	1.30	−0.68	1.70	Gonzalez & Wallerstein (1998)
	4250	1.40	−0.57	1.73	Sheffield et al.(2012)
HD 12014	4371	0.66	0.04	···	Prugniel et al.(2011)
	5196	2.30	0.45	···	Sánchez−Blázquez et al.(2006)
	5173	2.35	0.45	···	Cenarro et al.(2001)
HD 124186	4419	2.66	0.30	···	Prugniel et al.(2011)
	4458	2.79	0.31	···	Koleva & Vazdekis(2012)
	4347	2.10	0.24	···	Sánchez−Blázquez et al.(2006)
	4346	2.10	0.24	···	Cenarro et al.(2001)
μ Leo	4308	2.20	0.31	···	Cayrel et al.(1991)
	4375	1.95	0.12	2.60	Luck & Challener(1995)
	4421	2.30	0.03	1.50	Peterson(1976)
	4421	2.30	−0.11	2.00	Peterson(1976)
	4460	2.40	−0.01	1.80	Oinas(1974)
	4480	2.61	0.17	2.20	McWilliam(1990)
	4525	2.70	0.44	···	Thygesen et al.(2012)
	4540	2.30	0.42	1.80	McWilliam & Rich(1994)
	4540	2.30	0.47	2.20	Castro et al.(1996)
	4540	2.30	0.46	1.60	Castro et al.(1996)
	4540	2.30	0.49	2.20	Castro et al.(1996)
	4540	2.30	0.48	1.60	Castro et al.(1996)
	4540	2.30	0.40	1.00	Castro et al.(1996)

(continues)

Table B.1 (continued)

Object	$T_{\rm eff}$ (K)	$\log g$ (dex)	[Fe/H] (dex)	ξ (km/s)	Reference
	4540	2.20	0.29	1.20	Smith & Ruck(2000)
	4541	2.30	0.35	1.20	Gratton & Sneden(1990)
	4541	2.35	0.48	1.30	Branch et al.(1978)
	4565	2.90	0.29	1.95	Hekker & Meléndez(2007)
	4660	2.63	0.53	···	Bruntt et al.(2011)
	4710	2.82	0.11	2.50	Lambert & Ries(1981)
	4550	2.10	0.30	1.80	Smith et al.(2013)
	4531	2.34	0.32	1.50	Fulbright et al. 2006
	4466	2.65	0.31	···	Prugniel et al.(2011)
HD 223047	5002	1.26	0.04	···	Prugniel et al.(2011)
	4990	1.50	0.10	···	Luck(1982)
	4990	1.50	0.10	···	Soubiran et al.(2008)
	4990	1.50	0.25	···	Luck(1977)
HD 196755	5582	3.64	−0.02	···	Prugniel et al.(2011)
	5750	3.83	0.09	···	Takeda(2007)
	5510	3.60	−0.09	···	Frasca et al.(2009)
	5611	3.65	−0.02	···	Cenarro et al.(2007)
	5660	3.77	0.02	···	Soubiran et al.(2008)
	5520	3.42	−0.07	···	McWilliam(1990)
	5680	3.70	0.01	···	Mishenina et al.(2003)
	5700	4.00	0.02	···	Feltzing & Gonzalez(2001)
	5750	3.83	0.09	···	Takeda et al.(2005)
	5510	3.60	−0.09	···	Randich et al.(1999)
	5520	3.42	−0.07	···	McWilliam(1990)
	5663	4.40	−0.05	···	Kuroczkin & Wiszniewski(1977)
HD 204155	5718	3.93	−0.69	···	Prugniel et al.(2011)
	5753	4.02	−0.69	···	Lee et al.(2011)
	5753	4.04	−0.65	···	Lee et al.(2011)
	5704	3.89	−0.70	···	Koleva & Vazdekis(2012)
	5702	4.51	−0.70	···	Sozzetti et al.(2009)
	5830	4.12	−0.63	···	Mashonkina & Gehren(2000)
	5700	4.00	−0.75	···	Fulbright(2000)
	5816	4.08	−0.56	···	Clementini et al.(1999)
	5829	4.12	−0.63	···	Fuhrmann(1998)

(continues)

Table B.1 (continued)

Object	$T_{\rm eff}$ (K)	$\log g$ (dex)	[Fe/H] (dex)	ξ (km/s)	Reference
	5650	3.99	−1.01	···	Axer et al.(1994)
	5608	4.24	−0.90	···	Cenarro et al.(2007)
	5600	3.80	−0.78	···	Mishenina et al.(2003)
	5600	3.80	−0.78	···	Mishenina & Kovtyukh(2001)
	5759	4.04	−0.56	···	Qui et al.(2002)
	5772	4.03	−0.73	···	Gratton et al.(2003)
	5773	3.99	−0.67	···	Zhang & Zhao(2006)
	5815	4.09	−0.66	···	Gehren et al.(2004)
HD 18391	5750	1.20	−0.13	···	Prugniel et al.(2011)
	5500	0.00	−0.28	···	Cenarro et al.(2007)

Appendix C

Line depths and the ratios of all observed stars

We here list line depths and the ratios of all the 10 calibrating stars used for temperature scales (Chapter 4). And we also list line depths and the ratios of two standard Cepheids and four target Cepheids (Chapter 6).

Table C.1. Measured line-depths (d) and ratios (r) with errors (σ) for the static calibration stars.

Object	d_1	e_1	d_2	e_2	r	e_r	T_i	σ_r	$\sigma_{\rm fit}$	$\sigma_{\rm all}$
(1) KI(15163.09)/FeI(15244.97)										
HD 219978	0.344	0.005	0.297	0.005	1.157	0.028	4186	70	238	248
HD 137704	0.216	0.006	0.201	0.006	1.073	0.044	4398	112	238	263
Arcturus	0.151	0.004	0.187	0.004	0.805	0.031	5074	77	238	250
HD 12014	0.352	0.006	0.320	0.006	1.098	0.026	4336	65	238	247
HD 124186	0.324	0.007	0.282	0.007	1.148	0.037	4211	93	238	256
μLeo	0.299	0.004	0.279	0.004	1.071	0.019	4404	48	238	243
HD 223047	0.240	0.006	0.251	0.006	0.956	0.033	4695	82	238	252
HD 196755	0.087	0.006	0.162	0.006	0.535	0.039	5757	99	238	258
HD 204155	0.038	0.007	0.085	0.007	0.449	0.091	5974	230	238	331
HD 18391	0.058	0.005	0.100	0.005	0.582	0.062	5639	156	238	285
(2) KI(15168.40)/SiI(15376.89)										
HD 219978	0.296	0.005	0.257	0.005	1.150	0.032	4273	55	246	252
HD 137704	0.200	0.006	0.182	0.006	1.103	0.050	4355	86	246	261
Arcturus	0.144	0.004	0.183	0.004	0.791	0.031	4893	54	246	252
HD 12014	0.314	0.006	0.303	0.006	1.035	0.027	4472	46	246	250
HD 124186	0.300	0.007	0.237	0.007	1.266	0.046	4074	80	246	259
μLeo	0.288	0.004	0.252	0.004	1.142	0.022	4287	37	246	249
HD 223047	0.211	0.006	0.258	0.006	0.820	0.030	4843	51	246	251
HD 196755	0.070	0.006	0.177	0.006	0.392	0.034	5582	59	246	253
HD 204155	0.030	0.007	0.129	0.007	0.228	0.056	5865	96	246	264
HD 18391	0.050	0.005	0.166	0.005	0.302	0.034	5738	58	246	253
(3) FeI(15194.50)/FeI(15207.54)										
HD 219978	0.300	0.005	0.365	0.005	0.822	0.019	3902	43	163	169
HD 137704	0.175	0.006	0.261	0.006	0.670	0.028	4249	64	163	175
Arcturus	0.128	0.004	0.241	0.004	0.533	0.021	4560	48	163	170
HD 12014	0.253	0.006	0.378	0.006	0.669	0.018	4251	41	163	168
HD 124186	0.185	0.007	0.337	0.007	0.548	0.023	4526	53	163	171
μLeo	0.171	0.004	0.328	0.004	0.522	0.012	4586	28	163	165

(continues)

Table C.1 (continued)

Object	d_1	e_1	d_2	e_2	r	e_r	T_i	σ_r	$\sigma_{\rm fit}$	$\sigma_{\rm all}$
HD 223047	0.143	0.006	0.319	0.006	0.448	0.020	4754	46	163	169
HD 196755	0.015	0.006	0.212	0.006	0.072	0.027	5611	60	163	174
HD 204155	···	0.007	0.132	0.007	···	···	···	···	163	···
HD 18391	···	0.005	0.181	0.005	···	···	···	···	163	···
(4) TiI(15543.78)/FeI(15591.49)										
HD 219978	0.491	0.005	0.319	0.007	1.539	0.037	3882	44	121	129
HD 137704	0.303	0.006	0.240	0.007	1.263	0.045	4210	53	121	132
Arcturus	0.232	0.004	0.188	0.006	1.233	0.046	4245	55	121	133
HD 12014	0.375	0.006	0.300	0.007	1.250	0.033	4225	39	121	127
HD 124186	0.295	0.007	0.302	0.008	0.978	0.034	4547	40	121	128
μLeo	0.282	0.004	0.287	0.004	0.985	0.019	4539	22	121	123
HD 223047	0.181	0.006	0.267	0.007	0.677	0.028	4904	34	121	126
HD 196755	0.025	0.006	0.213	0.008	0.117	0.027	5567	32	121	125
HD 204155	···	0.007	0.114	0.010	···	···	···	···	121	···
HD 18391	···	0.005	0.189	0.007	···	···	···	···	121	···
(5) TiI(15602.84)/FeI(16040.65)										
HD 219978	0.275	0.007	0.272	0.003	1.009	0.028	4006	28	67	73
HD 137704	0.175	0.007	0.177	0.005	0.986	0.049	4029	49	67	83
Arcturus	0.090	0.006	0.180	0.004	0.500	0.035	4523	36	67	76
HD 12014	bl	0.007	0.264	0.004	···	···	···	···	67	···
HD 124186	0.139	0.008	0.245	0.005	0.565	0.035	4457	35	67	76
μLeo	0.129	0.004	0.218	0.004	0.593	0.021	4429	21	67	70
HD 223047	bl	0.007	0.226	0.004	···	···	···	···	67	···
HD 196755	···	0.008	0.167	0.003	···	···	···	···	67	···
HD 204155	···	0.010	0.080	0.003	···	···	···	···	67	···
HD 18391	···	0.007	0.075	0.003	···	···	···	···	67	···
(6) TiI(15715.57)/FeI(15621.65)										
HD 219978	0.501	0.007	0.396	0.007	1.264	0.028	3954	42	41	59
HD 137704	0.337	0.007	0.292	0.007	1.155	0.037	4117	55	41	69

(continues)

Table C.1 (continued)

Object	d_1	e_1	d_2	e_2	r	e_r	T_i	σ_r	$\sigma_{\rm fit}$	$\sigma_{\rm all}$
Arcturus	0.263	0.006	0.249	0.006	1.055	0.036	4268	53	41	67
HD 12014	0.377	0.007	0.390	0.007	0.967	0.024	4400	35	41	54
HD 124186	0.352	0.008	0.365	0.008	0.964	0.030	4404	45	41	61
μLeo	0.324	0.004	0.346	0.004	0.937	0.016	4444	24	41	48
HD 223047	0.199	0.007	0.327	0.007	0.609	0.025	4937	38	41	56
HD 196755	0.037	0.008	0.238	0.008	0.154	0.033	5620	49	41	64
HD 204155	···	0.010	0.151	0.010	···	···	···	···	41	···
HD 18391	···	0.007	0.142	0.007	···	···	···	···	41	···
(7) FeI(16225.64)/FeI(16753.09)										
HD 219978	0.333	0.003	0.239	0.005	1.391	0.033	4331	67	414	419
HD 137704	0.228	0.005	0.145	0.006	1.575	0.077	3953	159	414	443
Arcturus	0.166	0.004	0.137	0.005	1.213	0.052	4697	108	414	428
HD 12014	0.283	0.004	0.184	0.006	1.536	0.054	4033	112	414	429
HD 124186	0.261	0.005	0.225	0.007	1.162	0.042	4802	87	414	423
μLeo	0.246	0.004	0.216	0.003	1.136	0.024	4856	50	414	417
HD 223047	0.187	0.004	0.179	0.006	1.045	0.043	5044	87	414	423
HD 196755	0.099	0.003	0.123	0.006	0.808	0.047	5530	96	414	425
HD 204155	0.038	0.003	0.040	0.007	0.948	0.192	5242	394	414	572
HD 18391	0.070	0.003	0.068	0.005	1.027	0.090	5079	184	414	453
(8) CoI(16757.64)/FeI(16316.35)										
HD 219978	0.245	0.005	0.381	0.003	0.644	0.014	3930	37	209	212
HD 137704	0.157	0.006	0.293	0.005	0.537	0.024	4204	61	209	218
Arcturus	0.102	0.005	0.266	0.004	0.383	0.020	4600	51	209	215
HD 12014	0.124	0.006	0.377	0.004	0.330	0.016	4737	42	209	213
HD 124186	0.192	0.007	0.368	0.005	0.522	0.020	4244	51	209	215
μLeo	0.181	0.003	0.369	0.004	0.491	0.010	4321	27	209	211
HD 223047	0.077	0.006	0.336	0.004	0.230	0.018	4993	47	209	214
HD 196755	0.013	0.006	0.234	0.003	0.055	0.025	5445	65	209	219
HD 204155	0.008	0.007	0.145	0.003	0.052	0.050	5451	128	209	245
HD 18391	···	0.003	0.228	0.003	···	···	···	···	209	···

(continues)

Table C.1 (continued)

Object	d_1	e_1	d_2	e_2	r	e_r	T_i	σ_r	$\sigma_{\rm fit}$	$\sigma_{\rm all}$
(9) AlI(16763.35)/FeI(16517.25)										
HD 219978	0.395	0.005	0.249	0.005	1.586	0.039	4112	72	197	210
HD 137704	0.318	0.006	0.192	0.006	1.653	0.063	3989	117	197	229
Arcturus	0.265	0.005	0.188	0.005	1.407	0.047	4442	86	197	215
HD 12014	0.313	0.006	0.238	0.006	1.316	0.041	4610	76	197	211
HD 124186	0.364	0.007	0.254	0.007	1.437	0.046	4388	85	197	215
μLeo	0.348	0.003	0.238	0.003	1.458	0.026	4348	47	197	203
HD 223047	0.253	0.006	0.232	0.006	1.093	0.039	5024	72	197	210
HD 196755	0.167	0.006	0.173	0.006	0.966	0.047	5257	88	197	216
HD 204155	0.112	0.007	0.082	0.007	1.366	0.148	4520	274	197	337
HD 18391	0.092	0.005	0.149	0.005	0.621	0.041	5894	75	197	211

Table C.2. Measured line-depths (d) and ratios (r) with errors (σ) for standard Cepheids.

N	d_1	e_1	d_2	e_2	r	e_r	T_i	σ_r	$\sigma_{\rm fit}$	$\sigma_{\rm all}$
δ Cep : $T_{\rm eff} = 5663 \pm 46$ (K)										
(1)	0.086	0.005	0.132	0.005	0.652	0.044	5461	112	238	263
(2)	0.068	0.005	0.189	0.005	0.357	0.028	5642	48	246	251
(3)	0.025	0.005	0.207	0.005	0.118	0.024	5505	54	163	172
(4)	0.021	0.005	0.219	0.006	0.094	0.023	5595	27	121	124
(5)	···	0.006	0.109	0.003	0.000	···	···	···	67	···
(6)	0.015	0.006	0.199	0.006	0.073	0.031	5742	46	41	62
(7)	0.098	0.003	0.105	0.005	0.940	0.052	5257	107	414	428
(8)	···	0.005	0.237	0.003	0.000	···	···	···	209	···
(9)	0.143	0.005	0.165	0.005	0.868	0.039	5439	71	197	210
X Cyg : $T_{\rm eff} = 5646 \pm 71$ (K)										
(1)	0.050	0.006	0.094	0.006	0.536	0.077	5755	193	238	307
(2)	0.043	0.006	0.144	0.006	0.296	0.046	5748	79	246	258
(3)	···	0.006	0.155	0.006	0.000	···	···	···	163	···
(4)	···	0.006	0.164	0.008	0.000	···	···	···	121	···
(5)	···	0.008	0.087	0.003	0.000	···	···	···	67	···
(6)	···	0.008	0.146	0.008	0.000	···	···	···	41	···
(7)	0.066	0.003	0.074	0.007	0.894	0.091	5353	188	414	455
(8)	0.008	0.007	0.195	0.003	0.040	0.034	5484	88	209	227
(9)	0.092	0.007	0.131	0.007	0.703	0.062	5743	115	197	228

Table C.3. Measured line-depths (d) and ratios (r) with errors (σ) for target Cepheids.

N	d_1	e_1	d_2	e_2	r	e_r	T_i	σ_r	$\sigma_{\rm fit}$	$\sigma_{\rm all}$
GCC-a : $T_{\rm eff} = 5293 \pm 292$ (K)										
(1)	0.077	0.034	0.115	0.034	0.668	0.358	5420	905	238	936
(2)	0.130	0.034	0.218	0.034	0.597	0.183	5229	316	246	401
(3)	0.119	0.034	0.238	0.034	0.498	0.161	4642	366	163	401
(4)	···	0.034	0.227	0.030	···	···	···	···	121	···
(5)	···	0.030	0.167	0.021	···	···	···	···	67	···
(6)	···	0.030	0.243	0.030	···	···	···	···	41	···
(7)	0.190	0.021	0.129	0.020	1.475	0.282	4159	579	414	712
(8)	···	0.020	0.246	0.021	···	···	···	···	209	···
(9)	0.120	0.020	0.192	0.020	0.628	0.123	5883	227	197	300
GCC-b : $T_{\rm eff} = 5243 \pm 245$ (K)										
(1)	0.151	0.025	0.103	0.025	1.464	0.430	3412	1086	238	1112
(2)	···	0.025	0.164	0.025	···	···	···	···	246	···
(3)	···	0.025	0.185	0.025	···	···	···	···	163	···
(4)	···	0.025	0.236	0.022	···	···	···	···	121	···
(5)	···	0.022	0.119	0.016	···	···	···	···	67	···
(6)	···	0.022	0.194	0.022	···	···	···	···	41	···
(7)	0.114	0.016	0.126	0.016	0.899	0.169	5342	346	414	540
(8)	0.065	0.016	0.243	0.016	0.265	0.066	4903	170	209	270
(9)	0.117	0.016	0.155	0.016	0.756	0.126	5645	232	197	304
GCC-c : $T_{\rm eff} = 4774 \pm 157$ (K)										
(1)	0.332	0.046	0.272	0.046	1.220	0.269	4028	678	238	719
(2)	0.264	0.046	0.352	0.046	0.749	0.164	4967	284	246	376
(3)	0.196	0.046	0.406	0.046	0.483	0.127	4676	288	163	331
(4)	0.337	0.046	0.239	0.038	1.411	0.296	4034	351	121	371
(5)	blend	0.038	0.276	0.025	···	···	···	···	67	···
(6)	0.305	0.038	0.360	0.038	0.849	0.138	4576	207	41	211
(7)	0.232	0.025	0.225	0.023	1.032	0.154	5070	316	414	521
(8)	0.116	0.023	0.354	0.025	0.329	0.069	4740	177	209	274

(continues)

Table C.3 (continued)

N	d_1	e_1	d_2	e_2	r	e_r	T_i	σ_r	$\sigma_{\rm fit}$	$\sigma_{\rm all}$
(9)	0.273	0.023	0.321	0.023	0.849	0.094	5474	173	197	262
GCC-d : $T_{\rm eff} = 4991 \pm 119$ (K)										
(1)	0.108	0.039	0.188	0.039	0.575	0.241	5656	608	238	1099
(2)	0.125	0.039	0.212	0.039	0.592	0.216	5237	372	246	246
(3)	0.103	0.039	0.252	0.039	0.407	0.168	4847	383	163	163
(4)	···	0.039	0.224	0.034	···	···	···	···	121	···
(5)	···	0.034	0.160	0.024	···	···	···	···	67	···
(6)	···	0.034	0.253	0.034	···	···	···	···	41	···
(7)	0.117	0.024	0.168	0.024	0.694	0.173	5764	355	414	534
(8)	0.053	0.024	0.300	0.024	0.175	0.081	5135	209	209	266
(9)	0.210	0.024	0.161	0.024	1.302	0.245	4638	452	197	298